Székeli Ádám, Bsc

Impact of Gas Diffusion Layer Characteristics on Water Management on SO2 -Depolarized Electrolysis

MASTER'S THESIS

to achieve the university degree of

Diplom-Ingenieur

Master's degree program:

Technical Chemistry

submitted to

Graz University of Technology

Supervisor

Ass.Prof. Dipl.-Ing. Dr.techn. BSc Merit Bodner

Institute of Chemical Engineering and Environmental Technology

Ing. Civ. Lukas Fernando Roessler Escudero

Graz, June 2026

Abstract

Sulfur depolarized electrolysis (SDE) is a promising alternative for hydrogen production, while simultaneously producing sulfuric acid. In SDE, the kinetically demanding oxygen evolution reaction is replaced by the oxidation of SO_2 to sulfuric acid. This reduces the reversible cell potential to 0.158 V vs RHE. Currently SDE remains at an early stage of development, and several aspects of cell operation are not yet fully understood. A definitive reaction mechanism for the anodic sulfur dioxide oxidation reaction has not been established, which complicates the determination of ideal operating conditions and how cell components should be optimized. One such component is the gas diffusion layer (GDL), which strongly affects mass transfer processes and governs the distribution of gaseous and liquid species between the flow field and the catalyst layer. Despite its importance for efficient and stable long-term operation, the GDL properties most suitable for SDE have not been established.

In this master's thesis, commercially available GDLs from SGL Carbon and Freudenberg are systematically evaluated to identify GDL properties beneficial for gas-fed SDE operation. Five GDL materials differing in substrate structure, thickness, hydrophobic treatment, and the presence or absence of a microporous layer were investigated in symmetric and asymmetric cell configurations, totaling 12 tested combinations. Performance was evaluated by in-situ testing, involving polarization curves and electrochemical impedance spectroscopy (EIS). Short-term stability was assessed during 4 h operation at selected operating points. Scanning electron microscopy (SEM), mercury intrusion porosimetry (MIP), contact angle measurements were carried out for ex-situ characterization of the GDLs.

The results show that the GDL selection has a strong impact on performance and operational stability. GDLs with high pore volume and sufficiently large pore diameters supported stable operation, while dense or poorly permeable materials led to severe transport limitations. The two electrodes were found to require different GDL properties: water-retaining materials were beneficial on the cathode side, whereas sufficient permeability and easier liquid removal were beneficial on the anode side. The best performing configuration; Freudenberg E35 on the cathode and Sigracet GDL10BA on the anode, reached a current density of 1.31 A/cm^2 at 1.2 V. Analysis of the product via titration confirmed current efficiencies close to 100%, indicating that parasitic reactions were negligible under the operating conditions.

Based on experimental observations, a working hypothesis was proposed. According to that for stable operation a flooded anode-side GDL is required. This allows SO_2 to dissolve into the retained liquid phase without displacing the produced acid. Overall, this work demonstrates the importance of optimized diffusion media SDE performance and outlines design guidelines for future GDL development customized for SDE applications.

Kurzfassung

Die schwefel-depolarisierte Elektrolyser (SDE) ist eine vielversprechende Alternative zur Wasserstoffproduktion, bei welcher als Zweitprodukt Schwefelsäure statt Sauerstoff erzeugt wird. . In der SDE wird die kinetisch anspruchsvolle Sauerstoffentwicklungsreaktion durch die Oxidation von SO_2 zu Schwefelsäure ersetzt. Dadurch wird das reversible Zellpotential auf 0,158 V vs. RHE reduziert. Die SDE befindet sich noch in einem frühen Entwicklungsstadium, und mehrere Aspekte des Zellbetriebs sind noch nicht vollständig verstanden. Ein definitiver Reaktionsmechanismus für die anodische Schwefeldioxid-Oxidationsreaktion wurde bisher nicht etabliert. Dies erschwert die Bestimmung idealer Betriebsbedingungen und die Optimierung der Zellkomponenten. Eine solche Komponente ist die Gasdiffusionsschicht (GDS), die Massentransferprozesse stark beeinflusst und die Verteilung gasförmiger und flüssiger Spezies zwischen dem Strömungsfeld und der Katalysatorschicht steuert. Trotz ihrer Bedeutung für einen effizienten und stabilen Langzeitbetrieb wurden die für die SDE am besten geeigneten GDL-Eigenschaften bisher nicht etabliert.

In dieser Masterarbeit werden kommerziell erhältliche GDLs von SGL Carbon und Freudenberg systematisch untersucht, um GDL-Eigenschaften zu identifizieren, die für den gasgespeisten SDE-Betrieb vorteilhaft sind. Fünf GDL-Materialien, die sich in Substratstruktur, Dicke, hydrophober Behandlung und dem Vorhandensein oder Fehlen einer mikroporösen Schicht unterscheiden, wurden in symmetrischen und asymmetrischen Zellkonfigurationen untersucht. Insgesamt wurden 12 Kombinationen getestet. Die Leistung wurde durch In-situ-Tests bewertet, einschließlich Polarisationskurven und elektrochemischer Impedanzspektroskopie (EIS). Die Kurzzeitstabilität wurde während eines 4-stündigen Betriebs an ausgewählten Betriebspunkten untersucht. Rasterelektronenmikroskopie (SEM), Quecksilberintrusionsporosimetrie (MIP) und Kontaktwinkelmessungen wurden zur Ex-situ-Charakterisierung der GDLs durchgeführt.

Die Ergebnisse zeigen, dass die Auswahl der GDL einen starken Einfluss auf die Leistung und die Betriebsstabilität hat. GDLs mit hohem Porenvolumen und ausreichend großen Porendurchmessern unterstützten einen stabilen Betrieb, während dichte oder schlecht permeable Materialien zu starken Transportlimitierungen führten. Es wurde festgestellt, dass die beiden Elektroden unterschiedliche GDL-Eigenschaften erfordern: wasserretentive Materialien waren auf der Kathodenseite vorteilhaft, während ausreichende Permeabilität und eine einfachere Flüssigkeitsentfernung auf der Anodenseite vorteilhaft waren. Die leistungsstärkste Konfiguration; Freudenberg E35 auf der Kathode und Sigracet GDL10BA auf der Anode, erreichte eine Stromdichte von 1,31 A/cm^2 bei 1,2 V. Die Analyse des Produkts mittels Titration bestätigte Stromausbeuten nahe 100 %, was darauf hinweist, dass parasitäre Reaktionen unter den Betriebsbedingungen vernachlässigbar waren.

Auf Grundlage der experimentellen Beobachtungen wurde eine Arbeitshypothese vorgeschlagen, nach der für einen stabilen Betrieb eine geflutete anodenseitige GDL erforderlich ist. Dies ermöglicht es SO_2, sich in der zurückgehaltenen flüssigen Phase zu lösen, ohne die produzierte Säure zu verdrängen.

Insgesamt zeigt diese Arbeit die Bedeutung optimierter Diffusionsmedien für die SDE-Leistung und skizziert Designrichtlinien für die zukünftige GDL-Entwicklung, die auf SDE-Anwendungen zugeschnitten ist.

Contents

Acknowledgements

Use of generative AI tools

During the preparation of this thesis, generative AI tools were used as supporting tools. ChatGPT, based on OpenAI's GPT-5.5 Thinking model, was used for sentence restructuring, and improving the readability of selected text passages. Google Gemini 3.1 Pro was used for the preparation of selected figures (Figure 1-6), including image upscaling and the generation schematic diagrams. These tools were not used as primary scientific sources. All AI-assisted text and figure content was critically reviewed, verified, and, where necessary, modified by the author. Calculations, figures, and references were checked and approved by the author. The author takes full responsibility for the submitted work.

1. Introduction

The current global energy system faces many challenges. It must be able to meet continuously growing global energy demand (~ 181,000 TWh in 2024 [1]) while also addressing increasing concerns over energy security and climate change. Fossil energy carriers remain problematic because they are finite, geographically unevenly distributed, and associated with greenhouse-gas emissions (global CO_2 from fossil-fuel energy use in 2024 was about 34.7 Gt CO_2 [1]) and environmental pollution, both of which contribute to global warming. These concerns have led to a gradual shift away from fossil-based systems of energy production and consumption toward renewable energy sources such as wind and solar. The share of renewables in electricity generation was about 32% in 2024, globally. [2] This energy transition is accelerating, as shown by the unprecedented expansion of renewable power: in 2024, global renewable electricity capacity additions reached nearly 685 GW, 22% higher than in 2023. [2] However, the growing share of renewable electricity also increases the need for efficient energy storage and conversion technologies. This has led to renewed interest in the concept of a hydrogen economy, which is a concept for a future energy system where hydrogen serves as a primary energy carrier to replace traditional hydrocarbons such as oil, coal, and natural gas across all sectors of the economy. Ideally renewable or low-carbon energy is used to produce hydrogen, that can be stored for long periods, transported by pipelines or ships, and used later as a fuel or chemical feedstock in sectors where direct electrification is difficult. This would allow the deeper penetration of renewables into hard-to-abate sectors such as steel production, ammonia synthesis, heavy transport, shipping, aviation, and long-term energy storage.

1.1. The hydrogen economy

The concept of a hydrogen economy was first popularized in the early 1970s. John O'M. Bockris and A. J. Appleby first published the term in their 1972 paper "The Hydrogen Economy: An Ultimate Economy?". [3] The idea quickly caught international attention and in 1973, the first dedicated conference on hydrogen energy was organized at Cornell University, followed by the more influential Miami Energy Conference in 1974, organized by T. Nejat Veziroglu. These events brought together leading researchers to discuss hydrogen's potential role in future energy systems. The same year, the International Association for Hydrogen Energy (IAHE) was established, with both Bockris and Veziroglu being among the founding members. In 1976 the first issue of the *International Journal of Hydrogen Energy (IJHE)*, was released, which remains a central platform for research in the field. [4] From this point onwards, hydrogen increasingly gained traction as a proposed clean energy carrier, moving beyond electrochemistry into wider discussions across science, industry, energy policy, and legislation.

Since then, hydrogen has experienced several waves of enthusiasm particularly during the 1970s oil crises, again in the 1990s with growing concern over climate change, and once more in the early 2000s with renewed interest in fuel cells and transport applications. [5] The IEA's latest report identifies this recurring pattern where periods of very high expectations and hundreds of project announcements are often followed by delays, cancellations, policy backsteps, company failures. [6] The renewed interest in hydrogen in the last decade is driven by falling renewable electricity costs, improved electrolyser technologies, the ever-growing urgency of climate targets. [5]

1.2. Potential for hydrogen

The appeal of hydrogen rests on its molecular and stable nature. Unlike electricity, which requires real-time balancing between production and consumption, hydrogen can be converted, stored, and transported and later reconverted into useful energy. Because hydrogen is the lightest element, held together by strong chemical bonds (bond dissociation enthalpy of ΔH_D(H−H) =436 kJ/mol [7]), it possesses the highest gravimetric energy density of all known substances.

The energy content of hydrogen is commonly expressed in terms of the lower heating value (LHV) and the higher heating value (HHV). [8]These values are derived from the enthalpy change of hydrogen combustion, depending on whether the produced water is assumed to remain in the vapor phase or to condense to liquid water, respectively.[9]

$$LHV = \frac{\Delta H^\circ_{(H_2O(g))}}{M_{(H_2)}} = \frac{241.8\,\frac{kJ}{mol}}{0.002016\,\frac{kg}{mol}} = 119.9\,\frac{MJ}{kg} \xrightarrow{:3.6\,\frac{MJ}{kWh}} 33.3\,\frac{kWh}{kg} \qquad \text{Eq. 1}$$

$$HHV = \frac{\Delta H^\circ_{(H_2O(l))}}{M_{(H_2)}} = \frac{285.8\,\frac{kJ}{mol}}{0.002016\,\frac{kg}{mol}} = 141.8\,\frac{MJ}{kg} \xrightarrow{:3.6\,\frac{MJ}{kWh}} 39.4\,\frac{kWh}{kg} \qquad \text{Eq. 2}$$

Considering its lower heating value (LHV) of 120.1 MJ/kg, corresponding to approximately 33.4 kWh/kg, hydrogen has nearly three times the gravimetric energy content of gasoline. [5] Furthermore, when it is burned or used in a fuel cell, it produces only water, which is beneficial for reducing local emissions.

For these reasons, hydrogen is widely considered a possible solution for long-term and seasonal energy storage. Surplus electricity from variable renewable sources, such as wind and solar power, can be converted into hydrogen or used later at the location and time of demand. This way, hydrogen can help reduce curtailment of renewable electricity

and support decarbonization by allowing a deeper integration of renewable energy into the energy system.

In the transport sector, fuel cell systems are especially relevant for heavy-duty, long-distance applications such as maritime, rail, and aviation, where battery mass, charging time, or operational range are limited. Beyond direct use in fuel cells. Hydrogen can also serve as a feedstock for synthetic fuels, including ammonia, methanol, and other e-fuels. Hydrogen also holds potential for buildings and district energy systems. It can be integrated into existing infrastructure by blending it into natural gas networks, used directly in dedicated hydrogen boilers, or deployed in fuel cells for combined heat and power.

Indeed, there are many possible new applications, and alternative production methods, but the current hydrogen landscape remains dominated by already established industrial processes. In 2024, global hydrogen demand increased to almost 100 Mt, of which less than 1% came from low-emissions sources. In addition, hydrogen is largely produced and consumed on-site within the same facility. Around 85% is used where it's made.[5] Most of this hydrogen remains confined to already established industrial uses such as oil refining (hydrotreatment / hydrocracking), ammonia synthesis, methanol synthesis and steel making (DRI). [6] New applications accounted for less than 1% of the global demand in 2024. Europe is performing slightly better than the global average, with new applications representing ~ 4% of its regional hydrogen demand. [10]

Because these industries already possess the necessary infrastructure and expertise, they present a strategic opportunity for "drop-in" solutions. Replacing fossil-derived hydrogen with low-carbon hydrogen offers a relatively direct decarbonization pathway.

Despite its strong potential the widespread adoption of hydrogen is yet to happen. Low-emissions hydrogen production is still more expensive than conventional fossil-based routes. Large-scale deployment is further limited by the lack of transport, distribution and refueling infrastructure. Hydrogen's low volumetric energy density makes compact storage and transport technically challenging. At standard temperature and pressure, hydrogen's volumetric energy density is ~ 0.01 MJ/L. [11] For comparison, methane at ambient pressure has a density of roughly 0.0378 MJ/L. When hydrogen is highly compressed to 700 bar (a common pressure for vehicle fuel tanks), its volumetric energy density increases to 5.6 MJ/L [11] which is approximately 15% of the energy density of gasoline which is around 34.6 MJ/L [11]

The further expansion of the hydrogen economy not only depends on technological progress, but also on coordinated political and industrial support. This has led to a growing number of national hydrogen strategies, international initiatives and policy frameworks aimed at accelerating hydrogen deployment and reducing economic and infrastructural barriers.

1.3. Hydrogen initiatives, and policy drivers in Europe

In 2019 the European Commission presented European Green Deal [12], providing an overarching framework for the EU's climate and energy policy. Its central objective is to make the EU climate-neutral by 2050. The Commission's EU Hydrogen Strategy[13], published in 2020, translated this general climate goal into a hydrogen-specific roadmap. It set targets of at least 6 GW of renewable hydrogen electrolysers, increasing to 40 by 2030. The European Clean Hydrogen Alliance [14] was launched alongside the strategy to support implementation by helping coordination between the different players of the value chain. To achieve the climate goals of the Green Deal, the EU introduced the Fit for 55 package. Its goal is to reduce greenhouse-gas emissions by at least 55% by 2030 compared with 1990 levels.

From a hydrogen policy perspective, one of the most important legal instruments is the Renewable Energy Directive (RED), more precisely its third revision, RED III, adopted in 2023. RED III sets a binding industrial hydrogen target: by 2030, at least 42% of hydrogen used in industry must come from renewable fuels of non-biological origin (RFNBOs), a category that includes renewable hydrogen.

The REPowerEU plan [15] strengthened this direction after Russia's invasion of Ukraine and the energy crisis. It links hydrogen policy not only to decarbonization, but also to energy security. The EU aims to produce 10 Mt of renewable hydrogen domestically and import another 10 Mt by 2030. This target shows that hydrogen is not only seen as a climate technology, but also as part of the EU's energy-independence strategy.

The EU has also created more specific rules and laws for hydrogen markets via the Hydrogen and Decarbonized Gas Market Package [16] adopted in 2024. It aims to support cross-border hydrogen transport, improve access to infrastructure, enable the repurpose of parts of the existing gas network, and create more predictable market conditions for investors. In addition, the EU uses delegated acts to define what counts as renewable hydrogen and how greenhouse-gas savings must be calculated. This is important because hydrogen only contributes to climate targets if it is produced with sufficiently low emissions. The delegated acts therefore create technical criteria for renewable hydrogen, especially regarding electricity sourcing.

Notably, the EU has created a strong political push for renewable hydrogen, but set targets proved to be too ambitious. REPowerEU aims for 10 Mt of domestic renewable hydrogen production [17] but current data suggest a large gap between the goal and what is achievable.[18] Around 12.7 Mt of low-emission hydrogen production capacity has been announced (9.3 Mt from water electrolysis), but only around 2.3 Mt is considered realistic by 2030. [18]

A similar gap appears in electrolyser deployment. The EU Hydrogen Strategy set a target of 40 GW of renewable hydrogen electrolysers by 2030 [19], while announced projects

now amount to about 84.2 GW. But only around 13 GW is considered realistic, with just 2.84 GW currently under construction.[18] This shows that the project pipeline is large on paper, but that actual implementation is moving much more slowly than policy targets require.

Nevertheless, the sector is moving forward. Installed electrolyser capacity in Europe increased from 52 MW in 2018 to 571 MW in 2025.[18] In 2024, the installed capacity was 376 MW (only about 6% of the 2024 target)[20] and produced ~ 65,000 t/y [20]of clean hydrogen, equal to only 0.6% of regional hydrogen demand of 7.87 Mt.

The EU also supports hydrogen through financial and market-building instruments. The European Hydrogen Bank [21], the Clean Hydrogen Partnership, and the European Clean Hydrogen Alliance [22]and the Hydrogen Mechanism platform [23] , to mention a few, are all there to provide funding, help coordination, and secure investment for hydrogen production and research. This addresses one of the main barriers to hydrogen deployment: producers need secure demand before investing, while industrial users need reliable supply before switching technologies.

1.4. Hydrogen Production Methods

Hydrogen is not a primary energy source, but an energy carrier. Therefore, its climate value depends mainly on how it is produced. There are a multitude of technologies available to produce hydrogen. These different technologies utilize a variety of raw materials, including fossil fuels, biomass, and water, and require different energy sources to drive the conversion processes. This energy can be supplied in many forms, such as nuclear heat, solar thermal energy, or electricity sourced from renewables, nuclear plants, or the existing power grid. [24] As a result, the environmental impacts and the cost of hydrogen, even if it is produced with the same technology, can vary significantly. Therefore, to differentiate between technologies and their carbon intensity (CO_2 emitted /kg H_2 produced), both in industry and research, a “colour” nomenclature is often used, even though this classification is not technically rigorous.[25], [26]

There is no universal agreement on a hydrogen “colour code”, which can lead to overlapping use or conflicting labels for the same production routes, creating confusion in communication and policymaking. International agencies such as the IEA suggests that international discussion should focus on emissions instead of colors. It recommends the use of labels such as “renewable,” “low-emission/low-carbon,” and “clean,” or to rely on technology-specific descriptions which should be tied to emission thresholds. [5], [6]

EU Hydrogen Strategy follows this approach by defining low-carbon hydrogen at 36.4 g CO_2-eq/MJ H_2, equal to about 4.4 kg CO_2-eq/kg H_2.[27] Other regions use their own values, China for example defined 14.5 kg CO_2/kg H_2 threshold for “low-carbon”

hydrogen and 4.9 kg CO_2/kg H_2 for “clean and renewable” hydrogen [28] and the US set a limit of 4.0 kgCO_2e/kgH_2 to qualify as clean. [24]

Nevertheless, the colour scheme became a shorthand for describing the carbon footprint and the technology behind hydrogen production. The most established and widely used colors are grey, blue, and green hydrogen, as they correspond to mature and already implemented production technologies.

1.4.1 Fossil based hydrogen

The most common hydrogen production route is steam methane reforming (SMR) of natural gas and coal gasification, accounting for 83% of the global hydrogen production in 2019. [5] But other reforming methods also fall into this category, including coal gasification, partial oxidation of methane (POM), partial oxidation of oil products (POX), and autothermal reforming (ATR). In some classifications, coal-derived hydrogen is further separated into black and brown hydrogen, depending on whether bituminous coal or lignite is used as the feedstock.

Both SMR and coal gasification produce hydrogen through the formation of synthesis gas, (CO and H_2) followed by the water–gas shift reaction, where CO reacts with steam to form CO_2 and additional H_2. The main difference is the feedstock, SMR uses natural gas (methane), while gasification uses solid carbonaceous materials, most commonly coal. [5] Coal gasification is generally considered the most CO_2 intensive method (approximately 19 - 20 kg CO_2/kg H_2 produced.) [5]While less intensive than coal, SMR still releases significant emissions, (typically ranging from 8.5 - 10 kg CO_2/kg H_2, considering direct emissions during production.[5]) The overall climate impact of natural gas-based hydrogen can increase substantially due to fugitive methane emissions during natural gas extraction and transport, since methane is a much stronger greenhouse gas than CO_2 over short time horizons. [29]

Hydrogen produced from fossil fuels with carbon capture, utilization and/or storage (CCUS) to reduce CO_2 emissions.[28] It is viewed as a bridging technology because it can be implemented using the already existing fossil-fuel-based hydrogen infrastructure. This makes it easier to deploy in the short to medium term than fully new green hydrogen systems. [26]The climate benefit of blue hydrogen is not always straightforward and strongly depends on several factors including: the technology being retrofitted; the achieved carbon capture rate; fugitive methane emissions; and the availability of suitable storage sites and infrastructure. Moreover, the overall emissions also depend on whether CO_2 is permanently stored or used for enhanced oil recovery (EOR), as well as the transport distance and method. Ideal capture rates above 90% are technically feasible, however, many currently operating hydrogen-CCUS facilities achieve only partial capture rates of around 56–60%. [29] In 2024, less than 1% of fossil fuel-based hydrogen production was equipped with CCUS. [20]Although the cumulative capture capacity of

these plants is estimated at around 12 Mtpa CO_2, only about 1 Mtpa is currently injected into dedicated geological storage. [29]

Reported carbon intensity values for blue hydrogen therefore vary widely. Under favorable conditions, values as low as 0.2–0.45 kg CO_2e/kg H_2 have been reported, assuming very low fugitive methane emissions and carbon capture rates approaching 98%.[28] In contrast, emissions as high as 14.5 kg CO_2e/kg H_2 have also been reported under conditions of high methane leakage (~3.5%), moderate capture rates (~56%), and when evaluated using a 20-year global warming potential for methane. [29], [30]

Global hydrogen consumption grew from approximately 90 million tonnes (Mt) of hydrogen in 2020 to nearly 100 Mt in 2024. [6] 99% of current supply is still produced via technologies based on fossil fuels. Therefore, there is a pressing need for the development of large-scale, and efficient green production methods.

1.4.2. Water electrolysis

In the past decades, water electrolysis has emerged as a key technology to produce low-emission hydrogen on a global-scale. [31]. In water electrolysis electrical energy is used to split water into hydrogen (H_2) and oxygen (O_2).

Overall reaction $$H_2O\ (l) \rightarrow H_2(g)\ + \frac{1}{2} O_2\ (g)$$ Eq. 3

This reaction requires an input of energy equal to the Gibbs free energy change (ΔG). At standard conditions (25 °C, 1 bar), ΔG = 237.2 kJ/mol [9], this value represents the portion of the reaction enthalpy that must be supplied as electrical work, i.e. the minimum energy input from the external power source. It corresponds to a standard reversible potential of 1.23 V. [32], [33]

$$\mathrm{U_{rev}} = \mathrm{E_0^R} = \frac{\Delta \mathrm{G_0^R}}{\mathrm{nF}} = \frac{237.21 \times 10^3\ \mathrm{J\ mol^{-1}}}{2 \times 96\,485\ \mathrm{C\ mol^{-1}}} = 1.229\ \mathrm{V}$$ Eq. 4

The full enthalpy change (ΔH) of water splitting at standard conditions (25 °C, 1 bar) amounts to 285.8 kJ/mol. [9] If the entire enthalpy is provided electrochemically, the corresponding cell voltage is the *thermoneutral potential*, 1.48 V at 25 °.

$$U_{tn} = \frac{\Delta H_0^R}{n \cdot F} = \frac{285.84 \times 10^3\ \mathrm{J\ mol^{-1}}}{2 \times 96{,}485\ \mathrm{C\ mol^{-1}}} = 1.481\ \mathrm{V}$$ Eq. 5

The difference between ΔH and ΔG (~48.6 kJ/mol) [9] represents the entropy term (TΔS). In practice, this entropy-related energy doesn't need to be supplied as electricity. Instead, it can be provided in the form of heat.

If this electricity is supplied from renewable sources, the process can be considered zero-emission, apart from emissions related to equipment manufacturing and construction. For grid-powered electrolysis, the environmental impact depends strongly on the electricity mix. Countries with high shares of renewables or hydropower can produce hydrogen with relatively low emissions such as Norway, Iceland, Canada. Fossil-fuel-heavy grids lead to higher carbon intensity.[26]

Despite its benefits, the widespread application is hindered by the inherently high electricity consumption and expensive cell materials. For a working electrolyser, the electrical energy input is determined by the applied cell voltage, current, and operating time.[8]

$$E = U \cdot I \cdot t \qquad \text{Eq. 6}$$

The rate of hydrogen production is directly linked to the current according to Faraday's law, meaning that higher current produces hydrogen at a higher rate. However, increasing the current density also increases the cell voltage, because larger kinetic, ohmic, and mass-transport losses must be overcome. Therefore, practical electrolyser energy consumption depends not only on the amount of hydrogen produced, but also on the operating current density and the corresponding cell voltage. Commercial electrolysers usually operate at 1.6–2.2 V, [32], [33]and commonly require around 50–80 kWh/kg H_2 [32], [33] This motivates alternative electrochemical routes in which the OER is replaced by a less demanding anodic reaction.

There are four main electrolysis technologies currently utilized or under development. The main water-electrolysis technologies differ primarily in their electrolyte, operating temperature, catalyst requirements, and technological maturity. Alkaline water electrolysis (AWE) and proton exchange membrane water electrolysis (PEMWE) are the most commercially established low-temperature technologies, but they differ substantially in terms of achievable current density, material requirements, and response to fluctuating power input. AWE is the most mature and widely established electrolyzer technology for hydrogen production, accounting for about 60% of global installed capacity and additions. [6] PEMWE systems are particularly suitable for applications requiring compact design, fast response, and operation under fluctuating electricity supply. This makes it more suitable for coupling with intermittent renewable electricity. Solid oxide electrolysis cells (SOECs) operate at much higher temperatures and can partly replace electrical energy demand with external heat [8], [34]. This makes SOEC particularly attractive where waste heat, nuclear heat, geothermal heat, solar thermal energy, or heat from downstream synthesis processes can be integrated into the

system. Although high temperature operation introduces additional challenges related to materials stability and system durability. Anion exchange membrane water electrolysis (AEMWE) represents a newer approach that combines a membrane-based cell design with alkaline operating conditions and the potential use of non-precious metal catalysts. The key characteristics, advantages, and limitations of these technologies are summarized in **TABLE 1**.

***TABLE 1** | Comparison of the main water-electrolysis technologies with respect to their electrolyte and charge carrier, typical operating conditions, key advantages, limitations, and technological maturity.*

Technology	Electrolyte / charge carrier	Typical operating conditions	Main advantages	Main limitations	Maturity
AWE [33]	Liquid 20–40 wt.% KOH or NaOH with a pH close to 14.; **OH^-** transport through a diaphragm	60–80 °C; 0.1–0.5 A/cm^2; 1.8–2.4 V	Established technology; comparatively low-cost materials; Ni-based catalysts can be used	Lower current density; limited dynamic response; gas crossover through the diaphragm	TRL 9–10
PEMWE [32]	Solid proton-conducting membrane, typically PFSA; **H^+** transport	60–80 °C; 1–2.2 A/cm^2; 1.8–2.2 V	Compact design; high current density; rapid response to fluctuating power input	High capital cost; requires corrosion-resistant components and noble-metal catalysts, particularly Ir at the anode	TRL 9
SOEC [8], [35]	Dense ceramic electrolyte, yttria-stabilized zirconia (YSZ), or gadolinium-doped ceria (GDC). [53]; **O^{2-}** transport	700–1000 °C; 0.3–1.0 A cm^{-2}; approximately 1.2 V	Part of the energy demand can be supplied as heat; high electrical efficiency; possible co-electrolysis of H_2O and CO_2	High-temperature materials degradation; thermal expansion mismatch; sealing challenges	TRL 7–8
AEMWE	Solid alkaline membrane; **OH^-** transport	Low-temperature operation	Potential use of low-cost, non-precious metal catalysts; combines membrane-based design with alkaline chemistry	Lower technological maturity; membrane stability and durability remain limiting factors	Emerging

2. Sulfur depolarized electrolysis

Sulfur depolarized electrolysis (SDE) is a promising alternative to water electrolysis. In the SDE cell, SO_2 is oxidized at the anode to form H_2SO_4, while protons are reduced at the cathode to produce H_2. [36], [37] The oxidation of SO_2 takes place at the anode, where it reacts with water to produce sulfuric acid, hydrogen ions and electrons. The hydrogen ions migrate through the electrolyte to reach the cathode where they recombine with the incoming electrons to form pure hydrogen gas. [8]

Anode half reaction:	$SO_2(aq) + 2H_2O\ (l) \rightarrow \mathrm{H_2}SO_4(l) + 2H^+ + 2e^-$	E°= 0.158V (vs RHE)	Eq.7
Cathode half reaction:	$2H^+ + 2e^- \rightarrow H_2(g)$	E° = 0.0V (vs RHE)	Eq.8

The intrinsic advantage of SDE is that by replacing the OER with the electrochemical oxidation of SO_2, the reversible potential is lowered from 1.23 V to 0.158 V (vs. RHE) [9]. This thermodynamic benefit could translate directly into substantial energy savings and a reduction in the cost of green hydrogen. Additionally, it allows the use of less expensive carbon-based cell components, such as graphite flow fields and carbon-based diffusion layers. SDE also generates sulfuric acid, which is a highly sought after chemical (with ~300 Mt produced in 2025 [38]) making it valuable by-product.

Compared with conventional electrolyser technologies, which are mature and commercially deployed, SDE stands at a much lower technology readiness level (TRL). Technology is still in an early stage of development, with most research limited to laboratory-scale cells and short-term experimental studies.

2.1. Origins of SDE: The Hybrid Sulfur Process

SDE was originally conceived as the electrochemical step of a thermochemical water-splitting method called the Hybrid Sulphur (HyS) cycle (Figure 1) developed by the Westinghouse Corporation. [36] It was originally developed in the 1970s, the process combined a high-temperature thermochemical step with a low-temperature electrochemical step. [7] More recently, SDE is also being considered as standalone technology where SO_2-containing waste streams are available. This would allow a toxic and environmentally harmful gas stream to turn into valuable industrial chemicals. [39]

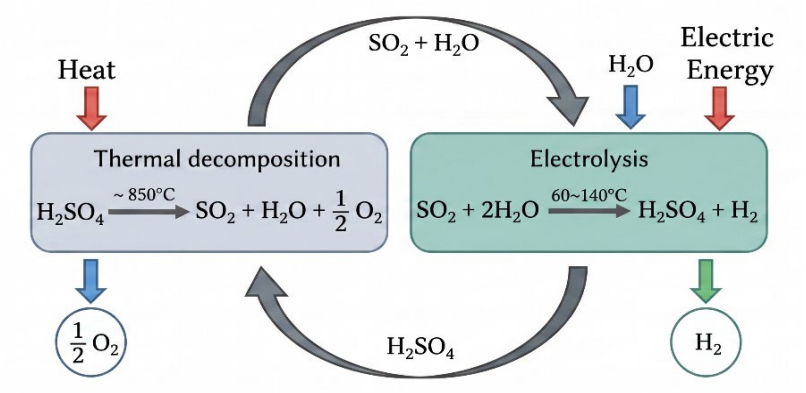

FIGURE 1 | Schematic illustration of the HyS process. Adapted from [54]

Thermochemical step:	$H_2SO_4(aq) \rightarrow SO_2(g) + \frac{1}{2}O_2(g) + H_2O(g)$	850-1000 °C	Eq.9
Electrochemical step:	$SO_2(aq) + 2H_2O\ (l) \rightarrow H_2SO_4(aq) + H_2(g)$	E°= 0.158 V	Eq.10
Overall reaction:	$H_2O\ (l) \rightarrow H_2(g) + \frac{1}{2}O_2\ (g)$		Eq.11

In the thermochemical step, sulfuric acid (H_2SO_4) is decomposed into sulfur dioxide (SO_2), oxygen (O_2), and water (H_2O) at temperatures between 850 - 1000°C. This requisite heat can be supplied directly by nuclear or solar sources, making use of thermal energy that would otherwise be lost or difficult to convert efficiently into electricity. In the following electrochemical step SO_2 reacts electrochemically with water to produce H_2 and regenerate the sulfuric acid. This closes the cycle and achieves water splitting with part of the energy supplied as heat and part as electricity.

The original Westinghouse setup was based on a parallel plate electrolyzer divided into two liquid compartments by a microporous rubber diaphragm, which separated the circulating anolyte and catholyte streams. Although this arrangement demonstrated the feasibility of low-voltage SO_2 oxidation, it was characterized by high electrode overpotentials, significant ohmic resistances, low SO_2 solubility, and high catalyst loadings (7–10 mg Pt/cm2). Initial operation achieved cell voltages below 0.8 V at 200 mA/cm2 in 50 wt% H_2SO_4. [7] Although later technical improvement reduced the achievable voltage to approximately 0.68 V at 200 mA/cm2 and 0.91 V at 400 mA/cm2 under the same acid concentration, performance remained low. [8]

Since then, a more compact membrane-electrode assembly (MEA) design was adopted. In the late 2000s, Gorensek et al. conducted a preliminary techno-economic evaluation at Savannah River National Laboratory (SRNL) and defined performance targets for cost-competitive operation, setting a benchmark of ≤0.6 V at 500 mA/cm$_2$ while producing ≥65

wt% sulfuric acid. For sustainable operation at temperatures ≥100 °C and pressures ≥10 bar was targeted. [40] These targets subsequently became an unofficial benchmark in SDE research, with later studies from other groups at University of South Carolina (USC) [41], [42] and at the Institute of Nuclear and New Energy Technology (INET) [43] explicitly comparing their results against this baseline.

2.2. Components of a sulfur depolarized electrolyser

SDE cells utilize proton exchange membrane (PEM) technology, which has enabled the transition from early parallel-plate designs to a much more compact design (Figure 2). This current architecture utilizes a membrane electrode assembly (MEA) configuration just like those found in PEMWE and PEMFC, currently borrowing components and design principles from both technologies. The MEA has a sandwich-like structure consisting of three primary functional components. In the middle is the polymer electrolyte membrane, which provides the essential path for proton transmission and is most often made of perfluorosulfonic acid (PFSA) polymer such as Nafion®. The membrane is bordered by electrodes (the anode and cathode catalyst layers) where the specific oxidation and reduction reactions occur. Finally, the structure incorporates porous transport media (PTM) in the form of carbon-based gas diffusion layers (GDL). Commonly used materials include carbon paper, graphite felt, or carbon cloth. GDL is to provide mechanical stability, good electrical contact and distribute reactants.

Electrodes are commonly implemented in one of two configurations. The catalyst layers, most often supported platinum (Pt/C), can be applied either directly onto the membrane or onto the gas diffusion layers, resulting in catalyst coated membrane (CCM) or gas diffusion electrode (GDE) which is then pressed against the membrane, respectively. The resulting MEA is placed between two electrically conducting flow fields. To ensure proper electrical isolation**,** insulation layers like Kynar or fiberglass are positioned between the flow fields and the outer structural components. The entire cell is held together by tightened bolts that compress the assembly to prevent leakage and maintain consistent electrical continuity across all layers.

2.2.1. The gas diffusion layer

A GDL is a type of porous transport media characterized by high porosity, typically > 50% [44], usually made from carbon-based material such as carbon paper, carbon felt, or carbon cloth. [45] It is positioned between the flow-field plates and the catalyst layers (CL) on both the anode and cathode sides of the MEA. Its primary function is to facilitate efficient mass-transport between the flow-field plates and the catalyst layers. It ensures the equal distribution of reactants to the active sites and the efficient removal of products. Additionally, the GDL provides a pathway for electron conduction, facilitates heat dissipation during operation, and provides mechanical stability for the MEA. [46]

The GDL typically consists of two structurally distinct layers: a macroporous substrate and a microporous layer (MPL). [47] The substrate is a porous carbon-fiber network that largely determines the bulk properties of the GDL. The length, diameter, and orientation of the fibers will define its fundamental properties including porosity, permeability, electrical conductivity, compressibility, and mechanical strength. [47], [48] The MPL is positioned on the membrane-facing side of the GDL and usually consists of carbon black mixed with a hydrophobic agent, most commonly polytetrafluoroethylene (PTFE). The different pore sizes of the substrate and the MPL results in a pore-size and capillary-pressure gradient which facilitates product removal from the catalyst layer toward the flow field [46], [47]. In addition, the MPL provides a smoother and higher-surface-area interface, thereby reducing interfacial contact resistance between the catalyst layer and the GDL. It also protects the membrane and CL from the rough surface of the carbon-fiber substrate and helps prevent carbon fibers from penetrating into the membrane. [44], [49]

The use of GDLs is well established in PEMFCs, [50] [47] [45]and numerous studies have investigated how GDL material, structure, porosity, thickness, wettability, and MPL design affect fuel cell performance.[48], [49], [51] In PEMFCs, GDLs are optimized to balance reactant transport with product-water removal, since excess liquid water can cause flooding, block gas-transport pathways, and hinder oxygen diffusion to the catalyst layer. [47]

Since water is not a product that must be removed, but rather a reactant, conclusions from PEMFC studies cannot be directly transferred to SDE operation. Material properties beneficial under fuel cell conditions may become disadvantageous in SDEs. For example, in PEMFCs, excess liquid water must be removed to avoid flooding, whereas in SDEs a flooded or highly wet environment is advantageous. The reaction needs water to be readily available for it to happen, furthermore it affects the resulting acid concentration and contributes to membrane hydration, both of which are important operating parameters that will be discussed in detail in a later section. Optimizing the structural characteristics of the GDL could contribute significantly to the further development of SDE technology, however, a clear correlation between structural properties and electrochemical performance is still lacking.

The following section provides a summary of essential GDL characteristics to highlight why reliable structure–performance correlations are challenging to establish.

Gas diffusion layer properties

TABLE 2 | *Summary of key GDL properties and their main effects on cell operation.*

Property	Representative parameters	Main effect on GDL and cell performance
Thickness	Uncompressed thickness Compressed thickness	Determines the transport distance through the GDL and influences electrical resistance and mechanical stability.

Porosity and pore structure	Total porosity Pore-size distribution Tortuosity Connectivity	Governs the available void volume and pathways for gas and liquid transport. Larger or more connected pores generally facilitate transport, whereas tortuous or poorly connected structures increase mass-transfer resistance.
Permeability	Gas / liquid permeability, measured in the through-plane or in-plane direction	Through-plane permeability controls transport between the flow field and catalyst layer. In-plane permeability supports lateral redistribution of reactants and products beneath flow-field ribs.
PTFE treatment / wettability	PTFE loading Static contact angle	PTFE increases hydrophobicity and influences liquid-water retention and removal. Excessive PTFE can reduce pore volume and permeability, increasing mass-transport resistance.
Microporous layer (MPL)	Presence Thickness Structure and pore size PTFE content	Modifies the catalyst-facing interface, improves surface contact, and affects water distribution. However, it generally decreases overall permeability because of its smaller pores.
Electrical conductivity / resistance	In-plane and through-plane conductivity Bulk and contact resistance	In-plane conductivity supports lateral current distribution across the electrode. Through-plane conductivity and low contact resistance are required for efficient electron transfer between the catalyst layer, GDL, and flow field.
Compressibility	Thickness change or stress–strain behavior under compression	Compression improves electrical contact and reduces contact resistance. Excessive compression reduces pore volume and permeability, can hinder mass transport, and may cause GDL intrusion into flow-field channels.

Important GDL metrics include thickness, compressibility, surface treatment, permeability, and electrical resistance or conductivity. [46], [47] Surface treatment mainly refers to PTFE loading and the presence or absence of an MPL, both of which strongly affect wettability, pore accessibility, and interfacial contact. Permeability and electrical conductivity are often reported separately in the in-plane and through-plane directions because GDLs are inherently anisotropic materials. This anisotropy arises from the preferential orientation of carbon fibers within the sheet and from the geometry of the GDL itself, which is laterally wide but very thin. [48] For permeability, the through-plane direction is important, because fluids must pass across the GDL thickness. For current distribution, the in-plane conductivity is important, to effectively distribute the current laterally across the electrode surface.

Direct comparison of manufacturer-reported values or results from different GDL studies can be difficult due to the lack of standardization in measuring techniques.[50] Different characterization methods can yield different values for nominally the same property. For

example, mercury intrusion porosimetry (MIP) is a volume-based method: it estimates pore size from the pressure required to force mercury into accessible voids and can misidentify large surface openings as large pores, even if these pores do not go all the way through the membrane. [46], [47] As a result, MIP often gives larger mean pore sizes. In contrast, capillary flow porometry (CFP) is a flow-based method: it characterizes the constrictions that a gas must pass through when flowing entirely across the material. Therefore, CFP is more sensitive to the narrowest connected passages, or "bottlenecks", and can give substantially smaller mean pore sizes.[46], [47]

Mass transport through the GDL is governed by its microstructure including pore size, pore-size distribution, tortuosity, and connectivity. However, these parameters are difficult to characterize unambiguously because a GDL is not composed of isolated, well-defined pores, but of a highly interconnected fibrous network. [44], [50] The reported pore-size distributions span a wide range, often across several orders of magnitude, indicating that of micro-, meso-, and macropores coexist within the same material. The GDL substrates have a typical thickness of approximately 0.2–0.5 mm and, pore sizes in the range of 10–100 μm, while the mean pore size usually falls between 30 and 40 μm [44], [45], [47], [52]

Commercial GDLs usually include an MPL, although its thickness can vary considerably. MPL thicknesses in the range of approximately 10–150 μm have been investigated, while commercial GDLs typically employ MPLs thinner than 50 μm. [53] The pore sizes in the MPL are much smaller than those of the macroporous substrate, commonly falling in the range of roughly 20–200 nm. It generally contains a high PTFE loading (~15-30 wt.%) [53] and is usually characterized by a comparatively smooth surface although cracks, ranging from 5 to 15 μm in width[47], have been frequently observed. Furthermore, the addition of the MPL typically results in a significant decrease in the overall gas and water permeability. [44]

PTFE coating is another surface treatment often applied to GDLs. Compared to the MPL, which mainly modifies the catalyst-facing surface, PTFE treatment acts as a bulk method because it modifies the internal carbon-fiber surfaces throughout the porous substrate.[47] Its purpose is to increase hydrophobicity and thereby facilitate liquid-water removal from the GDL. Typical PTFE loadings are commonly in the range of 5–30 wt.%. [46] However, the PTFE distribution is often not perfectly uniform: accumulate at fiber–fiber intersections and partially occupy smaller pores. [46]As the PTFE loading increases, the GDL becomes more hydrophobic, but the available pore volume decreases, reducing porosity, and permeability, increasing mass-transport resistance[45], [46].

Compressibility is another GDL property. During cell assembly, the electrolyzer is clamped together to prevent leakage. Realistic transport-property testing commonly covers the 0.5–3 MPa range to reflect these actual loading conditions.[54] In the reviewed

literature, clamping pressures of 1.5 MPa, 1.61 MPa,[55] and 2.0–2.5 MPa[44] have been reported. This clamping pressure applies mechanical stress to the GDL, causing deformation and a reduction in thickness. [47] As a result, the pore structure can be distorted, which changes permeability and alters mass transport through the layer. At the same time, compression can improve electrical contact, [48] reducing both bulk resistance and interfacial contact resistance. It is important to avoid over compression which can reduce pore volume to such an extent that mass-transfer becomes greatly hindered. It can also cause the material to intrude into the flow fields flow channels resulting in increased pressure drop and non-uniform distribution of the reactants. [47] Repeated or high compression can lead to irreversible thickness changes and microstructural damage, further altering transport and resistance properties. [50]

GDLs are primarily manufactured from polyacrylonitrile (PAN) fibers, which are considered the most attractive precursor due to their high carbon yield and superior mechanical properties. [46] The specific way these fibers are processed and structured determines the final material's characteristics, resulting in products with different properties. While commercial GDL materials are commonly labeled as carbon paper, carbon cloth, or carbon felt, these terms are often used without technical rigor. Both carbon paper and carbon felt are considered non-woven materials because they consist of fibers that are randomly oriented and stacked into a web-like matrix. The main difference being how the fibers are held together. [46], [47]

In a carbon paper the fibers are glued together by a polymeric binder typically phenolic resin. [44] During its manufacturing the fibers are preferentially aligned parallel to the material surface resulting in significant anisotropy in its electrical and thermal properties. [46]It is characterized by relatively high tortuosity and smooth surface but compared to carbon cloth or carbon felt is mechanically rigid and brittle.[49] Carbon felt, however, is held together by mechanical bonding through hydroentangling, a process using high-pressure water jets to entwine the fibers. This creates a "spaghetti" fiber structure with randomly curved fibers oriented in both the through-plane and in-plane directions. [44] Finally, carbon cloth is a woven substrate fabricated from spun PAN yarns, creating a very tight fabric that maintains its structural integrity without the need for additional binders. [46]

In this study, GDLs manufactured by SGL Carbon and Freudenberg were evaluated. The SGL Carbon GDL can be classified as a carbon-paper-based substrate, whereas the Freudenberg GDL is structurally closer to carbon felt. [46], [50]

2.2.2. Membrane selection

Beyond enabling sufficient water transport, the membrane must also provide high proton conductivity so that protons can be transferred to the cathode with minimal ohmic losses. [56] At the same time, it must limit SO_2 crossover, since SO_2 reaching the cathode can undergo parasitic reduction reactions that lower efficiency and contaminate the

hydrogen product, as discussed in the following section. These transport requirements must be met while maintaining chemical and mechanical stability under hot, strongly acidic, and oxidizing operating conditions. Therefore, although proton conductivity and the diffusion of neutral species such as water and SO_2 depend on operating parameters including temperature, pressure, acid concentration, and membrane water content, they are fundamentally determined by the membrane material and its transport properties. This makes membrane selection a key factor to enable high performance and long-term durability.

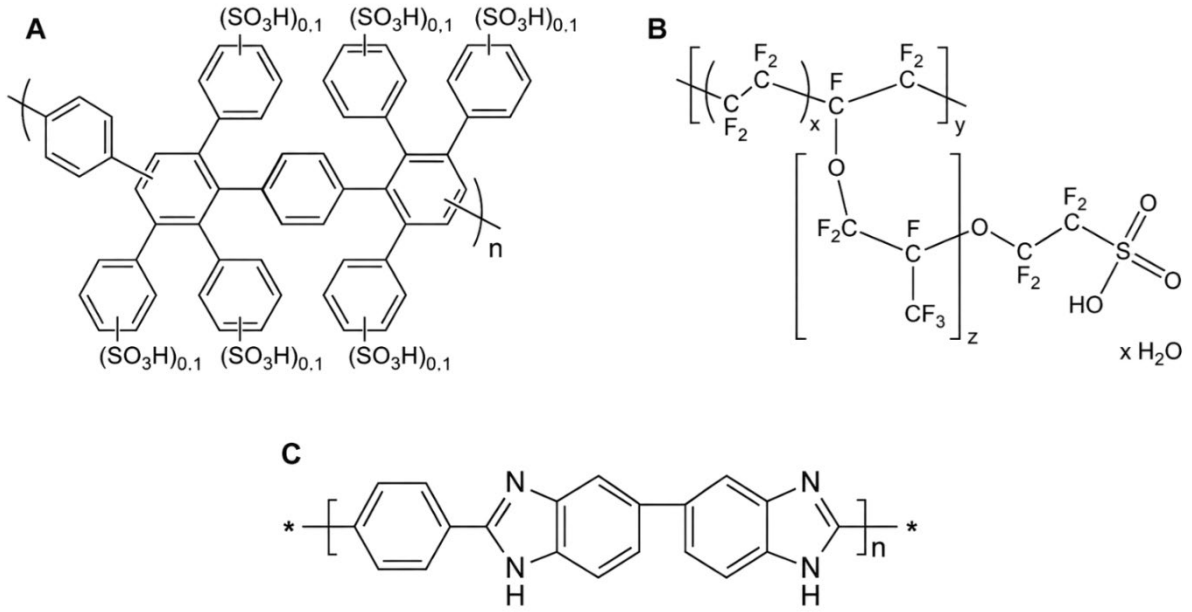

***FIGURE 2** | Chemical structures of proton-conducting membrane materials investigated for sulfur dioxide-depolarized electrolysis: (A) sulfonated Diels–Alder poly(phenylene) [57] (SDAPP), (B) Nafion® [57], and (C) polybenzimidazole (PBI).[63]*

The most employed membranes are PFSA ionomers, typically Nafion® [56], [57] Nafion is a perfluorinated copolymer consisting of a hydrophobic PTFE backbone with perfluorinated side chains terminated by hydrophilic sulfonic acid groups. The PTFE backbone provides good chemical and mechanical stability, while the sulfonic acid side chains enable proton transport.[58] Nafion is also commercially widely available in several thickness grades, such as N115, N117, N212 and MEA fabrication methods such as hot-pressing and direct catalyst painting are mature and routinely utilized. Although these membranes offer high proton conductivity, this ability is strictly dependent on the level of hydration. When hydrated, the hydrophilic side chains cluster to form interconnected, water-filled channels that serve as pathways for proton transport. [58] This dependence generally restricts Nafion operation to temperatures below about 100 °C, because liquid-phase water must be retained within the membrane; operation above this range therefore requires pressurization. [59] It also limits the viable sulfuric acid

concentration, since concentrated acid promotes membrane dehydration, shrinking of the ion-conducting channels, and increased ohmic resistance. [60] Furthermore, Nafion exhibits relatively high permeability to gases such as SO_2. [61] For these reasons, its viability in SDE applications (where elevated temperature, strongly acidic media, and SO_2 crossover are of concern), has been contested, and current research is investigating alternative membrane materials.

Sulfonated Diels–Alder polyphenylene (SDAPP) membranes have been investigated as a candidate to replace Nafion. [59], [62] SDAPP membranes are a sub-class of sulfonated polyphenylenes synthesized via a Diels–Alder reaction to construct a backbone comprised entirely of stable aryl–aryl bonds.[57] Similarly to Nafion, the structure is functionalized by directly attaching sulfonic acid groups to the framework, creating the strongly acidic ionic sites. Therefore, SDAPP membranes conduct protons essentially through same mechanism as PFSA membranes. As a results SDAPP membranes show superior thermal stability at temperatures up to 285 °C, due to all-aromatic backbone which is chemically exceptionally robust because it lacks the labile heteroatom linkages found in other polyaromatics. [57] However, their proton conductivity still depends strongly on membrane water content [59] therefore, pressurization is required in order to take full advantage of their high thermal stability.

Polybenzimidazole (PBI) membranes serve as another alternative to Nafion. PBI-s are a family of aromatic heterocyclic polymers which consist of an aromatic heterocyclic backbone built from repeating benzimidazole units. [56], [63] This PBI backbone is not inherently proton conducting on his own. To function as an electrolyte, the membrane must be doped with acids such as phosphoric acid (H_3PO_4) or sulfuric acid (H_2SO_4), to impart necessary high ionic conductivity. Similar to SDAPP, the rigid aromatic backbone of PBI membranes results in high thermal (~200 C) and chemical stability.[63] However, unlike Nafion, proton transport in doped PBI relies on acidic species rather than water molecules, enabling operation even under anhydrous conditions. The absence of water channels inherently reduces the transport of small neutral molecules, such as SO_2 across the membrane. [61] It also reduces the dependence of the ohmic resistance on the membrane hydration level. [41]

Staser et al. [60] and Garrick et al. [41] used to sulfonated polybenzimidazole (s-PBI) membranes and demonstrated better performance compared to Nafion, due to the above-mentioned benefits. They also highlighted the issue of possible acid leaching, noting that contact with liquid water on the cathode side can wash out the essential acid dopants and lead to a gradual reduction in membrane conductivity. Therefore, SDE cells with s-PBI membrane require that the cathode is kept dry and the SO_2 feed is humidified before entering the anode compartment.

2.2.3. Current state of catalysis

The anodic kinetic overpotential represents the primary source of inefficiency in SDE. While the reversible potential for SO_2 oxidation is 0.158 V, significantly lower than that of OER (1.23 V) the electrochemical oxidation is similarly sluggish and requires substantial activation energy. [64] This inherent kinetic barrier leads to large overpotentials often around 0.4 V [65], necessitating adequate electrocatalysis.

Over the past decades, extensive research has been devoted to the electrochemical oxidation of SO_2 in acidic media, including studies of the reaction mechanism, kinetics, mass-transport limitations, electrolyte composition, and electrode preconditioning. However, a comprehensive review of all aspects of this topic is beyond the scope of this work; instead, only a broad overview of the main current research trends in SDE will be provided.

Mechanistic studies are normally carried out using rotating disk electrodes with polished Pt surfaces under well-defined laboratory conditions. [66], [67], [68] While such experiments provide valuable fundamental insight, they are generally performed at low current densities and under potential regimes that differ substantially from those encountered during practical SDE operation. Despite research efforts the elementary steps and reaction intermediates involved in SO_2 electrooxidation remain unresolved, and no generally accepted mechanism has yet been established. As highlighted in the critical review by O'Brien et al [69], there is "widespread disagreement in the literature", with the apparent reaction pathway depending strongly on the electrode material, electrolyte pH and acid concentration, surface state, applied potential, and electrode pre-conditioning history.

Ungerer et al. used density functional theory (DFT) calculations to study the competitive adsorption of H_2O and SO_2 on catalytically relevant platinum surfaces. [70] Their results showed that SO_2 adsorbs more strongly than H_2O on all investigated Pt surfaces, with the adsorption strength decreasing in the order Pt(001) > Pt(011) > Pt(111). [71] This indicates that SO_2 can preferentially occupy and displace water on the active sites, which is important because water activation is required for the overall SO_2 oxidation reaction. The authors therefore suggested that high SO_2 coverage may limit water access to the catalyst surface ultimately inhibiting the reaction. [70]

O'Brien et al. further showed experimentally that the electrochemical behavior of Pt is strongly affected by surface preconditioning. [67] At potentials lower than approximately 0.45 V to 0.6 V vs. SHE, SO_2 undergoes reduction to sulfur-containing surface species, forming a sulfur adlayer on Pt. They claimed that depending on its coverage, this layer can either promote SO_2 oxidation or inhibit it by blocking the active surface. [65] They found that above approximately 0.9 V vs. SHE Pt oxide formation becomes more significant which further affects the SO_2 oxidation.

In the context of SDE, early research has mainly focused on testing and screening different anode materials to identify catalysts with sufficient activity, acceptable cost, and adequate stability under the acidic operating conditions.

Díaz-Abad et al. provided an overview of the different anodic materials that have been tested. [66] Early studies examined pure noble metals such as Pt, Pd, Ir, and Au with Pt showing consistently good performance and becoming the standard benchmark for SDE. Since then, Pt-based bimetallic and alloy catalysts, such as Pt–Cr, Pt–Ru, and Pt–Pd, have been investigated to improve activity and reduce reliance on Pt. Core–shell catalyst architectures were also explored as another strategy to lower noble-metal loading and improve catalyst utilization. Additionally, alternative supports for platinum have been investigated, including activated carbon, reduced graphene oxide (RGO), and SiC/TiC binary carbides, which show high electrochemical stability in corrosive acidic environment.

Pt supported on carbon (Pt/C) remains the standard for SDE anodes. It shows high catalytic activity and good corrosion resistance, and it has mature production processes. But due to its high price, recent studies have focused on decreasing the Pt loading and improving the way the catalyst is deposited. In early SDE development, platinum loadings were as high as 10 mg Pt/cm^2, whereas modern Pt/C-based SDE studies typically use loadings of about 1.0–2.0 mg Pt/cm^2; loadings below 0.5 mg Pt/cm^2 [88], [89] are generally considered *"ultra-low"*. [89], [90]

Díaz-Abad et al. [72] compared airbrushing with electrospray deposition for *"ultra-low"* Pt electrodes and found that electrospray gave better performance due to improved catalyst dispersion; however, the absolute current density remained relatively low, with the best performance staying below 400 mA/cm^2 at 1.0 V and 110 °C.

A recent study by Tian et al. [73] followed a different approach. They used a total loading of 0.42 mg Pt/cm^2 but varied the distribution between the GDL (graphite felt) and the membrane surface. The authors claimed that the resulting "three-dimensional" electrode allows for better contact between dissolved SO_2 and the catalyst. They observed the highest current density when the ratio of Pt on the GDL to the PEM was 3:1 (anode side). They reported a current density of 1.6 A/cm^2 at 1.05 V, 80 °C, with 30 wt% H_2SO_4.

Besides Pt-based catalysts, gold (Au) has emerged as a promising candidate for SO_2 oxidation. This was demonstrated by Meekins et al. in a USC/SRNL study, where they compared commercial Au/C and Pt/C catalysts. Both metal were used at a low anode loading of 0.1 mg$_{metal}$/cm^2, with 0.3 mg Pt/cm^2 on the cathode. Au/C exhibited a lower onset potential, reached higher current densities and better short-term stability, which the authors claimed to highlight gold's lower susceptibility to poisoning by adsorbed sulfur species. The authors further suggested that increasing the Au loading from 0.1 to 0.5 mg Au/cm^2 could allow the cell to approach the target of 0.5 A/cm^2 at 0.6 V. Their

results indicated that Au-based catalysts may provide an alternative route for improving SDE performance, although its cost and long-term durability still needs to be investigated. [74]

Roessler et al. [75]reported similar results in a recent study that investigated the effects of asymmetrical catalyst loadings. They found that the best results came from an asymmetrical loading of 0.1 mg Au/cm^2 and a cathode loading of 0.3 mg Pt/cm^2, which achieved a high current density of 0.54 A/cm^2. This strategy successfully reduced platinum usage by 50% and decreased the overall metal loading by approximately 30%. The researchers also noted that increasing the operating temperature from 20 to 80 °*C* nearly tripled the cell's efficiency. However, they found that 0.1 mg Au/cm^2 represents a critical threshold, as lower loadings result in instant deactivation because the catalyst layer becomes too thin.

2.2.4. On the use of carbon materials

Although SDE is an electrolysis process, its material-selection is technically closer to PEMFC technology than to PEMWE. In PEMFCs, carbon materials are extensively used because of their high electrical conductivity, low cost and abundance, ease of machining, and good chemical stability. [76] Accordingly, SDE can utilize carbon-based components from PEMFCs, including graphite flow fields, carbon-based GDLs and carbon-supported catalyst materials. In contrast the use of carbon materials in PEMWE is limited, particularly on the anode side, due to rapid carbon corrosion. Carbon corrosion is the electrochemical oxidation of carbon to CO_2 and CO. [50], [76], [77]

$$C + 2H_2O \rightarrow CO_2 + 4H^+ + 4e^- \qquad E° = 0.207\ V\ (vs\ RHE) \qquad Eq.12$$

$$C + 2H_2O \rightarrow CO + 2H^+ + 2e^- \qquad E° = 0.518\ V\ (vs\ RHE) \qquad Eq.13$$

It leads to material loss and structural damage ultimately compromising the performance and long-term operation of the electrolyzer. The low reversible potential of these reactions means that the reaction is thermodynamically favorable under all practical conditions. In practice, the kinetics of the reaction are so strongly hindered that corrosion remains negligible below ~1.0 V, the exact onset depending on the graphite type and local reaction conditions.[77] Carbon corrosion accelerates sharply once electrode potentials exceed 1.2 V vs RHE, and becomes rapid and destructive above ~1.4 V, where CO_2 evolution and structural breakdown are observed within short time scales. [76]

This makes the utilization of carbon-based components completely impractical for PEMWE where potentials are typically above 1.4 V and may exceed 2.0 V at high current density, making the use of expensive materials such as titanium and noble-metal oxides necessary. [78], [79] In contrast, SDE operates at significantly lower cell voltages.

Reported literature values are generally below 1.0 V, depending on current density, and remain limited to approximately 1.2 V even in the highest reported cases[80], [81]. Therefore, while carbon corrosion cannot be excluded entirely, its thermodynamic driving force, kinetic rate, and practical relevance are substantially reduced under SDE conditions. This enables the use of inexpensive carbon- and graphite-based components, together with mature fabrication routes originally developed for PEMFCs. This advantageous since titanium and some noble metals would readily corrode in high concentration sulfuric acid environment.

The relevant time scale must also be considered. Carbon corrosion in PEMFC and PEMEL research is evaluated against of tens of thousands of hours. Recent PEMWE studies have shown that carbon-based components can remain usable over experimentally relevant time scales despite being unsuitable for long-term commercial operation. Young et al. showed that carbon paper PTLs and graphite flow fields could be used for about 40 h of PEMWE testing, including 15 h at high voltages between 2 and 3 V.[79] Messing et al. further showed that uncoated carbon-composite bipolar plates could be used in a PEM electrolyzer for 567 h under alternating current densities of 1 and 3 A/cm^2, with low degradation rates. [78] This is relevant for SDE, where reported demonstrations currently reach only a few hundred hours at best and explains why in most cases carbon-corrosion is not considered. Long-term testing will be necessary to evaluate the extent of carbon corrosion and its effect on SDE cell performance and durability.

2.3. SDE operating methods

A number of different options regarding how to feed SO_2 to the system have been reported in literature. [82], [83], [84] Throughout this work, these distinct feeding options are referred to as the cell "configurations", differing fundamentally in the phase and delivery method of the incoming reactants. This is important because high SDE performance depends on efficient reactant supply to the active reaction sites, while simultaneously ensuring effective removal of the sulfuric acid formed. Although several configurations have been explored gas-fed and liquid-fed configurations are the most employed.

In the liquid-fed configuration (FIGURE 3/1), a sulfuric acid solution saturated with SO_2 is supplied to the anode, and while not strictly necessary the cathode is typically fed with deionized water. The advantage of this configuration is that water management is less critical as the membrane is less prone to dehydration. Furthermore, the resulting acid concentration remains independent of other parameters, being primarily determined by the bulk anolyte composition. In the liquid-fed configuration, the availability of SO_2 at the electrode surface is the performance-limiting factor. This is directly tied to the SO_2 concentration in the anolyte —the upper limit of which is dictated by its solubility— and the diffusion rates through the liquid phase to the reaction sites. Both solubility and diffusion are functions of sulfuric acid concentration, operating temperature, and system pressure. This architecture has been investigated extensively at the Savannah River

National Laboratory (SRNL) [82] and Chinese Institute of Nuclear and New Energy Technology (INET) [43], with the main research focus directed toward improving SO_2 mass transfer and increasing the attainable sulfuric acid concentration without compromising cell performance.

In the gas-fed configuration (FIGURE 3/2), anhydrous SO_2 is supplied directly to the anode, while liquid water is supplied to cathode side. To facilitate the reaction, water must first diffuse through the membrane to the anode to react with SO_2 and form sulfuric acid. This configuration avoids the SO_2 mass-transport limitations however, because all water required for the reaction must cross the membrane, water management becomes critical. In this design, water serves a triple role: it acts as a reactant, determines the resulting sulfuric acid concentration, and maintains membrane hydration. This architecture was pioneered at the University of South Carolina (USC) [85], where research primarily focuses on improving the efficiency of water transport from the cathode to the anode, thus allow high performance.

Additional configurations have been evaluated in the literature, such as feeding SO_2 gas saturated with water vapor or utilizing SO_2 gas – liquid water mixtures as alternatives to acid solutions. [86] While these approaches remain viable, they are not the primary focus of current research and have not been as extensively covered as the liquid-fed or gas-fed configurations(FIGURE 3). In this work, we opted for the gas-fed configuration, which will serve as the primary focus of further discussion.

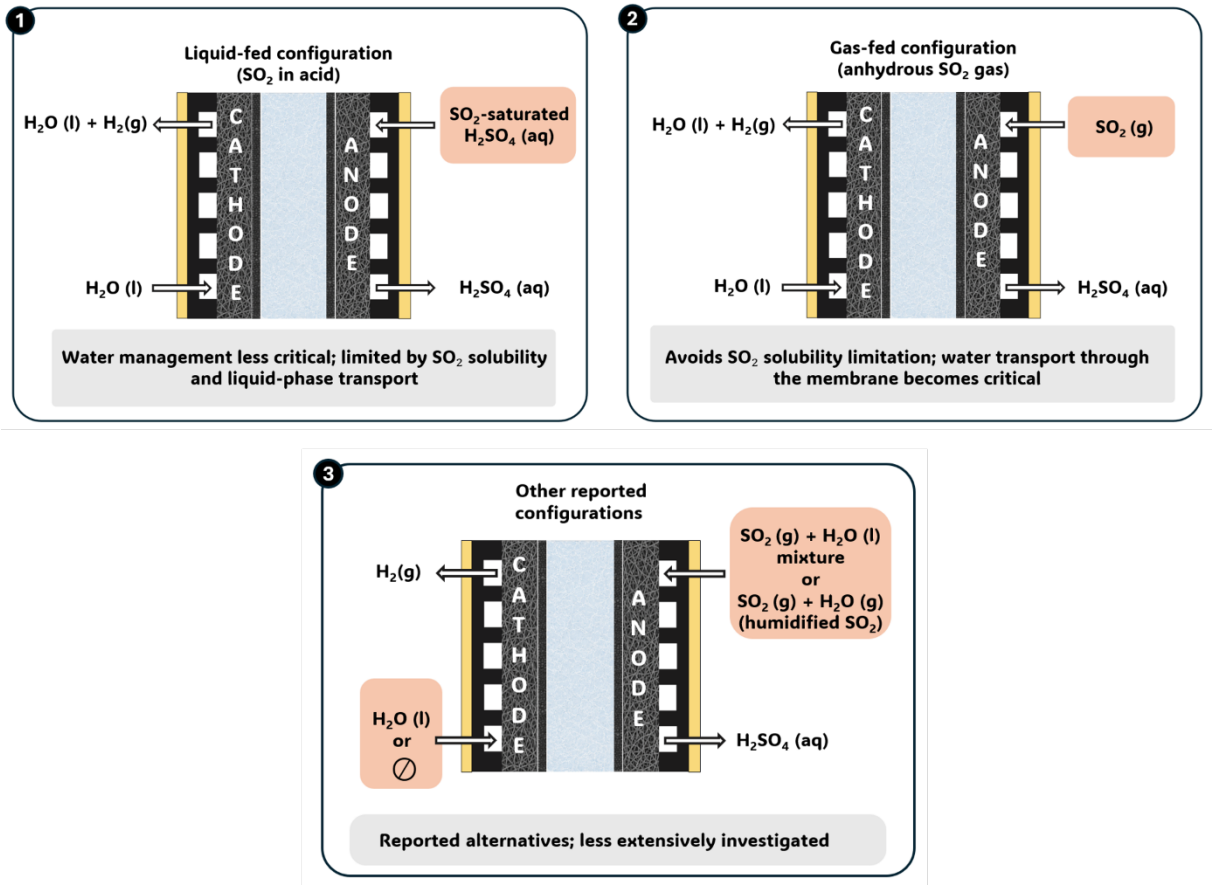

***FIGURE 3** | Overview of selected sulfur dioxide feeding configurations. 1) In liquid-fed operation, SO_2 is supplied dissolved in sulfuric acid, whereas in 2) gas-fed operation anhydrous SO_2 is supplied directly to the anode. 3) Additional concepts, including humidified SO_2 feeds and gas–liquid mixtures, have also been reported. The gas-fed configuration investigated in this work is highlighted.*

2.4. Membrane-mediated transport

2.4.1. Water management

As highlighted in the previous section, water plays a crucial role in SDE operation. It acts as a reactant in SO_2 oxidation, maintains membrane hydration, and dilutes the produced sulfuric acid while helping its efficient removal from the cell. This is especially important in gas-fed configurations, where all the required water is supplied from the cathode side and must first diffuse through the membrane before reaching the reaction site. Water management is therefore a complex aspect of SDE operation that directly influences cell performance.

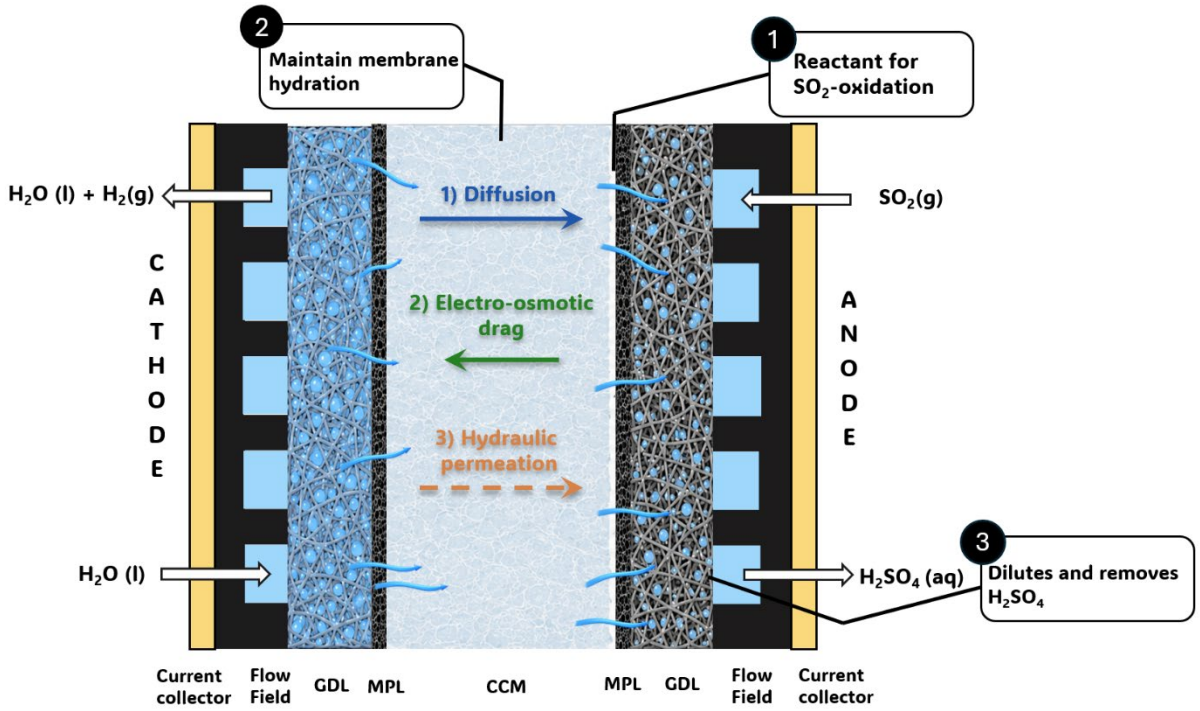

Figure 4* | *Schematic representation of water transport in the gas-fed SDE cell *Liquid water is supplied to the cathode, while gaseous SO_2 is supplied to the anode. The cell consists of current collectors, flow fields, gas diffusion layers (GDLs), microporous layers (MPLs), and the catalyst-coated membrane (CCM).*

*Water is transported from the cathode to the anode mainly by **1) diffusion** and **3) hydraulic permeation**, while **2) electro-osmotic drag** transports water in the opposite direction together with proton migration.*

*The numbered labels indicate the main roles of water in the cell: **(1)** water is required at the anode as a reactant for SO_2 oxidation, **(2)** water maintains membrane hydration, and **(3)** excess water dilutes and helps remove the produced H_2SO_4 from the anode.*

Staser et al. [42], [59], [87] investigated water management in a gas-fed PEM SDE electrolyzer using a combined mathematical and experimental approach. In their one-dimensional model, water transport across the membrane was described as the net result of diffusion, electro-osmotic drag, and hydraulic permeation caused by pressure differences across the membrane. Diffusion drives water toward the anode because the anolyte has a higher sulfuric acid concentration and therefore a lower water activity than the cathode side, where pure water is supplied. In contrast, electro-osmotic drag transports water with migrating protons toward the cathode during operation. A pressure difference may also be applied to promote hydraulic permeation and assist water transport across the membrane.

To support their model predictions, Staser et al. [87] carried out complementary experiments using Nafion N115, N117, and N212 membranes having a thickness of 125, 180, and 50 µm, respectively. The comparison indicated that thinner membranes facilitate greater water transport across the membrane, with N212 showing the highest apparent water flux. However, they also reported that, despite the better water transport

in thinner membrane, they found that sustaining operation at current densities above 0.6 A/cm^2 was generally not possible without applying a 600 kPa pressure differential to the cathode to actively assist water transport.

2.4.2. SO_2 Crossover

SO_2 crossover refers to the undesired transport of unreacted SO_2 species through the membrane from the anode to the cathode side and remains one of the technical challenges in SDE development.

Ding et al. investigated open-circuit conditions (OCV), where SO_2 is present in the cell but no external bias is applied. Under these conditions, SO2-crossover leads to the formation of internal galvanic cells, which may offset the applied working voltage during subsequent operation. The authors evaluated this behavior by measuring the OCV and related the measured values to possible redox couples, involving SO_2 oxidation on the anode side and SO_2 reduction on the cathode side. They argued that an appropriate external bias should be applied before SO_2 is introduced into the cell. This bias promotes SO_2 oxidation at the anode, consuming SO_2 and therefore suppressing SO_2 crossover.

Nevertheless, it remains an inherent risk of SDE operation, that cannot be completely eliminated, because SO_2 readily dissolves in the acidic, hydrated domains of the Nafion membrane and diffuses toward the cathode along its concentration gradient. Once SO_2 reaches the cathode, it can participate in several parasitic side reactions that can alter the apparent current (or voltage). Under the reducing conditions at the cathode, SO_2 can be electrochemically reduced first to elemental sulfur then to H_2S (Eq.14-16.) This has been observed previously in literature [80], [81] as well during some unsuccessful operation through this thesis, resulting in solid sulfur depositions in flowfields, cathode water and porous media. However, since a two-electrode setup was used in this work, the cathode potential was not monitored separately. A reference electrode would be required to directly determine cathode potential during operation.

$$SO_2(aq) + 4H^+ + 4e^- \rightarrow S(s) + 2H_2O(l)) \qquad E°= 0.45\ V\ vs\ RHE \qquad Eq.14$$

$$S(s) + 2H^+ + 2e^- \rightarrow H_2S(aq) \qquad E°= 0.14\ V\ vs\ RHE \qquad Eq.15$$

$$SO_2(aq) + 6e^- + 6H^+ \rightarrow H_2S\ (aq) + 2H_2O(l) \qquad E°= 0.35V\ vs\ RHE \qquad Eq.16$$

SO_2 can also be chemically reduced at the cathode side. In the presence of the produced H_2, SO_2 may react to form H_2S, while reaction with already formed H_2S can lead to elemental sulfur deposition (Eq. 18,18) [61], [82]

$$SO_2(aq) + 3H_2(g) \rightarrow H_2S(aq) + 2H_2O(l)) \qquad G° = -201.4\ kj/mol \qquad Eq.17$$

$$SO_2(aq) + 2H_2S\ (aq) \rightarrow 3S(s) + 2H_2O(l) \qquad G° = -117.9\ kj/mol \qquad Eq.18$$

The side reactions described by Eq. 14-16 contribute to the measured current and can therefore give the false impression of improved cell performance, even though this current is not associated with hydrogen evolution.[88] In other words, these reactions consume charge that would otherwise be used for hydrogen production which lowers the Faradaic efficiency of the cell.[80] Both SO_2 and H_2S contaminate the hydrogen stream, making costly downstream purification necessary. Over time, the resulting sulfur-containing species can poison the cathode catalyst, accumulate at the electrode–membrane interface, promote delamination of the MEA, and block transport pathways in the GDL and membrane. [80], [82]

Steimke et al. at SRNL [82] reported the most severe cases of SO_2 crossover. After 100 h of operation, they reported the formation of a thick sulfur-rich layer at the membrane–cathode interface. This deposit was reported to contain 58.7% sulfur and had grown to a thickness comparable to that of the membrane itself. The accumulation caused a sharp increase in cell voltage and eventually led to catastrophic delamination of the cathode from the membrane. To mitigate this SRNL developed an operating procedure based on maintaining the cell in a mass-transfer-limited regime. In this approach, the cell is operated below an "imaginary line" on an SO_2 molarity–current density map, so that SO_2 is consumed at the anode faster than it can be resupplied from the bulk anolyte. This minimizes the SO_2 concentration at the membrane surface and therefore reduces the driving force for crossover to the cathode. Although this starvation-type operation caused some increase in cell voltage, it drastically reduced SO_2 crossover. After implementing the strategy to limit crossover, they demonstrated operation continuously for over 200 hours (ten days). The cell was operated galvanostatically at 500 mA/cm^2 with a hydrogen production rate reaching 98% of theoretical efficiency. Post-test SEM analysis confirmed that the MEA remained in pristine condition without any sulfur layer formation [82]

Roessler et al. [80] adopted a similar strategy to mitigate SO_2 crossover by controlling the SO_2 stoichiometry (stoichiometry referring to the ratio between the SO_2 feed rate and its rate of consumption). Under their original, non-optimized operation at an SO_2 stoichiometry of 4.0 and cell voltages of 0.8 and 1.0 V, a white solid was observed in the cathode water, which turned yellow after filtration and was identified as elemental sulfur. analysis further showed sulfur deposition within the porous structure of the GDL, where it could block transport pathways. By increasing the operating voltage to 1.2 V and applying "SO_2-starved" conditions, visible solid formation was virtually eliminated, with only minor traces amounts detected. In this optimized approach, crossover was minimized by maintaining an SO_2 stoichiometry of 1.0, ensuring that SO_2 was consumed at the anode as fast as it was fed. Over 4 h of continuous operation, they reported a current density decrease by 0.1 mA/cm^{2}h under the optimized conditions, compared with 20 mA/cm^{2}h indicating significantly reduced degradation.

Staser et al. at USC also addressed SO_2 crossover. [88] They demonstrated that increasing water flux across the membrane can reduce SO_2 crossover, preferably by applying a pressure differential to drive water toward the anode. In their studies, they reported the use of pressure differentials of 600 kPa across the membrane. Interestingly, they reported that changing the SO_2 conversion between 20% and 80%, corresponding to a 5-fold to 1.25-fold SO_2 excess, had no noticeable effect on electrolyzer performance. This appears to contrast with the findings of Roessler et al. [80], although the difference may be related to the applied pressure differential in the USC studies. SEM analysis still showed some sulfur deposition within the GDL structure, but they did not report the same catastrophic delamination observed by SRNL. Thus, considered crossover to be minimal under their operating conditions and estimated that only about 0.35% of the SO_2 crossing the membrane was reduced to elemental sulfur at the cathode.

Elvington et al. carried out a systematic study on different membrane materials for SDE, testing both PFSA-type membranes (e.g., Nafion®) and non-PFSA candidates such as SDAPP, PBI, and perfluorocyclobutane-based polymers (BPVE, BPVE-6F). [61] Their work clearly demonstrated a trade-off between proton conductivity, SO_2 crossover, and overall electrolyzer performance. This relationship was summarized by the general observation that "*membranes with high conductivity and good performance also tended to exhibit high SO_2 transport, while membranes with low SO_2 transport suffered from low conductivity and weaker performance*."

The study also highlighted the development of sulfonated perfluorocyclobutyl aromatic ether (S-PFCB) membranes, such as BPVE and BPVE-6F, designed specifically for the HyS electrolyzer with the primary goal of suppressing SO_2 transport. When corrected for thickness, their SO_2 permeability was indeed significantly lower than Nafion.

2.5. Thermodynamics and the effect of operating conditions on performance

As mentioned in section 2, the main advantage of SDE is the low reversible cell voltage compared with conventional water electrolysis. This advantage comes from replacing the OER by the oxidation of SO_2. The overall electrochemical reaction can be written as:

$$\mathrm{SO_2(aq) + 2H_2O(l) \rightarrow SO_4^{2-}(aq) + 4H^+(aq) + H_2(g)} \qquad \text{Eq.19}$$

For this reaction, the standard Gibbs free energy and the standard reaction enthalpy are calculated from standard formation values, in **TABLE 3** according to Eq. 20 and Eq. 22.

$$\Delta_r G^\circ = \sum \Delta_f G^\circ_{\text{products}} - \sum \Delta_f G^\circ_{\text{reactants}} \qquad \text{Eq.20}$$

$$\Delta_r G^\circ = [-744.53 + 4(0) + 0] - [-300.676 + 2(-237.129)] = +30.404\ \mathrm{kJ/mol} \qquad \text{Eq.21}$$

$$\Delta_r H^\circ = \sum \Delta_f H^\circ_{\text{products}} - \sum \Delta_f H^\circ_{\text{reactants}} \quad \text{Eq.22}$$

$$\Delta_r H^\circ = [-909.27 + 4(0) + 0] - [-322.980 + 2(-285.830)] = -14.630\ \text{kJ/mol} \quad \text{Eq.23}$$

TABLE 3 | *Standard Gibbs free energies of formation ($\Delta_f G°$) and standard enthalpies of formation ($\Delta_f H°$) used to calculate the thermodynamic properties of the SO_2-depolarized electrolysis reaction. The values are given in kJ/mol and refer to standard conditions. The entries for H^+(aq) and H_2(g) are zero by convention, as they represent the reference states used for electrochemical thermodynamic calculations. The tabulated values were taken from [89].*

Species	$\Delta_f G^\circ$ [kJ/mol]	$\Delta_f H^\circ$ [kJ/mol]
SO_2(aq)	−300.676	−322.980
H_2O(l)	−237.129	−285.830
SO_4^{2-}(aq)	−744.53	−909.27
H^+(aq)	0	0
H_2(g)	0	0

The calculated value of $\Delta_r G°$ is positive. This means that the reaction is not spontaneous under standard conditions and that electrical work must be supplied to drive the reaction. However, the value is small compared with water electrolysis. In contrast, the reaction is exothermic with respect to enthalpy. The positive Gibbs free energy corresponds to a minimum reversible cell voltage of 0.158 V. (Eq. 24)

$$U_{\text{rev}} = \frac{\Delta G^\circ_R}{nF} = \frac{30.404 \times 10^3}{2 \times 96485} = \boxed{0.1576\ \text{V} \approx 0.158\ \text{V}} \quad \text{Eq.24}$$

The performance of an SDE cell typically evaluated in terms of the achieved at a given cell voltage, together with the sulfuric acid concentration produced or maintained during operation. With research groups generally aiming for the benchmark set by Gorensek et al. at SRNL which is 0.5 A/cm^2 at 0.6V with a resulting product concentration of 65 wt.% H_2SO_4. [40] Using Eq. 25, the electrical energy demand can be calculated. At the theoretical SDE voltage, the electrical energy demand is only 4.20 kWh/kgH_2. If the cell is operated at the SDE target of 0.6 V, this increases to 15.95 kWh/kgH_2. In this work, 1.2 V is used as the main operating point for evaluating the different GDL combinations, corresponding to 31.91 kWh/kgH_2. This is substantially higher than the thermodynamic minimum of SDE, but it is still below the energy demand expected for practical water electrolysis that lies in the range of 50–80 kWh/kgH_2. Table 4 summarizes the calculated

specific electrical energy demands for the relevant SDE operating voltages and for theoretical water electrolysis as a reference.

$$E_{\text{spec}} = \frac{U \cdot 2F}{M_{\text{H}_2} \cdot 3.6 \times 10^6} = \frac{U \cdot 2 \cdot 96485\ \text{C/mol}}{2.016 \times 10^{-3}\ \text{kg/mol} \cdot 3.6 \times 10^6} = 26.59 \cdot U \qquad \text{Eq.27}$$

***TABLE 4**: Comparison of the calculated specific electrical energy demand at different SDE and water electrolysis voltages.*

Case	Voltage [V]	Calculation	Electrical energy demand [kWh/kgH_2]
SDE theoretical	0.158	26.59 · 0.158	4.20
SDE target	0.6	26.59 · 0.6	15.95
SDE at 1.2 V	1.2	26.59 · 1.2	31.91
WE theoretical	1.229	26.59 · 1.229	32.68
WE	1.8–2.2	26.59 · 1.8 26.59 · 2.2	47.86–58.50

The cell voltage is defined as the potential difference between the two electrodes. Under standard conditions, this equilibrium potential (U_{eq}) equals 0.158 V, corresponding to the thermodynamic driving force of the SO_2-oxidation reaction.

$$U_{eq} = U_{SO_2} + U_{H_2} \qquad \text{Eq.28}$$

To maximize the energy efficiency of the SDE, the operating cell voltage should be maintained as close as possible to the reversible cell potential. This reversible potential is not fixed; rather, it varies with the actual operating conditions of the electrolyzer. Temperature, sulfuric acid concentration, SO_2 activity, water activity, and hydrogen pressure all influence the equilibrium potentials of the anodic SO_2 oxidation reaction and the cathodic hydrogen evolution reaction. At equilibrium, these electrode potentials are described by their respective Nernst equations:

$$U_{SO_2} = U^0_{SO_2,T} - \frac{RT}{nF} \ln Q_T \qquad \text{Eq.29}$$

$$U_{H_2} = U^0_{H_2,T} + \frac{RT}{nF} \ln \frac{P_{H_2}}{P^0_{H_2}} \qquad \text{Eq.30}$$

Where:

- U_{SO_2}; U_{H_2}: electrode potentials (V)
- $U^0_{SO_2,T}$; $U^0_{H_2,T}$: standard electrode potentials at temperature T (C).
- R: Universal gas constant (8.314 J/molK)
- T: Absolute temperature (K).
- n: Number of electrons transferred in the half-reaction [-] here n=2.
- F: Faraday constant, 96485 C/mol
- Q_T: Reaction quotient for SO_2 oxidation [-]

$$Q_T = \frac{\left(a_{\mathrm{SO_2}}\right)\cdot\left(a_{\mathrm{H_2O}}\right)^2}{\left(a_{\mathrm{SO_4^{2-}}}\right)\cdot\left(a_{\mathrm{H_2}}\right)\cdot 10^{-2\mathrm{pH}}}) \quad \text{Eq.31}$$

- P_{H_2}: Hydrogen partial pressure at cathode (Pa or bar, consistent units).
- $P^0_{H_2}$: Standard-state hydrogen pressure, usually 1 bar (Pa or bar).

Any voltage applied beyond this adjusted equilibrium potential represents an overpotential, which accounts for losses related to reaction kinetics, ohmic resistance, and mass transfer limitations. These overpotentials directly lower the system's electrical efficiency because the excess energy input is dissipated as waste heat instead of being converted into useful chemical energy in the form of hydrogen.

Systematic studies have been conducted to decompose the total SDE voltage into its constituent parts: reversible potential, anodic overpotential, cathodic overpotential, and ohmic loss. [90], [91], [92]

$$V_{cell} = U_{eq} + \eta_a + \eta_c + \eta_\Omega \quad \text{Eq.32}$$

Where:

- U_{eq} = equilibrium potential
- η_a = anodic overpotential
- η_c = cathodic overpotential
- η_Ω = ohmic overpotential

The electrode overpotentials can be further partitioned into kinetic overpotentials and concentration overpotentials. Kinetic overpotential (also known as activation overpotential or charge transfer resistance) arises from the finite rate of electrochemical reactions and their inability to reach equilibrium instantly. In the context of the SDE, this represents the extra voltage required to drive the sluggish SO_2 oxidation at a practical rate. Concentration overpotential (or diffusion resistance) is the additional voltage that arises when the supply of reactants, such as dissolved SO or water, to the catalyst sites

is insufficient. This creates a concentration gradient between the bulk electrolyte and the electrodes surface, particularly at high current densities. Finally, the ohmic term entails voltage losses caused by the inherent resistance of the cell components, including the flow fields, GDLs, catalyst layers, and the membrane. These ohmic losses generally increase linearly with current density.

To accurately assess and investigate U_{eq} the activities of the reacting chemical species are required according to Eq.22. To achieve this, Straser et al. at the USC [93] and Gorensek et al. at the SRNL [92] developed thermodynamic and mathematical models. These models integrated specialized methods, such as Mixed Solvent Electrolyte (MSE) or electrolyte NRTL (eNRTL), to simulate activities within the highly non-idea SO_2-H_2SO_4-H_2O system. They showed that the reversible cell potential increases with both the temperature (dE^o/dT = 0.784 mV/K) and the product sulfuric acid concentration.

To isolate individual overpotentials researchers employed a strategy where they measured the total cell voltage (usually recorded across various temperature and pressure ranges) and subtracted U_{eq} and the ohmic losses (η_Ω), measured experimentally. Researchers at USC primarily employed the current interrupt technique and hydrogen pump experiments to isolate membrane and catalyst layer resistances.[41], [91] In contrast, groups at SRNL relied on high-frequency resistance (HFR) measurements, typically captured using galvanostatic electrochemical impedance spectroscopy (EIS).[82] Throughout these evaluations, the cathodic overpotential (η_c) for hydrogen evolution on platinum was deemed negligible, often contributing less than 5 mV to the total voltage. This approach isolated the anodic overpotential as the primary kinetic barrier and allows for the investigation how individual components shift with varying parameters.

Researchers at INET developed an in-situ EIS method to systematically analyze the components of the overall cell impedance. To characterize the electrolyzers dynamic behavior, they proposed equivalent circuit models that include elements such as ohmic resistance, anodic and cathodic kinetics impedance, and concentration polarization impedance**.** Their conclusions aligned well qualitatively with the work of the USC and SRNL groups. [94]

The following sections summarize the primary findings and experimental observations reported across several studies reviewed as part of this thesis. [41], [62], [81], [90], [91], [92], [93], [95]

Temperature

The reversible potential of SO_2-oxidation has a positive temperature coefficient of 0.784 mV/K, causing U_{eq} to rise alongside operating temperatures. Furthermore, increasing temperature decreases the solubility of SO_2 in aqueous sulfuric acid, reducing reactant availability and potentially leading mass transport limitations. For example, at 4 bar in 40

wt% H_2SO_4, the predicted SO_2 solubility decreased from 21.1 to 2.59 g SO_2 per 100 g of solution as the temperature increased from 40 to 100 °C.

However, elevated temperatures improve proton conductivity in the membrane and electrode kinetics, lowering both ohmic losses and the anodic overpotential. Because the reduction in overpotentials typically outweighs the increase in reversible potential, higher temperatures lead to a net decrease in operating cell voltage. Since Nafion requires sufficient hydration, it is generally restricted to temperatures below 100 °C, most studies being conducted near 80 °C, to prevent membrane dehydration. Therefore, higher temperatures, typically 120–140 °C, are only viable when using alternative membranes such as s-PBI or SDAPP.

Pressure

At the anode, elevated pressure increases SO_2 solubility of in the sulfuric acid, increasing its chemical activity. Thermodynamic calculations for 40 wt% H_2SO_4 at 80 °C predict an SO_2 solubility of approximately 0.75 g SO_2 per 100 g solution at 1 bar. Increasing the system pressure to 4 bar raises the solubility to approximately 4 g SO_2 per 100 g solution, while at 12 bar it reaches about 20 g SO_2 per 100 g solution. Thus, higher anode pressure can substantially improve SO_2 availability, although such high pressures exceed the conditions typically applied in SDE studies which mostly operated at atmospheric pressure.

Furthermore, maintaining pressure differential across the membrane helps controlling water transport via hydraulic permeation. Increased water flux ensures proper membrane hydration, which reduces ohmic losses and helps mitigating SO_2 crossover. At the same time, it also dilutes the sulfuric acid produced. In a study done by Garrick et al. [41] the anode was maintained near atmospheric pressure while the cathode was pressurized to about 7 bar, corresponding to a pressure differential of 600 kPa. At 80 °C and 0.5 A/cm^2, increasing the pressure differential from 0 to 600 kPa lowered the cell voltage from 0.90 to 0.72 V, but decreased the produced acid concentration from 7.0 to 4.5 M due to the additional water transported to the anode. On the cathode side, higher hydrogen pressure also shifts the equilibrium potential of the HER upward according to the Nernst equation and therefore increases U_{eq}.

Sulfuric acid-concentration

In gas-fed cells, the final acid concentration is determined by the balance between the rate of formation and the flux of water across the membrane. The production rate of pure sulfuric acid is governed by Faraday's law and scales directly with the applied current density. The diluting water flux depends on inherent membrane properties, including the polymer type and thickness. This transport is further governed by operating conditions such as temperature and pressure differences. Product concentrations above 60 wt% H_2SO_4 are desirable, but gas-fed studies typically reported around 25–45 wt% H_2SO_4.

What makes reaching high acid concentrations difficult is that it increases U_{eq} by altering the chemical activities of the reacting species. Reduces SO_2 solubility. Hinders the mobility of species due to the increased viscosity of concentrated sulfuric acid. Elevated acid concentrations also dehydrate membranes such as Nafion, which significantly decrease ionic conductivity and results in higher ohmic losses. For example, values of about 45 wt% with SDAPP, 35 wt% with Nafion 212, and around 25 wt% with s-PBI were reported at approximately 0.5 A/cm^{-2}

3. Scope of this work

Since the resurgence of technology in the early 2000s, extensive research has been carried out to improve performance and understand limitations.[41], [62] Previous studies have investigated catalyst and membrane materials [61], [64], [96], effect of operating parameters[91], [93], experimented with different cell configurations, and operation modes. [83], [84], [95] Despite the progress, several questions remain unanswered. There is no clear consensus on the optimal operating conditions, the exact reaction mechanism of SO_2 oxidation is not established, SO_2 crossover remains problematic and mass transport limitations continue to hinder cell performance. [80], [82] [97]

Because the effective delivery of reactants and the removal of products are strongly affected by the gas diffusion layer (GDL), the GDL is expected to have a major impact on SDE performance. However, a systematic understanding of how GDL properties influence SDE operation has remained lacking. Therefore, this work follows an iterative approach to investigate commercially available GDLs from different manufacturers, varying in thickness, PTFE content, and the presence or absence of microporous layers (MPLs). The results of this master's thesis were subsequently published by Roessler et al. [103], which, to the authors' best knowledge, represents the first systematic comparison of GDLs for SDE applications. The author's contribution to this publication included experimental work, cell assembly, in-situ and ex-situ measurements, data evaluation, literature review, and interpretation of the results. By examining how these properties influence cell operation and performance, this study aims to address the open question of which GDL characteristics are most suitable for SDE applications.

4. Experimental

The objective of this work is to evaluate commercially available GDLs for SDE applications and to identify properties that benefit or hinder cell performance. Five GDLs are selected, to allow for the investigation of the individual influence of the modified properties. From the resulting 25 possible combinations, a subset is tested using a series of *in situ* and *ex situ* measurements to evaluate their performance.

4.1. GDL selection

The GDLs used in this work are evaluated in a single-cell configuration using an in-house built SDE cell. Ideally, each GDL would differ by only one property, allowing changes in performance to be attributed to that specific parameter. However, since this work represents a first exploratory approach toward defining design criteria for future tailored SDE-specific GDLs, commercially available alternatives from Freudenberg Performance Materials and SGL Carbon are evaluated. (TABLE 5)

TABLE 5 | *Specifications of selected GDLs from commercial providers. The values presented are the nominal properties reported by the manufacturers, SGL Carbon and Freudenberg, in their respective technical datasheets. [98], [99], [100]*

Provider	Name	Type	Thickness µm	MPL	PTFE wt.%	Air permeability cm^3 / (cm^2s)
SGL Carbon	GDL10BA	Carbon paper	400	No	5%	85
	GDL39BB	Carbon paper	315	Yes	5%	10.3
Freudenberg	E35	Carbon felt	275 @ 10bar	No	0%	-
	E35H	Carbon felt	285 @ 10bar	No	5%	-
	H24C5	Carbon felt	215 @ 10bar	Yes	0%	0.4

Cells are assembled either symmetrically, using identical GDLs on both the anode and cathode sides, or asymmetrically, using different GDLs on each side. Except for the GDL combination, all other cell components and assembly parameters remained identical throughout the experiments. Based on the selected GDLs (TABLE 5), a total of 25 symmetric and asymmetric combinations are possible. However, some combinations are not tested because they are not expected to provide additional information compared to the selected 11. (**TABLE *6***) Therefore, only this subset of combinations are tested and are discussed in this study.

TABLE 6 | *Selected anode/cathode combinations for testing. Adopted from: [101]*

Combination	Cathode	Anode
1	GDL39BB	GDL39BB
2	H24C5	H24C5
3	E35	E35
4	GDL10BA	GDL10BA
5	E35H	E35H
6	E35	GDL39BB
7	E35	H24C5
8	GDL10BA	GDL39BB
9	E35H	GDL39BB
10	GDL39BB	GDL10BA
11	E35	GDL10BA

4.2. The SDE single-Cell

The cell used in this study is an in-house built unit, assembled from commercially available fuel cell components in a sandwich configuration. From the outside to the inside, the cell consists of stainless-steel pressure plates, Teflon spacers for electrical insulation, gold-coated copper current collectors, graphite flow fields with single serpentine channel design, gas diffusion layers, FC-PO 100 Ice Cube sealing gaskets from Freudenberg SE, and the membrane electrode assembly (MEA). The serpentine channels have a width of 1 mm and a depth of 1 mm**.** The MEA have an active area of 5 cm^2 and contained a 35 µm-thick reinforced PFSA-membrane, with Pt loadings of 0.6 mg/cm^2 on the anode side and 0.4 mg/cm^2 on the cathode side. Ice Cube sealing gaskets with a thickness of 35 µm are placed on both sides of the MEA to ensure gas tightness and prevent leakage.

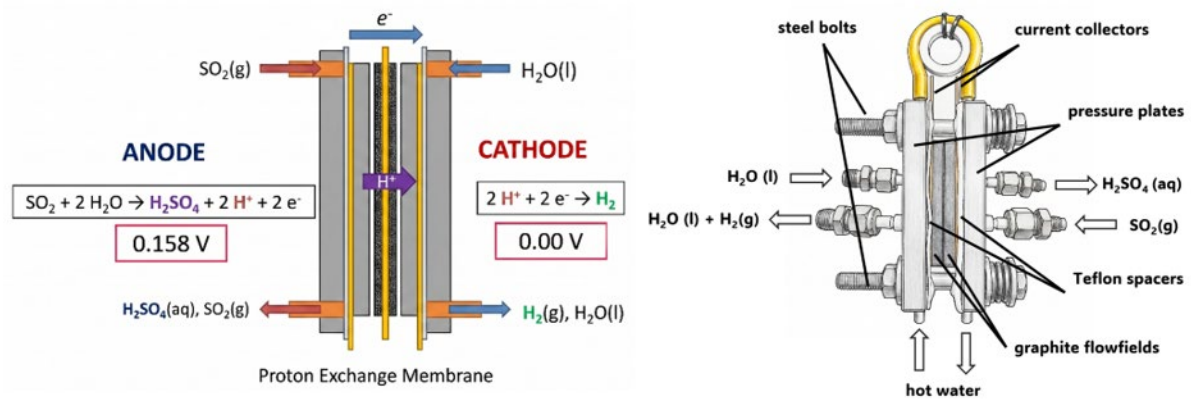

FIGURE 5 | *Schematic cross-section showing the half-cell reactions, reactants, products, and the flow of electrons (e^-) and protons H^+, alongside a 3D top view of the assembled cell hardware (right). The 3D render was generated using Google's Gemini 1.5 Pro model.*

The assembly is enclosed between the stainless-steel pressure plates and fastened using four M8 × 90 mm steel bolts and washers. Metallic disc spacers are placed at each corner to control the applied compression. The bolts are tightened in a diagonal sequence to a torque of 3.6–4.0 Nm using a calibrated torque wrench, ensuring homogeneous pressure distribution. To check the contact pressure distribution qualitatively, pressure-sensitive film is placed between the cell components during a test assembly. The resulting imprint indicates a reasonably uniform pressure distribution over the active area. The pressure film used is FUJIFILM Prescale LLW, Ultra Super Low Pressure, two-sheet type. A representative image of the pressure film and imprint is shown in Appendix D. After assembly, electrical resistance is measured using a VOLTCRAFT VC220 digital multimeter between the electrodes, between the electrodes and the respective current collectors, and between the electrodes and the pressure plates to ensure that no short circuit is present. Liquid tightness is subsequently verified by connecting the water inlet and outlet and circulating water through the cell for 5 min, the cell is considered leak-tight when no water droplets or visible leakage occurred. Gas

tightness was assessed by pressurizing the cell with nitrogen and applying leak-detection spray (Air Liquide) to the accessible fittings and sealing interfaces.

4.3. Experimental setup

The anode is supplied with 99.99% pure anhydrous SO_2 (Linde Gas GmbH, Austria) using a thermal mass flow controller (EL-FLOW Select, Bronkhorst High-Tech B.V.) operated at ambient pressure. The cathode is fed with ultrapure water (resistivity 17.6 mΩ·cm, BARNSTEAD E-PURE) delivered by a micro gear pump (ISMATEC) at a flow rate of 25 mL/min. The water is recirculated through a 500 mL reservoir located in a thermal bath at 80 °C. Fresh ultrapure water (resistivity 17.6 MΩ cm, obtained with water purifier "E-PURE", BARNSTEAD) is used for each experiment. All fluid connections consisted of PTFE tubing (6 × 4 mm) with 316 SS FITOK fit-by-torque fittings. All electrochemical measurements are carried out using a ZenniumPro potentiostat equipped with a PP242 Booster unit (ZAHNER-elektrik GmbH). The system is operated and monitored using Thales and Thales Analysis software.

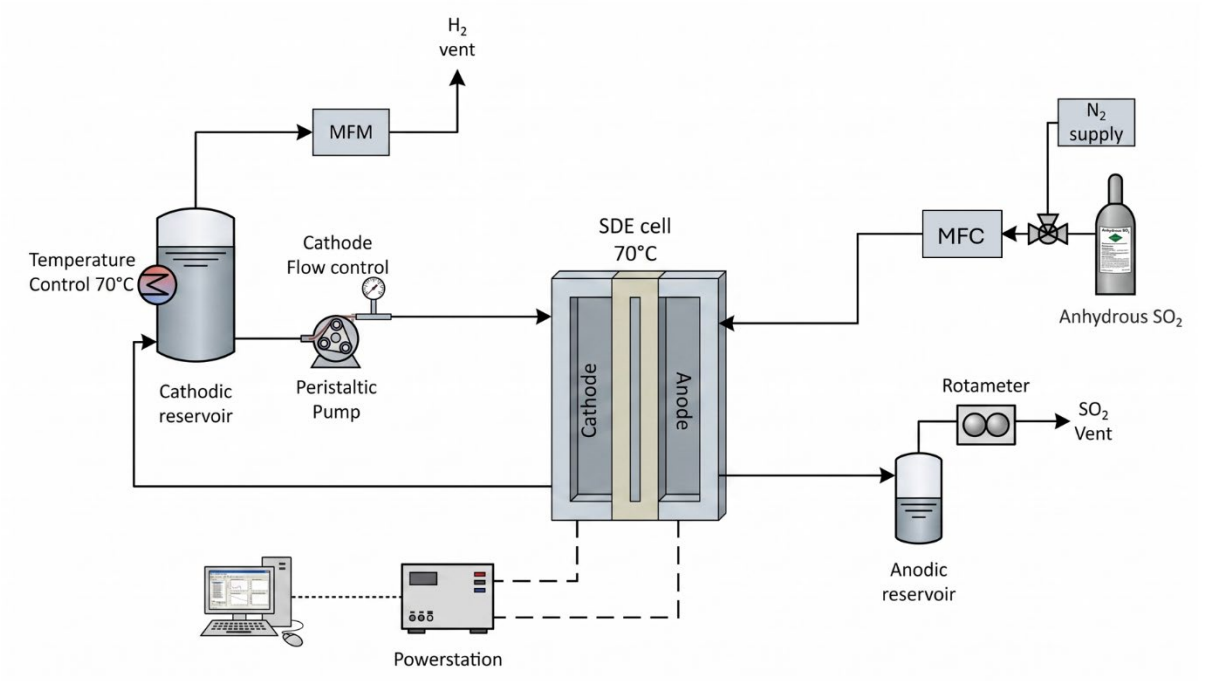

***FIGURE 6** | Schematic representation of the gas-fed SDE test station.*

4.4. Operation

4.4.1. Start-up

The operation of the SDE cell followed a defined start-up sequence to avoid SO_2 crossover and the resulting degradation. The underlying reasons for this specific start-up strategy to mitigate crossover are discussed in detail in previous work [80].

The cell is operated in potentiostatic mode, and SO_2 was only fed to the anode after a voltage had been established. As feeding SO_2 without an applied voltage can induce immediate crossover due to the rapid dissolution and diffusion of SO_2 in the acidic membrane environment.

First the cathode side is supplied with ultrapure water (80 °C) and circulated for at least 1 h prior to ensure complete humidification of the GDL and the membrane. Approximately 15 min before operation, the anode side was flushed with nitrogen to remove any residual oxygen that remained in the cell. The potentiostat is then set to operate in potentiostatic mode at a voltage of 1.2 V. After achieving a stable and low current response (<100 mA), the SO_2 feed to the anode is initiated.

4.4.2. Boundary test

To assess the operational limits of the SDE and identify stable working points, a boundary testing procedure is arried out by progressively increasing the SO_2 feed rate at the anode. The test always begins at a flow rate of 6 Nml/min, followed by 10 Nml/min, and subsequently increased in 2 Nml/min increments in each step. Each operating point is maintained until a stable current response is achieved before proceeding to the next step. A working point is considered stable when, after the initial current increase, no observable current decrease is detected over a period of at least 10 min. The SO_2 feed rate is increased until a further increase in flow produces no measurable rise in current. This point is defined as the upper operational boundary of the cell.

4.4.3. Stability test

Following the determination of this boundary, the system is shut down, and a new cell assembled with a fresh CCM and GDLs. The new cell is subjected to the start-up procedure described in Section 3.4.1. Subsequently, the SO_2 feed rate is increased stepwise, following the procedure described for the boundary test, until the previously identified last stable operating point is reached. Stability testing is performed over a period of 4 h to assess potential degradation rates and confirm the reproducibility of the optimized operation regime. The anodic effluent is directed into a liquid trap to collect the reaction products, while excess gas is vented. The process operates in a single-pass configuration, meaning no recirculation of the anodic liquid takes place.

4.4.4. In-situ characterization

Both used characterization techniques, electrochemical impedance spectroscopy (EIS) and potentiodynamic polarization curves, are well established and generally regarded as non-intrusive in conventional systems such as PEMWE and PEMFC, they can be used without significantly disturbing the operating conditions or damaging cell components. However, due to the intrinsic operating conditions of SDE both, their applicability and the obtainable information is limited. During polarization measurement while the potential is relatively low the cell is operating with excess SO_2 feed, this results in crossover and

drying of the membrane and anode side GDL. The excess SO_2 also causes a slight overshoot in the measured current once higher potentials (1–1.2 V) are reached. During normal operation the system is ideally close to 100% SO_2 conversion. Therefore, when registering an impedance spectrum, signals arising from mass-transport limitations can overshadow the contributions of other processes. To prevent this, EIS measurements can be performed under excess SO_2 feed, but that leads to the previously mentioned problems. Consequently, neither EIS measurements nor polarization curves can be regarded as fully non-intrusive in SDE, and neither technique is fully suitable for describing stable operating conditions.

EIS is carried out in single-sine mode using a frequency sweep from 100 mHz to 100 kHz, starting at 1 kHz and proceeding bidirectionally across the selected range with a 10 % amplitude (0.12 V).

Potentiodynamic polarization curves are registered with a scanning rate of 0.01 V/s with a potential range of 0.5 – 1.3 V. This interval ensures that only the intended electrochemical processes are investigated. Potential lower than 0.5 V would lead to the reduction of SO_2 at the anode, while potential higher than 1.3 V could cause the oxidation of water.

4.6. Ex-situ characterization

4.6.1. Scanning electron microscopy

Scanning electron microscopy (SEM) and energy-dispersive X-ray spectroscopy (EDX) are employed to qualitatively assess changes in the morphology and surface composition of the GDLs before and after operation. For SEM analysis, GDL samples with a maximum size of approximately 5 × 5 mm are prepared by cutting the material with a scalpel, without prior freezing. The samples are mounted on aluminium stubs using conductive carbon adhesive tape. For surface imaging, the samples are placed flat on the sample holder. For cross-sectional imaging, the samples are mounted perpendicular to the holder, so that the cut edge of the GDL is exposed to the electron beam. Imaging is performed using an FEI XL20 microscope (Philips, Amsterdam) operated at 15 kV. EDX is used to screen for possible surface contamination, particularly sulfur-containing deposits.

4.6.2. Mercury intrusion porosimetry

MIP is performed on each GDL using automated porosimeters from the Pascal series (Pascal 140 and Pascal 440, Thermo Finnigan) over a pressure range of 0.01–400 MPa to determine porosity and mean pore diameter. Data evaluation is carried out using the instrument's software, applying a lower pressure limit of 0.01 MPa and using the default mercury parameters (surface tension 0.485 N/m, contact angle 140°, and mercury density 13.5463 g/cm^3) for pore-size calculations.

During MIP, the sample is immersed in mercury, and the intruded pore volume is recorded as a function of increasing pressure. In theory by using the Washburn equation, the pore diameter corresponding to each intrusion pressure can be calculated, and by differentiating the intrusion curve, the pore size distribution can be derived. In practice, these calculations are carried out automatically by the instrument software, Solid, product version 1.4.1.3, file version 1.6.3.2.

$$d = -\frac{4\gamma \cos(\phi)}{P} \quad \text{Eq.33}$$

- d: pore diameter [m]
- γ: mercury surface tension [N/m]
- ϕ: mercury contact angle [°]
- P: applied intrusion pressure [Pa]

It is important to note that MIP is limited to pores that mercury can penetrate within the applied pressure range. Therefore, pores below approximately 0.1 μm cannot be reliably resolved using this method.

4.6.3. Contact angle measurement

Contact angle measurements are conducted to assess the wettability of the GDLs. A static contact angle is recorded using an Ossila L2004A1 goniometer (Ossila BV). All measurements are performed under ambient laboratory conditions. Ultrapure water droplets are placed on the GDL surface at three locations. The reported values, in TABLE 7, are the average contact angles calculated by instrument software.

4.6.4. Product characterization

Acid produced during the stability testing is analyzed with acid–base titration using an automated titration system (Titroline 7800, SI Analytics). For each measurement, 0.25 ± 0.001 mL of the anodic product is transferred into a 100 mL beaker, diluted with ultrapure water, and titrated with a 1.000 ± 0.001 M KOH solution (Carl Roth GmbH). Each sample is titrated thrice, and the reported value corresponds to the average of the three measurements. By determining the w/w% of H_2SO_4 the Faradaic (current) efficiency is calculated. This allowed the verification that the measured current wasn't the result of undesired side reaction.

5. Results and Discussion

5.1. Ex-situ characterization

The ex-situ measurements support and complement the information disclosed by the manufacturers. These measurements provide insights that enable a more detailed

characterization of the GDL microstructure, which helps to explain the behaviour observed during in-situ testing.

5.1.1 Scanning electron microscopy

All anode-side GDL materials used in this study are examined with SEM by comparing pristine samples with used samples of the same material. For GDLs containing an MPL, both the MPL side and the fiber side are examined. The complete set of SEM micrographs is provided in Appendix A. From these micrographs, a selected subset is presented below to highlight the key differences and support the observations discussed in this section. The selected micrographs highlight the main morphological differences between the carbon-paper GDLs, represented by the Sigracet materials (GDL39BB and GDL10BA), and the carbon-felt GDLs, represented by the Freudenberg materials (E35, E35H, and H24C5).

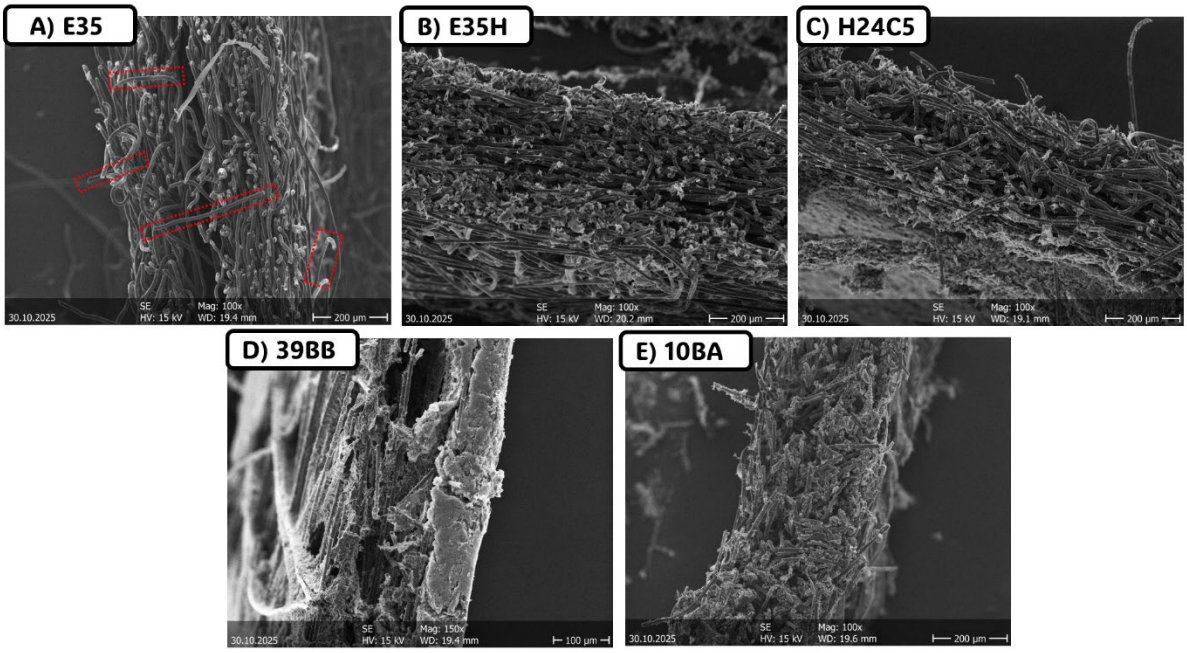

FIGURE 8 | *SEM cross-sectional images of the pristine GDLs used in this study. The micrographs display the internal fibrous structure of the Freudenberg (E35, E35H, H24C5) and SGL Carbon (39BB, 10BA) samples, captured at a magnification 100 x (with the exception of 39BB at 150x).*

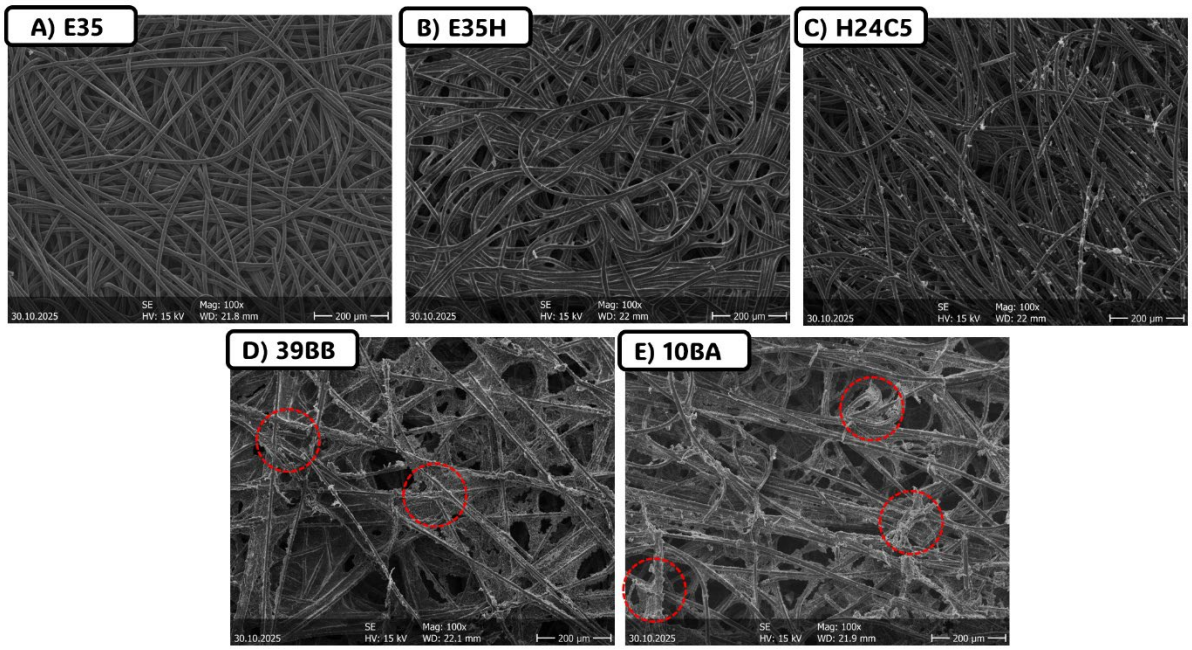

FIGURE 7 | *SEM images of the substrates of the investigated pristine GDLs. The micrographs show the top-view fibrous network of the Freudenberg (E35, E35H, H24C5) and SGL Carbon (39BB, 10BA) substrates, captured at a magnification of 100x*

The observed structures are consistent with the expected morphology of these two GDL classes. Although both are non-woven carbon materials, the surface (FIGURE 8) and cross-sectional images (FIGURE *7*) reveal clear structural differences. The Sigracet GDLs consist of shorter, straight fibers (FIGURE 7/E) that are randomly distributed but mainly oriented within the plane of the GDL. In comparison, the Freudenberg GDLs are composed of longer fibers (FIGURE 8/A, B, C) that twist and curve, forming a felt- or "spaghetti-like"

structure. The cross-sectional image of E35 (FIGURE 7/A) also shows fibers oriented in the through-plane. A few such fiber were marked with red rectangles. This feature can affect cell assembly, as sharp fibers perpendicular to the PEM may penetrate the membrane and cause short circuits. Although the penetration of the membrane was not directly confirmed, it provides a plausible explanation for the frequent short circuits observed during the assembly of combinations containing E35 or E35H. In these cases, either the start-up current remained above 100 mA, or the electrical resistance was close to zero when measured between the electrodes using a multimeter. The micrographs (FIGURE *8*) also confirm surface treatment. No additional binder or coating is visible on H24C5 and E35, consistent with their untreated surface. In contrast, E35H, GDL39BB, and GDL10BA show clearly visible additional binder material on the carbon fibers. This is further corroborated by the EDX results (Appendix C), which show elevated fluorine levels of 9.72 wt.%, 25.75 wt.%, and 25.72 wt.% for E35H, GDL39BB, and GDL10BA, respectively, compared to lower levels of 2.41 wt.% and 1.7 wt.% for H24C5 and E35, respectively. However, the appearance of the coating differs between the materials. In E35H, the fibers appear more evenly coated, suggesting a relatively homogeneous distribution. For the Sigracet GDLs, the binder appears coarser and more localized (FIGURE 8/D, E), with visible aggregation mainly at fiber contact points and junctions. These differences can be attributed to differences in the manufacturing process as described in ref. [46]

The SEM images already allow qualitative observations regarding fiber density and pore structure. The Sigracet GDLs consist of more loosely packed fibers and display noticeably larger pores in both the surface and cross-sectional views. In contrast, the Freudenberg GDLs exhibit a higher fiber density, with only comparatively small pores visible in the SEM images.

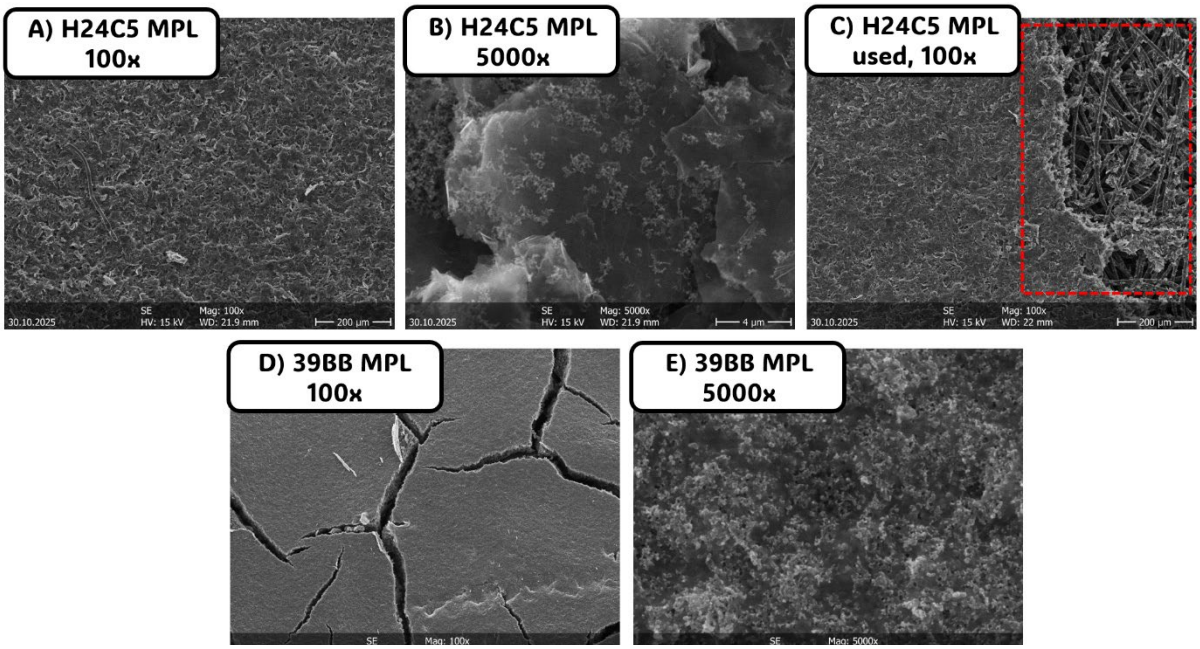

FIGURE 9 | *SEM images of the MPLs. The micrographs show the pristine MPL surfaces of the H24C5 and 39BB gas diffusion layers at magnifications of 100x and 5000x, alongside a degraded H24C5 sample after operation (highlighted with a red border).*

Differences can also be observed in the MPL morphology. (FIGURE 9). The MPL deposited on GDL39BB appears comparatively thicker and contains visible surface cracks. At higher magnification (×5000), small pores can also be identified within the MPL structure. In contrast, the MPL on H24C5 appears thinner and more compact, with no visible surface cracking. These observations help explain the substantially lower permeability reported for H24C5. Conversely, the higher permeability of GDL39BB is likely related to the presence of cracks and small pores in the MPL, which provide additional pathways for gas and liquid transport.

A comparison of the SEM images of the used and pristine GDLs, provided in Appendix A, shows little to no visible differences, indicating that no measurable degradation occurred within the investigated time frame. One exception is the MPL of H24C5, which is partially delaminated (FIGURE 9/C) during cell disassembly, with a clear rupture visible within the MPL layer. This is not the only indication of lower structural cohesion in the Freudenberg GDLs. E35 also tended to be separated into two distinct layers. Although this separation was not consistently visible in all cross-sectional images of the Freudenberg materials, it was repeatedly observed during handling.

5.1.2. Contact angle and Porosimetry

The hydrophobic properties of GDL materials are controlled by surface and bulk treatments. PTFE treatment increases the hydrophobicity of the fibrous substrate, while the presence of an MPL modifies the surface. Since wettability influences water distribution within the GDL, contact angle measurements are used to assess the interaction between the GDL surface and liquid water.

TABLE 7 | *Contact angle measurements of the investigated GDL substrates and MPLs. The reported values represent experimental data gathered to evaluate surface wettability properties.*

Name	Type	Face analysed	PTFE	Contact angle
GDL10BA	Carbon paper	Fibers	5%	143.4 ± 6.4
GDL39BB	Carbon paper	MPL	5%	157.7 ± 3.0
		Fibers	5%	148.0 ± 1.1
H24C5	Carbon felt	MPL	0%	150.3 ± 5.9
		Fibers	0%	132.6 ± 3.7
E35	Carbon felt	Fibers	0%	120.7 ± 8.2
E35H	Carbon felt	Fibers	5%	133.1 ± 6.4

In general, all investigated GDL substrates exhibit hydrophobic behavior with contact angles between 120.7 ± 8.2° for E35 and 148.0 ± 1.1° for GDL39BB. The measured values are consistent with literature, where contact angles of untreated carbon-paper GDLs are commonly reported between approximately 105° and 135°, while PTFE-treated materials can reach values above 150°. [102] The Freudenberg substrates show similar contact angles with overlapping uncertainties, indicating no statistically significant difference between them. E35 displayes the lowest mean contact angle, which is consistent with the absence of surface treatment. In contrast, E35H and H24C5 exhibit slightly higher and very similar mean contact angles values of 132.6 ± 3.7° and 133.1 ± 6.4°, respectively, despite PTFE treatment being specified only for E35H. This indicates that the measured value is influenced not only by PTFE treatment, but also by fiber arrangement, surface topography, and roughness. The MPL surfaces of GDL39BB and H24C5 show comparable contact angles above 150°, exceeding those of their respective fiber substrates. This increase is likely related to the higher PTFE content of the MPLs, however, MPL deposition also modifies the surface morphology, including roughness, porosity, and topography, which additionally influences the measured contact angle. Therefore, the higher values cannot be attributed to PTFE content alone.[44]

Although the exact PTFE contents are not disclosed by the manufacturers. Assumptions can be made based on the fluorine content detected by EDX. For the fiber substrates, the fluorine levels are measured at 1.7 *wt%* for E35, 2.41 *wt%* for H24C5, 9.72 *wt%* for E35H, 25.72 *wt%* for GDL10BA, and 25.75 *wt%* for GDL39BB. These low baseline values for E35 and H24C5 confirm earlier statements that these specific substrates do not have a hydrophobic coating.

In contrast, the microporous layers (MPLs) show an increase in fluorine. The GDL39BB MPL exhibits a notably high fluorine content of 52.27 wt.%, which assumingly points to extensive PTFE usage in its composition. While the H24C5 MPL has a relatively lower fluorine content of 19.78 wt.%, this is still roughly ten times higher than the amount found in its corresponding untreated substrate.

TABLE 8 | *MIP results for the investigated GDL substrates. The reported values characterize the specific pore volume, pore surface area, and modal pore diameter to evaluate the internal porous structure of the materials.*

Name	Type	Specific Pore volume mm^3/g	Pore surface area m^2/g	Modal pore diameter µm
GDL10BA	Carbon paper	2973±7.4	37.9±0.9	67.15±0.2
GDL39BB	Carbon paper	2139 ±5.3	36.9±0.9	71.07±0.2
H24C5	Carbon felt	1550±3.9	22.2±0.6	21.97±0.1
E35	Carbon felt	1415±3.5	10.6±0.3	23.57±0.1
E35H	Carbon felt	1259±3.1	20.1±0.5	21.66±0.1

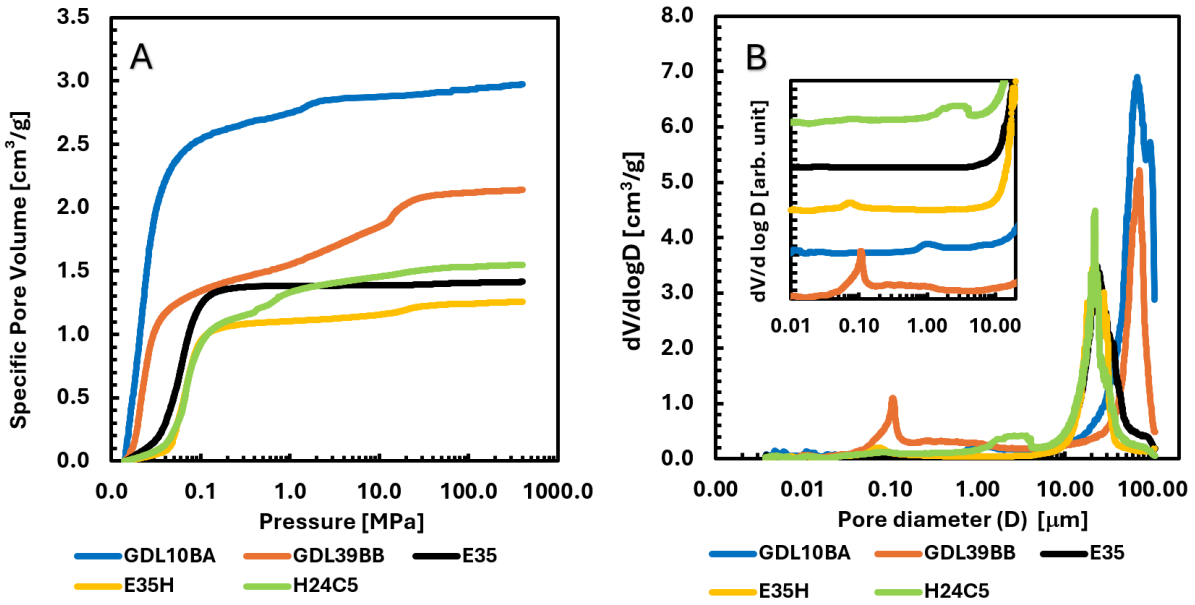

FIGURE 10 | *MIP analysis for the investigated GDLs.* ***A)*** *Cumulative specific pore volume as a function of intrusion pressure.* ***B)*** *Log-differential pore size distribution (dV/dlogD) indicating the modal pore diameters of the carbon paper (GDL10BA, GDL39BB) and carbon felt (E35, E35H, H24C5) materials, with an inset highlighting the sub-micron pore variations.*

Through MIP, various structural properties of the GDL materials are investigated. The corresponding results are summarized in TABLE 8

.

All GDLs exhibit a broad pore size distribution, ranging from pore diameters below 0.1 µm up to 100 µm, with most pores located in the 10–100 µm range. (FIGURE 10) These results are consistent with the SEM observations and confirm that the Sigracet GDLs possess larger and more easily accessible pores. This is reflected by their modal pore diameters of 67.15 µm for GDL10BA and 71.07 µm for GDL39BB. In comparison, the Freudenberg materials exhibited considerably smaller modal pore diameters of 21.97 µm for H24C5, 23.57 µm for E35, and 21.66 µm for E35H.

GDL39BB additionally shows a bimodal pore size distribution due to the presence of the MPL. The MPL introduces a second pore population, approximately two orders of magnitude smaller than those of the substrate. In contrast, no comparable peak was observed for H24C5, indicating that mercury could not penetrate the pores of its MPL within the applied pressure range. This is consistent with the compact MPL morphology observed by SEM and helps explain the very low permeability of H24C5.

E35, which is not subjected to surface treatment and therefore contains no additives, shows no indication of pores smaller than approximately 8–10 µm. This is reflected by the essentially flat intrusion curve from about 0.2 MPa onwards and by its low pore surface area of 8.82 m^2/g. In comparison, E35H should differ from E35 only by the applied hydrophobic treatment, according to the manufacturer. This treatment appears to reduce the total pore volume while introducing a population of smaller pores. This would explain the slight increase in the intrusion curve in the high-pressure region and the sharp increase in pore surface area to 16.71 m^2/g, roughly twice that of untreated E35.

Overall, the porosimetry results support the trends observed during in situ testing. The carbon-paper GDLs, GDL39BB and GDL10BA exhibited roughly twice the pore volume of E35, E35H, and H24C5 and showed the largest average pore diameters. Their higher porosity, and therefore larger void fraction within the diffusion medium, likely improves their ability to sustain the flooded acidic environment proposed in this work, while still allowing efficient transport of H_2SO_4 into and out of the anode compartment.

5.2. In-situ testing

For better readability, the GDL combinations are denoted by their respective numbers in TABLE 6, followed by the corresponding [cathode GDL] / [anode GDL] arrangement in parentheses. For symmetrical configurations, only the GDL type is indicated in parentheses.

5.2.1. Symmetrical gas diffusion layer configurations

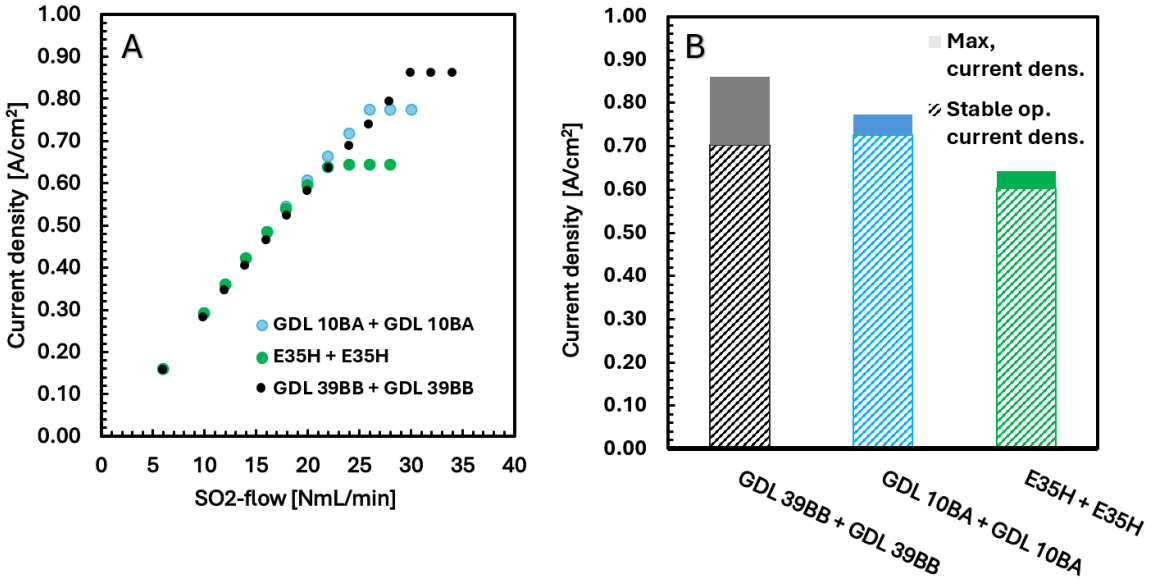

FIGURE 11 | *Symmetric GDL experimental run.* ***A)*** *boundary-test results, depicting the highest current density obtained with each configuration;* ***B)*** *comparison of the stable operating current density with the corresponding maximum current density achieved during boundary testing*

Five symmetric combinations are evaluated. Of these, three configurations, namely combination 1 (GDL39BB), combination 4 (GDL10BA), and combination 5 (E35H), achieve stable operation (FIGURE 11). In contrast, combination 2 (H24C5) and combination 3 (E35) do not perform successfully, as their cell performance do not exceed 100 mA/cm^2. These configurations are therefore excluded from further comparison, and only their respective polarization curves are shown in FIGURE 11/A. GDL39BB reaches the highest current density during boundary testing; however, this does not translate into superior stable performance. Under steady operation, both Sigracet GDLs, GDL39BB and GDL10BA perform similarly, whereas E35H shows slightly lower performance.

These results show that the use of hydrophobically treated carbon paper on both sides, either with or without an MPL, enables stable operation with reasonable performance. On the other hand, the absence of hydrophobic treatment appears to prevent successful operation, as the GDLs used in the failed configurations, H24C5 and E35, are both untreated. This is most clearly supported by comparing combination 3 (E35) with combination 5 (E35H), where the GDLs differ only in surface treatment: E35H is hydrophobically treated, whereas E35 is not.

Furthermore, the results indicate that the MPL also affects GDL performance, most likely through its influence on permeability. Both H24C5 and GDL39BB contain an MPL, yet GDL39BB enables stable operation, whereas H24C5 did not. We propose that this difference is not only related to the absence of PTFE treatment in H24C5, but also to its drastically lower permeability of 0.4 cm^3/cm^{2}s compared to 10.3 cm^3/cm^{2}s for GDL39BB.The role of the MPL is further highlighted when considering GDL10BA, which

has no MPL and exhibits an approximately eightfold higher permeability of 85 cm^3/cm^2s. However, this increased permeability does not result in improved performance compared to GDL39BB. This suggests that permeability is beneficial only up to a certain threshold, beyond which further increases do not provide additional performance gains. To elucidate these differences, ex situ measurements are performed and are discussed in section *4.6.1*.

FIGURE 12/A, B shows the impedance spectra recorded after stability testing and the polarization curves recorded after boundary testing, respectively. The polarization curves provide only qualitative information and should therefore not be interpreted as direct indicators of steady-state operation. This is because the cell, which ideally operates close to 100% SO_2 conversion, is supplied with a large excess of SO_2 during the initial low-voltage region of the polarization curve. Under these conditions, SO_2 crossover can occur almost immediately, and the measured current may be artificially increased by parasitic reactions. In addition, excess SO_2 can still be present at the electrode surface when higher voltages above 1.2 V are reached, leading to a slight current overshoot. This explains why the current densities shown at 1.2 V in FIGURE 12/A are consistently higher than those achieved during stable operation in FIGURE 11/B. Despite these limitations, polarization curves should not be disregarded, as the trends observed reflect the relative effectiveness of the different combinations and provide a meaningful basis for comparison.

Lastly, the EIS results lead to similar conclusions. A clear difference is observed between the carbon-paper GDLs, GDL39BB and GDL10BA, and the carbon-felt GDL, E35H. Both GDL39BB and GDL10BA show a distinguishable semicircle in the high-frequency region and a lower-frequency tail, indicating that the main electrochemical features remain visible. In contrast, E35H shows a sharp diffusion element that appears to overshadow the rest of the impedance response, resulting in impedance values orders of magnitude higher. This behavior suggests that transport is strongly hindered when using E35H, most likely at the anode, due to its lower porosity and less favorable pore structure for gas–liquid transport. As with the previous observations, ex situ characterization will be used to further interpret and confirm the origin of these differences.

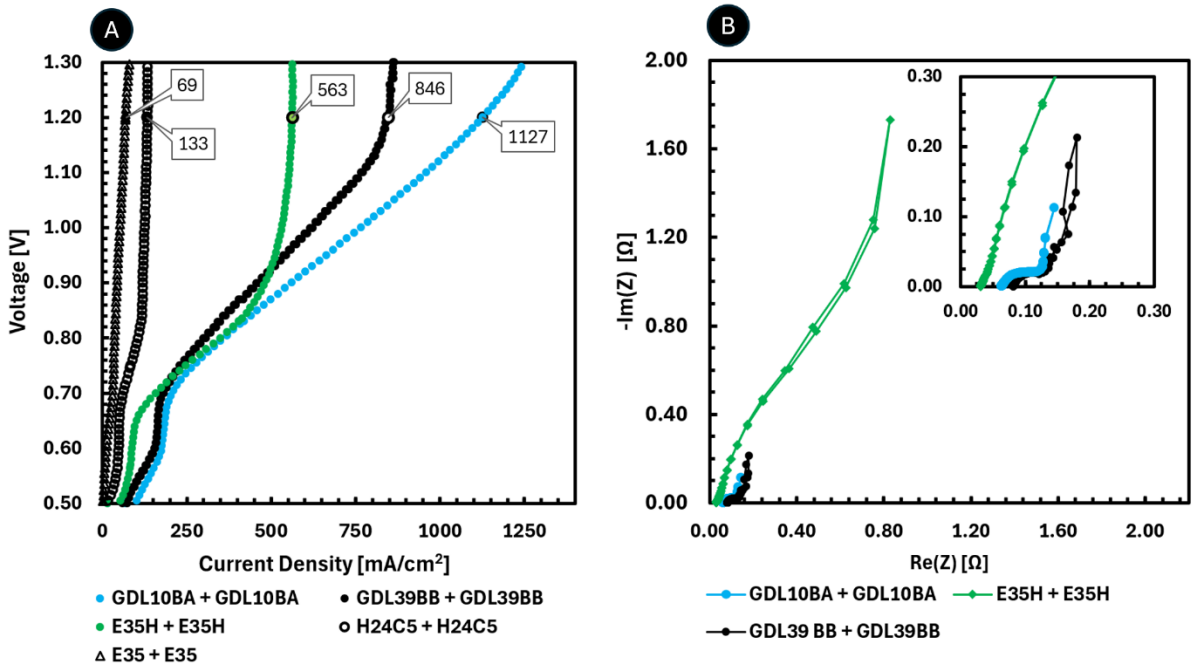

***FIGURE 12** | Electrochemical characterization of the symmetric GDL configurations. **(A)** Polarization curves recorded for all symmetric combinations. The highlighted values indicate the current densities obtained at the selected operating voltage of 1.2 V. **(B)** Nyquist plots of the symmetric configurations that achieved stable operation, measured after completion of the stability test.*

5.2.2. Asymmetrical gas diffusion layer configurations

For the asymmetric tests, six GDL pairings are selected from all possible combinations based on the performance of the symmetric configurations. Of these six combinations, five pass the boundary testing. (FIGURE *13*/A) The only configuration that does not perform successfully is combination 7 (E35/H24C5). Therefore, this combination is omitted from further comparison, and only its respective polarization curve is shown in FIGURE *14*/A to document its low performance. Ultimately, only two asymmetric configurations, namely combination 6 (E35/GDL39BB) and combination 10 (GDL39BB/GDL10BA), are able to maintain stable operation for 4 h. (FIGURE *13*)

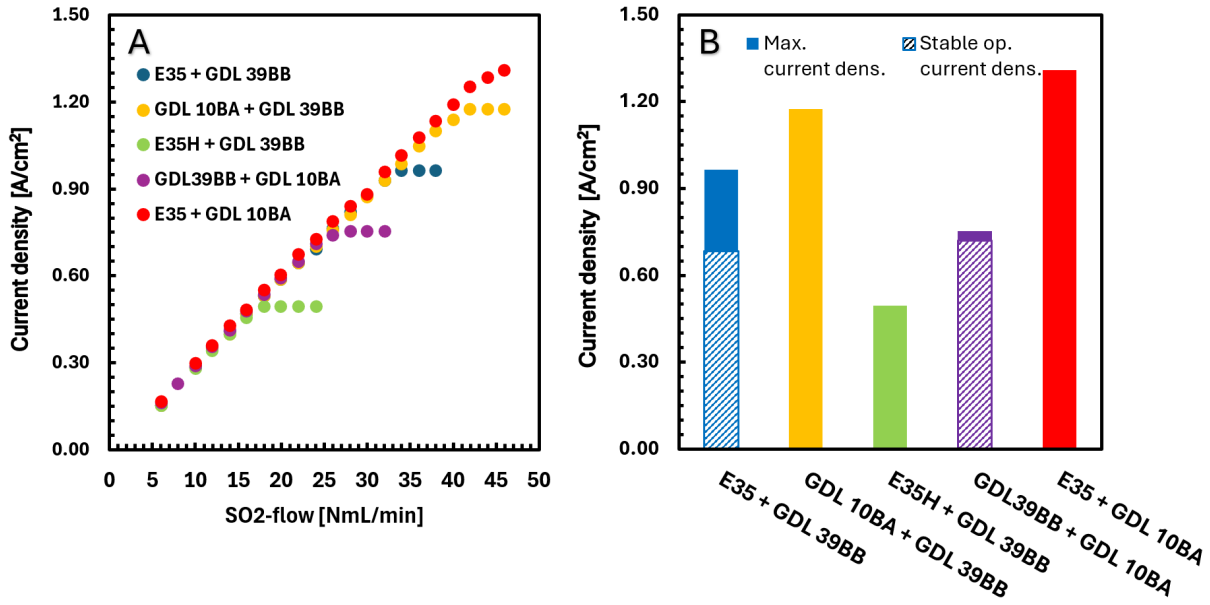

FIGURE 13 | *Asymmetrical GDL experimental run **A)** boundary-test results, depicting the highest current density obtained with each configuration; **B)** comparison of the stable operating current density with the corresponding maximum current density achieved during boundary testing*

Combinations 6 (E35/GDL39BB), 8 (GDL10BA/GDL39BB), and 11 (E35/GDL10BA) reaches higher current densities during boundary testing than any of the symmetric configurations. This is attributed to the use of either E35 or GDL10BA on the cathode side, where water retention is especially important in the gas-fed configuration. Since water is supplied from the cathode side, sufficient water inventory at the cathode is required to support effective transport toward the anode. GDL10BA, although hydrophobically treated, has the highest pore volume according to the porosimetry measurements, contains no MPL, is relatively thick, and has the highest permeability. These properties allow it to accommodate more water and make it more prone to flooding. E35, although less porous than GDL10BA, lacks PTFE treatment and is therefore relatively hydrophilic also indicated by the lower contact angle of 120.7°, which promotes water retention at the cathode.

In contrast, combinations 9 (E35H/GDL39BB) and 10 (GDL39BB/GDL10BA) show comparatively poorer performance. We propose that this is due to insufficient water availability at the cathode, although this likely arises from different material properties. In combination 9, E35H had the lowest pore volume among the tested GDLs and, due to its PTFE treatment, a higher contact angle than E35. The combination of low pore volume and increased hydrophobicity reduces water uptake and retention, thereby limiting water transport toward the membrane. In combination 10, GDL39BB is placed on the cathode side. Although its contact angle and pore volume is comparable to that of GDL10BA, it has lower porosity due to it MPL. Which, again, hinders water transport toward the membrane.

At the same time, the E35 is unsuitable as the anode-side diffusion layer under the tested conditions. The symmetric E35 combination can not operate successfully. We propose that the high water retention of E35 hinders efficient transport within the SO_2–H_2SO_4–water system, where SO_2 access and product removal are critical.

Furthermore, combination 7 (E35/H24C5) does not operate successfully. However, this failure cannot be attributed to the presence of E35 on the cathode side, since E35 performed when paired with both GDL39BB and GDL10BA. The limitation must therefore originate from H24C5 on the anode side. This confirms that H24C5 is not suitable for SDE operation and further supports that sufficient permeability and effective mass transport are the key to high performance.

Combination 11 reaches the highest current density among all tested configurations, supporting the previous observations and further highlighting that an MPL is not strictly required to achieve good SDE performance. However, the MPL proves to be beneficial from a practical assembly perspective. Combinations using GDLs without an MPL are more difficult to assemble reliably and often result in short-circuiting. This issue is especially pronounced for E35 and E35H. We propose that this is because these graphite-felt materials exhibit fibers oriented in the through-plane direction. As mentioned in section 4.6.1 these fibers possibly pierce the membrane during cell tightening.

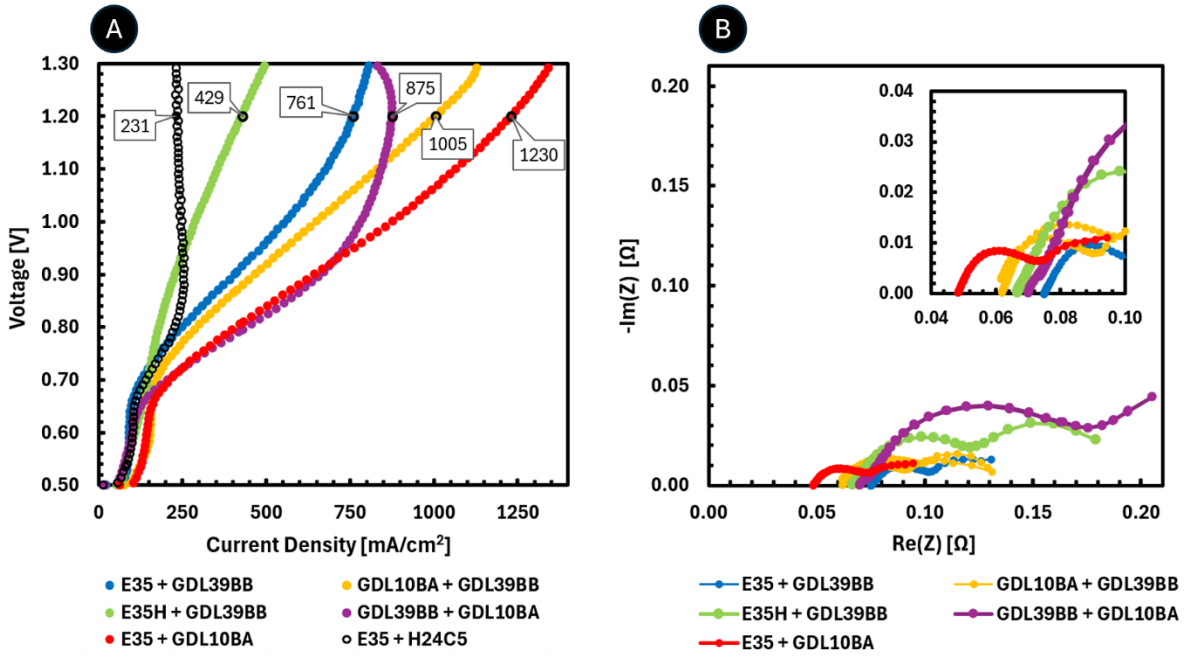

FIGURE 14 | *Electrochemical characterization of the asymmetric GDL configurations.* ***(A)*** *Polarization curves recorded for the asymmetric combinations. The highlighted values indicate the current densities obtained at the selected operating voltage of 1.2 V.* ***(B)*** *Nyquist plots of the asymmetric configurations that achieved stable operation. The combination E35 + H24C5 did not reach stable operation and is therefore not included in the impedance analysis.*

FIGURE *14*/A, B show the impedance spectra and polarization curves of the asymmetric configurations, respectively. All asymmetric combinations exhibit low overall

impedance, and two distinct semicircles were visible in the spectra. This could indicate the presence of two underlying physical or chemical processes, each occurring with its own characteristic timescale. Similar EIS features have been discussed in literature. Xue et al. [94]assigned the high-frequency intercept mainly to ohmic resistance, while the impedance arc was mainly related to the SO_2 oxidation reaction. At higher cell voltages, an additional mass-transfer contribution became visible. Ding et al. [81] later separated the impedance of SDE cells into ohmic, kinetic, and concentration-polarization contributions and showed that, at higher operating voltages, both reaction kinetics and mass transport can influence the spectra. However, these literature studies were carried out in liquid-fed SDE cells and used equivalent-circuit fitting, whereas in the present work the EIS data were recorded only as a qualitative comparison after operation. Therefore, the semicircles observed here are interpreted only as an indication of overlapping reaction and transport effects, most likely related to SO_2 oxidation and gas–liquid transport in the porous electrode. A detailed assignment of the individual arcs was not attempted.. Polarization curves show the same general performance ranking as the boundary testing/stable-operation data. Combination 11 (E35/GDL10BA) shows the highest current density, followed by combination 8 (GDL10BA/GDL39BB), while combinations 6 (E35/GDL39BB) and 10 (GDL39BB/GDL10BA) show intermediate performance. In contrast, combination 9 (E35H/GDL39BB) performs clearly worse, and combination 7 (E35/H24C5) remains the poorest configuration. This ranking is best explained by the different requirements of the cathode and anode, rather than by a single GDL property. E35 and GDL10BA perform well at the cathode because their wettability or high pore volume, respectively, support water retention and transport toward the anode. At the anode, the more open GDL10BA provides the highest performance, whereas GDL39BB remains functional due to its cracked MPL but introduces additional transport resistance. In contrast, the compact, low-permeability MPL of H24C5 severely restricts anode-side gas–liquid transport, explaining the failure of combination 7.

5.3. Product characterisation: Titration

Analysis of the anode outlet, specifically the amount and acid concentration, enables the calculation of current efficiency and provides insight into water availability inside the cell. FIGURE 15 shows the acid production rate, total liquid production rate, acid concentration, and current efficiency for the five combinations that went through stability testing. In all cases, the current efficiency was close to 100%, indicating that parasitic reactions were negligible (FIGURE 15). The acid production rate alone is not characteristic of a given GDL combination, because it is coupled to the reaction rate through Faraday's law. Therefore, different cells operating at similar current densities produce the same amount of pure acid, independent of the GDL combination.

More informative conclusions can be drawn from the liquid-production rate and acid concentration, as these values provide an indication of water availability in the anode

compartment. This is critical because water plays a central role in successful SDE operation and affects performance through several coupled transport processes. Combination 4 (GDL10BA) shows the lowest acid concentration, 28.4 wt.%, and the highest water throughput, which is consistent with the high permeability of GDL10BA. Comparing combination 4 (GDL10BA) with combination 10 (GDL39BB/GDL10BA), which produced acid concentrations of 28.4 wt.% and 49.5 wt.%, respectively, provides further insight. In both cases, GDL10BA is used on the anode side, while the cathode-side GDL is changed from GDL10BA to GDL39BB. Since GDL39BB contains an MPL and exhibits lower permeability, the higher acid concentration obtained for combination 10 suggests reduced water transport from the cathode to the anode. This indicates that water availability at the anode is governed more strongly by the cathode-side conditions.

This conclusion is further supported by combination 5 (E35H) and combination 6 (E35/GDL39BB). Both show slightly higher acid concentrations than combination 4 (GDL10BA), consistent with the denser fiber structure, smaller pore sizes, and presumably lower permeability of the Freudenberg materials. However, replacing the anode-side GDL with GDL39BB in combination 6 does not substantially change the acid concentration. This reinforces the conclusion that water transport to the anode side is primarily controlled by the cathode-side conditions rather than by the permeability of the anode GDL.

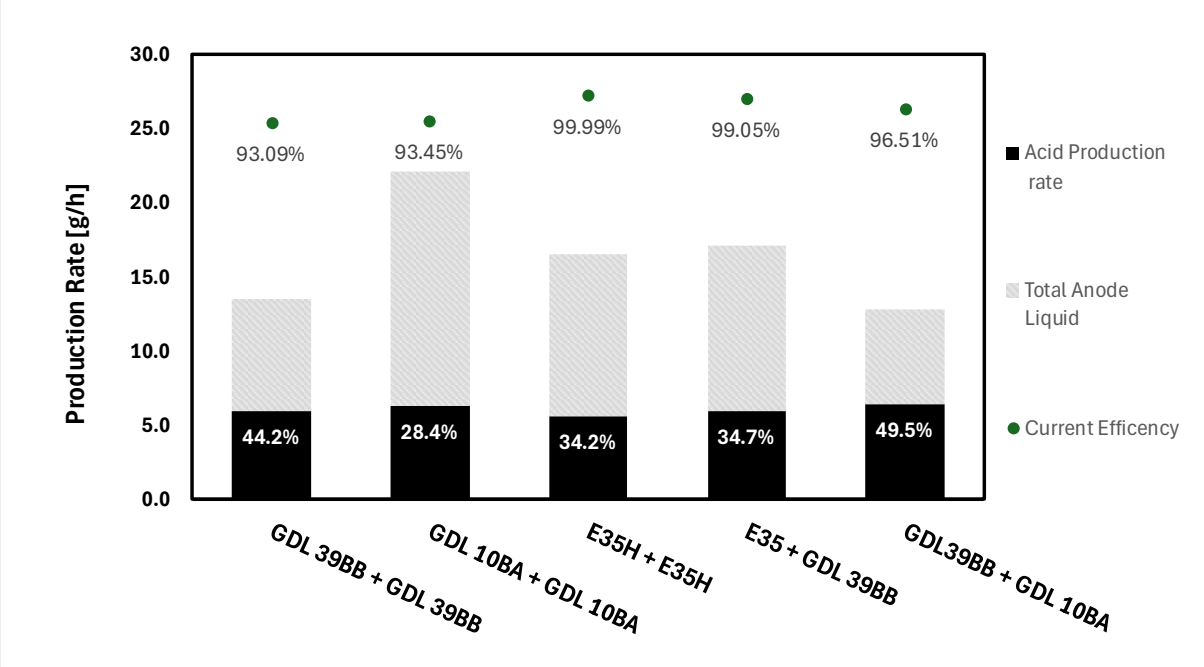

FIGURE 15 *| Anodic product analysis for the five GDL combinations subjected to 4-hour stability testing. The plots show the total liquid production rate (sulfuric acid and water), the pure H_2SO_4 production rate, the weight percentage (wt.%) of the produced acid, and the calculated current efficiency for each tested configuration.*

5.4. Hypothesis: Anodic reaction behaviour and ideal operation

During the course of the experiments, several configurations initially appeared capable of high performance (i.e., achieving high current densities) during boundary testing but were later unable to reproduce these results. When the SO_2 flow was increased (as described in the experimental section), these cells unexpectedly showed a rapid decline in performance (i.e., decreasing current) (FIGURE 16/D). Because the affected cells had previously operated on the scale of hours without comparable current decay. The abrupt performance loss occurring within less than 10 min after increasing the SO_2 flow is unlikely to originate from catalyst poisoning due to SO_2 crossover. If crossover had been the dominant cause, a gradual decline would be expected already during the preceding operation, rather than a sudden drop immediately after changing the anodic feed. These cells also did not recover or return to a stable operating state even after the SO_2 flow was reduced to the level at which they had previously been stable.

It is observed that there is a difference in the behavior of the anode outlet stream between

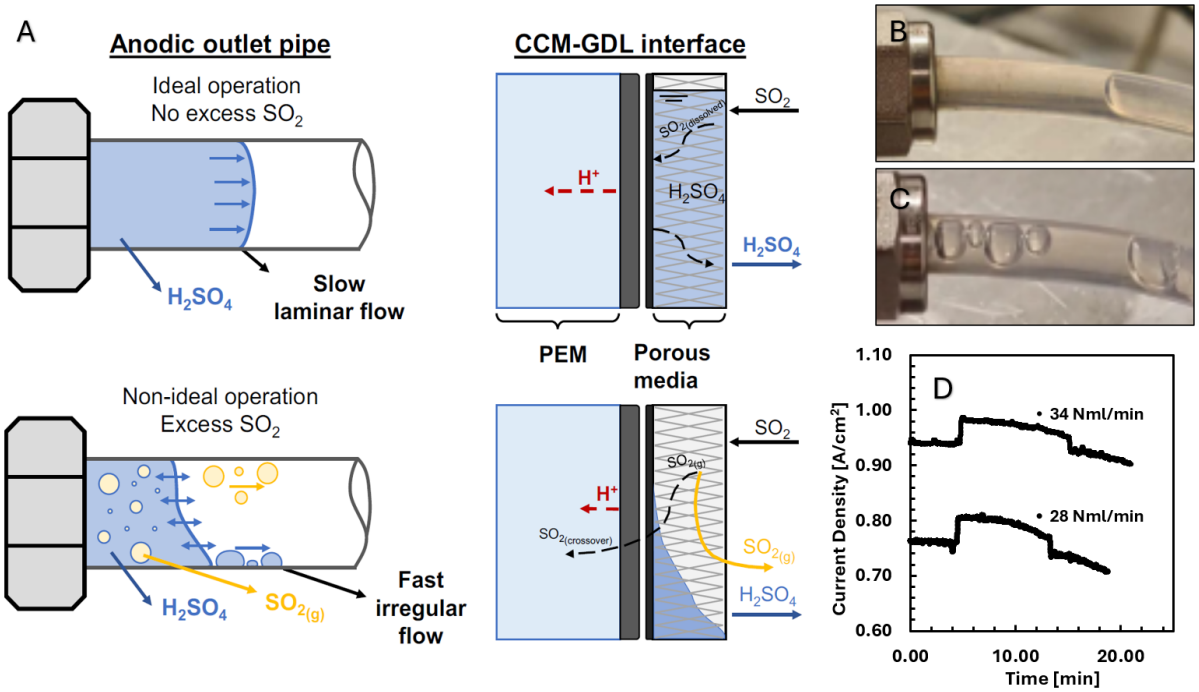

FIGURE 16 | ***A)*** *Schematic overview of the hypothesized anode operation environment during ideal operation (top) and non-ideal operation with excess SO_2 (bottom).* ***B)*** *Photographic observation of the anodic outlet pipe during successful operation.* ***C)*** *Photographic observation of the anodic outlet pipe during unsuccessful operation, displaying fast, irregular flow with gas bubbles.* ***D)*** *Current density response showing the observed decrease over a 20-minute timespan during unsuccessful cell operation. Adapted from: (L. Roessler Escudero et al., 2026)[93]*

a "successful" and "failed" testing. Under conditions where the cell operates successfully, the produced acid leaves the cell in a way that resembles plug-flow: the acid exits the cell slowly and uniformly, and no SO_2 gas bubbles are visible. (FIGURE 16/B) In contrast, when the outlet flow becomes irregular and is accompanied by bubble formation, experiments that initially appear stable later show a rapid decline in current.

(FIGURE 16/C) This makes bubble formation an early warning signal for potential operational instability.

These observations lead to a working hypothesis that can help to explain the above-described behavior. Before operation, the cell must first be humidified to ensure sufficient membrane conductivity. During this step, water diffuses from the cathode to the anode side, wetting both the membrane and the anode-side GDL. Therefore, when operation is initiated, the anode GDL can reasonably be assumed to be in a flooded state. We hypothesize that maintaining this flooded state is essential for stable operation. In other words, the GDL must retain the acid to maintain performance and long-term operation. The incoming SO_2 should therefore not purge or displace the acid from the GDL pores. Instead, SO_2 should either dissolve into the retained liquid phase or pass mainly through the flow-field channels without disturbing the acid-filled GDL.

As previously discussed, the SDE cell is operated with a stoichiometric SO_2 supply, ideally close to 100% conversion. Under these conditions, SO_2 crossover is expected to be minimal, and the anolyte is not expected to become saturated with SO_2. This should allow the incoming SO_2 to dissolve readily into the liquid phase and diffuse toward the catalyst layer without *"flushing-out"* the acid from the GDL pores. Consequently, this operating mode is hypothesized to preserve a plug-flow-like condition within the anode. We assume that when the SO_2 flow is increased too suddenly or exceeds a certain value, a portion of the gas remains undissolved, displacing the anolyte within the porous structure. Even a slight excess of SO_2 proved to be enough to expel liquid from the GDLs pore structure, causing the system to destabilize, leading to the observed rapid decline in current.

To support our hypothesis, results from two cells corresponding to combination 4 (GDL10BA) are presented. Both experiments follow the same start-up procedure and identical pre-conditioning (humidification). The only difference between the two tests is the maximum SO_2 feed rate: the first cell is operated at 28 Nml/min, a value previously shown to support stable 4-hour operation, while the second cell is operated at 30 Nml/min. This 2 Nml/min increase represents the smallest possible adjustment permitted by the mass-flow controller, corresponding to a 1% change in valve opening.

Ideally both cells would maintain steady operation near 0.8 A/cm^2. As expected, however, the increased SO_2 flow destabilizes the second cell, leading to a current decline of approximately 25 mA/cm^{2}h over the 4-hour experiment (a total loss of ~100 mA/cm^2). In contrast, the cell operated at 28 Nml/min shows no measurable current decay throughout the test period and exhibited no signs of sulfur deposition on the cathode. (FIGURE 17/A)

The corresponding impedance spectra are shown on FIGURE 17/B. At first, the higher impedance observed at the lower SO_2 flow rate may appear unfavorable. However, this outcome is expected when considering that, under these conditions, the reactant is

severely limited due to the nearly complete conversion of SO_2 on the anode side. As a result, mass-transport limitation might already contribute to the measured impedance at the high-frequency region. When the SO_2 flow is increased slightly, mass-transport limitations are reduced, and the corresponding impedance decreases accordingly. These results further support our hypothesis of the benefits of a flooded anode side GDL.

This hypothesis would explain the following observations.

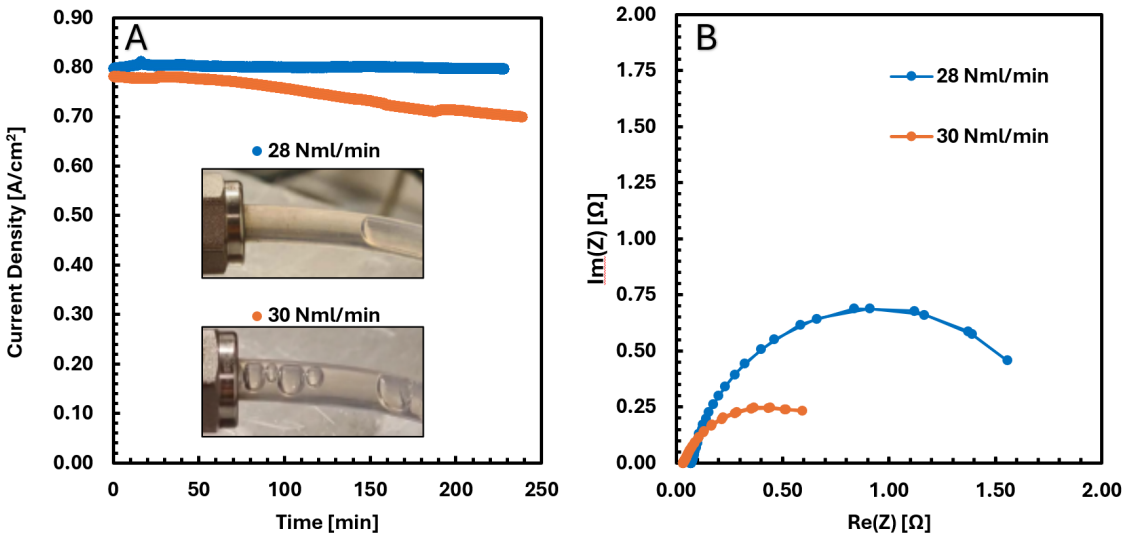

***FIGURE 17** | Proof of concept experiment for the anode flow hypothesis. **A)** Current density response over a 4-hour operation period, including photographic insets of the anodic outlet for stable (28 Nml/min) and unstable (30 Nml/min) flow behavior. **B)** EIS data recorded at the end of testing for both flow conditions.*

- Why the first stage of start-up (6 Nml/min SO2) requires 10-20 minutes to reach steady state, whereas the following 2 Nml/min increments stabilize much faster.
- Why large flow increases during boundary testing (4 Nml/min) frequently caused sudden current drops and prevented the cell reaching an operation point that was previously observed to be stable.
- Why these cell are unable to “recover” the steady state once is lost, i.e. if a current decrease occurs after a flow increase, reducing the SO_2 flow back to the earlier stable value does not typically lead to recovery.

5.4. Overview of the tested combinations

With all the combinations proposed tested, TABLE 9 shows the overview of the results, with the highlights of each experimental combination.

***TABLE 9** | Result overview of tested combinations. Adopted from: [101]*

Comb.	Cathode	Anode	Operation	Max. current (A/cm^2) 1.2 V	Observations
1	GDL39BB	GDL39BB	Possible	~0.90	Easiest combination to assemble
2	H24C5	H24C5	Not possible	-	Not suitable for SDE
3	E35	E35	Not possible	-	Not suitable for SDE
4	GDL10BA	GDL10BA	Possible	~0.80	Hard to achieve leak-free assembly
5	E35H	E35H	Possible	~0.64	Hard to achieve assembly without CCM piercing
6	E35	GDL39BB	Possible	~0.96	-
7	E35	H24C5	Not possible	-	Not suitable for SDE
8	GDL10BA	GDL39BB	Possible	~1.17	Remarkable performance and easy assembly
9	E35H	GDL39BB	Possible	~0.54	-
10	GDL39BB	GDL10BA	Possible	~0.76	-
11	E35	GDL10BA	Possible	~1.31	Best performing combination, however very challenging assembly

The main trends emerging from the complete data set are as follows:

- **GDL performance in the SDE depends not only on the material properties but whether it's employed on the anode or cathode side.**

This is evident from combinations 8 and 10, which use the same two GDLs in reversed positions. Replacing GDL10BA at the cathode and GDL39BB at the anode in combination 8 with GDL39BB at the cathode and GDL10BA at the anode in combination 10 decreases the maximum current density from approximately 1.17 to 0.76 A/cm^2. Further evidence is provided by combinations employing E35: although it could not sustain operation in the symmetric configuration, it enabled high current densities when used exclusively at the cathode in combinations 6 and 11.

- **The anode requires sufficiently open and connected transport pathways.**

H24C5 was unsuitable both in the symmetric configuration and when used as the anode in combination 7. Its compact MPL showed no visible cracks, and mercury did not

penetrate this structure within the accessible measurement range. Together with its very low air permeability, this indicates that the MPL restricts mass transport. In contrast, GDL39BB also contains an MPL but remains operable because its cracked and more porous MPL provides transport pathways through the layer.

- **The cathode benefits from a GDL that retains water while permitting hydrogen removal.**

E35 failed when used symmetrically but performed well when used exclusively as the cathode GDL in combinations 6 and 11. Likewise, GDL10BA gave high boundary-test currents when placed at the cathode in combination 8. These results indicate that the cathode requires sufficient water inventory to maintain CCM humidification and sustain water transport toward the anode. This function is not controlled by wettability alone: E35 likely retains water because of its more hydrophilic fibrous structure, whereas GDL10BA provides high water capacity through its large pore volume and open structure despite its PTFE treatment.

- **An MPL is not mandatory for high performance, but it is mechanically beneficial.**

The highest current density was achieved using the MPL-free combination E35/GDL10BA. Thus, an MPL is not inherently required for efficient SDE operation. However, GDL39BB provided a useful compromise between transport and practical handling: its MPL protected the CCM during assembly, while the cracks and pores within the MPL preserved sufficient transport. In contrast, the MPL-free felt materials were more difficult to assemble. Therefore, a future SDE-specific MPL should primarily serve as a protective and contact-improving layer.

6. Conclusion

As part of this master's thesis, a detailed literature review was carried out to establish the current state of SDE technology. The review covered the principal cell configurations, including liquid-fed and gas-fed operation, as well as the influence of operating conditions such as temperature, pressure, and acid concentration. Attention was given to material selection, since membrane properties and GDL structure strongly influence water management, SO_2 transport, acid removal, and overall mass transport within the cell.

Building on the gas-fed SDE concept reported in the literature, this work systematically evaluated commercially available gas-diffusion media from Sigracet and Freudenberg to identify the GDL properties most suitable for sulfur-dioxide depolarized electrolysis. The in-situ performance results, supported by ex-situ characterization, demonstrated that the two sides of the cell require different GDL properties.

A high permeability combined with a broad pore-size distribution is beneficial on both sides of the cell, as it supports the simultaneous transport of gases (H_2, SO_2) and liquids. Hydrophobic treatment was found to be advantageous on the anode side, where it promotes efficient removal of the acidic product. In contrast, hydrophobicity was disadvantageous on the cathode side, where increased water retention is required to help prevent membrane dry out. The presence of an MPL did not lead to a clear or consistently higher performance. In fact, for the H24C5 GDL, the highly compact MPL rendered the material unsuitable for SDE operation. From a user perspective however, the MPL proved useful; it acted as a protective layer, preventing the underlying carbon fibers from damaging the membrane during assembly. The MPL also noticeably reduced permeability, which in turn led to higher acid concentrations, reaching up to 49.5 wt.%. Current densities of 0.96 A /cm2 and 1.17 A/cm^2 were achieved for configuration 6 (E35/GDL39BB) and 8 (GDL10BA/ GDL39BB) respectively. These results suggest that, although the MPL in GDL39BB enables adequate water transport, due to the relatively large cracks on its surface, and offers practical benefits during assembly, it does not represent the optimal diffusion-media configuration for SDE operation.

The titration results show that the measured current was predominantly associated with the intended SDE reaction. The near 100% current efficiencies confirm that the currents obtained were not caused by parasitic SO_2 reduction reactions. The differences in acid concentration and total liquid production further indicate that water availability at the anode is controlled mainly by cathode-side GDL properties, whereas the anode GDL determines whether this water can maintain a stable acidic environment.

Several of the investigated combinations were able to reach the target current density of 1 A/cm^2. The best-performing configuration—configuration 11 (E35 /GDL10BA)—achieved 1.31 A/cm^2, highlighting the potential for high performance, competitive with

currently deployed electrolyzer technologies. Nevertheless, the current densities at which stable operation could be maintained were generally lower, typically in the range of 0.75–0.85 A/cm^2 for combination 1(GDL39BB), 4(GDL10BA), 5(E35H), 6(E35/GDL39BB), and 10 (GDL39BB/GDL10BA) Taken together, these results establish concrete design guidelines for GDLs specifically suited to SDE: At the cathode, the GDL must retain sufficient water to sustain membrane hydration and water transfer toward the anode, while allowing H_2 bubbles to leave the cell. At the anode, the GDL must maintain a continuous acidic liquid phase near the catalyst layer while still providing sufficiently open pathways for SO_2 access and H_2SO removal.

The findings form a foundation for the targeted development of next-generation diffusion media aimed at improving the performance, stability, and scalability of sulfur-depolarized electrolysis.

Bibliography

[1] "Global Energy Review 2025 – Analysis - IEA." Accessed: May 09, 2026. [Online]. Available: https://www.iea.org/reports/global-energy-review-2025

[2] "Renewables 2025 – Analysis - IEA." Accessed: May 09, 2026. [Online]. Available: https://www.iea.org/reports/renewables-2025

[3] J. O. M. Bockris, "The hydrogen economy: Its history," *Int. J. Hydrogen Energy*, vol. 38, no. 6, pp. 2579–2588, Feb. 2013, doi: 10.1016/J.IJHYDENE.2012.12.026.

[4] "About - Welcome to the International Association for Hydrogen Energy." Accessed: Sep. 29, 2025. [Online]. Available: https://www.iahe.org/en/about

[5] "The Future of Hydrogen – Analysis - IEA." Accessed: Aug. 29, 2025. [Online]. Available: https://www.iea.org/reports/the-future-of-hydrogen

[6] "Global Hydrogen Review 2025 – Analysis - IEA." Accessed: May 09, 2026. [Online]. Available: https://www.iea.org/reports/global-hydrogen-review-2025

[7] K. T. Møller, T. R. Jensen, E. Akiba, and H. wen Li, "Hydrogen - A sustainable energy carrier," *Progress in Natural Science: Materials International*, vol. 27, no. 1, pp. 34–40, Feb. 2017, doi: 10.1016/J.PNSC.2016.12.014.

[8] G. Voitic *et al.*, "Hydrogen Production," *Fuel Cells and Hydrogen: From Fundamentals to Applied Research*, pp. 215–241, Jan. 2018, doi: 10.1016/B978-0-12-811459-9.00010-4.

[9] S. A. Grigoriev and V. N. Fateev, "Hydrogen Production by Water Electrolysis," *Hydrogen Production Technologies*, pp. 231–276, Jan. 2017, doi: 10.1002/9781119283676.CH6;PAGEGROUP:STRING:PUBLICATION.

[10] "Observatory Reports | The European hydrogen market landscape." Accessed: May 10, 2026. [Online]. Available: https://observatory.clean-hydrogen.europa.eu/tools-reports/observatory-reports?keys=The+European+hydrogen+market+landscape+-+November+2025&created=2025&year=2025&items_per_page=10

[11] M. M. Hossain Bhuiyan and Z. Siddique, "Hydrogen as an alternative fuel: A comprehensive review of challenges and opportunities in production, storage, and transportation," *Int. J. Hydrogen Energy*, vol. 102, pp. 1026–1044, Feb. 2025, doi: 10.1016/j.ijhydene.2025.01.033.

[12] "The European Green Deal - European Commission." Accessed: May 10, 2026. [Online]. Available: https://commission.europa.eu/strategy-and-policy/priorities-2019-2024/european-green-deal_en

[13] “Key actions of the EU Hydrogen Strategy.” Accessed: May 10, 2026. [Online]. Available: https://energy.ec.europa.eu/topics/eus-energy-system/hydrogen/key-actions-eu-hydrogen-strategy_en

[14] “European Clean Hydrogen Alliance - Internal Market, Industry, Entrepreneurship and SMEs.” Accessed: May 10, 2026. [Online]. Available: https://single-market-economy.ec.europa.eu/industry/industrial-alliances/european-clean-hydrogen-alliance_en

[15] “Hydrogen.” Accessed: May 10, 2026. [Online]. Available: https://energy.ec.europa.eu/topics/eus-energy-system/hydrogen_en

[16] “Hydrogen and decarbonised gas market.” Accessed: May 10, 2026. [Online]. Available: https://energy.ec.europa.eu/topics/markets-and-consumers/hydrogen-and-decarbonised-gas-market_en

[17] “REPowerEU.” Accessed: Sep. 01, 2025. [Online]. Available: https://commission.europa.eu/topics/energy/repowereu_en

[18] A. Deasy-Millar, D. Fraile, M. Muron, G. Pawelec, S. Santos, and O. Staudenmayer, “Clean Hydrogen Monitor 2025,” Brussels, Sep. 2025.

[19] “COMMITTEE AND THE COMMITTEE OF THE REGIONS A hydrogen strategy for a climate-neutral Europe.” [Online]. Available: https://www.eu2018.at/calendar-events/political-events/BMNT-

[20] European Hydrogen Observatory, “The European hydrogen market landscape,” Brussels, Nov. 2025. [Online]. Available: https://observatory.clean-hydrogen.europa.eu/.

[21] “European Hydrogen Bank - European Commission.” Accessed: May 10, 2026. [Online]. Available: https://energy.ec.europa.eu/topics/eus-energy-system/hydrogen/european-hydrogen-bank_en

[22] “European Clean Hydrogen Alliance - European Commission.” Accessed: Sep. 01, 2025. [Online]. Available: https://single-market-economy.ec.europa.eu/industry/industrial-alliances/european-clean-hydrogen-alliance_en

[23] “Mechanism to support the market development of hydrogen.” Accessed: May 10, 2026. [Online]. Available: https://energy.ec.europa.eu/topics/eus-energy-system/hydrogen/european-hydrogen-bank/mechanism-support-market-development-hydrogen_en

[24] C. Gunathilake *et al.*, “A comprehensive review on hydrogen production, storage, and applications,” *Chem. Soc. Rev.*, vol. 53, no. 22, pp. 10900–10969, Nov. 2024, doi: 10.1039/D3CS00731F.

[25] J. Incer-Valverde, A. Korayem, G. Tsatsaronis, and T. Morosuk, "'Colors' of hydrogen: Definitions and carbon intensity," *Energy Convers. Manag.*, vol. 291, p. 117294, Sep. 2023, doi: 10.1016/J.ENCONMAN.2023.117294.

[26] A. Ajanovic, M. Sayer, and R. Haas, "The economics and the environmental benignity of different colors of hydrogen," *Int. J. Hydrogen Energy*, vol. 47, no. 57, pp. 24136–24154, Jul. 2022, doi: 10.1016/J.IJHYDENE.2022.02.094.

[27] G. Pawelec, M. Muron, J. Bracht, B. Bonnet-Cantalloube, and A. Floristean, "Clean Hydrogen Monitor 2020," Brussels, 2020.

[28] J. Incer-Valverde, A. Korayem, G. Tsatsaronis, and T. Morosuk, "'Colors' of hydrogen: Definitions and carbon intensity," *Energy Convers. Manag.*, vol. 291, p. 117294, Sep. 2023, doi: 10.1016/J.ENCONMAN.2023.117294.

[29] T. Longden, F. J. Beck, F. Jotzo, R. Andrews, and M. Prasad, "'Clean' hydrogen? – Comparing the emissions and costs of fossil fuel versus renewable electricity based hydrogen," *Appl. Energy*, vol. 306, p. 118145, Jan. 2022, doi: 10.1016/J.APENERGY.2021.118145.

[30] R. W. Howarth and M. Z. Jacobson, "How green is blue hydrogen?," *Energy Sci. Eng.*, vol. 9, no. 10, pp. 1676–1687, Oct. 2021, doi: 10.1002/ESE3.956;JOURNAL:JOURNAL:20500505;CTYPE:STRING:JOURNAL.

[31] H. Nazir *et al.*, "Is the H2 economy realizable in the foreseeable future? Part I: H2 production methods," *Int. J. Hydrogen Energy*, vol. 45, no. 27, pp. 13777–13788, May 2020, doi: 10.1016/J.IJHYDENE.2020.03.092.

[32] N. Sezer, S. Bayhan, U. Fesli, and A. Sanfilippo, "A comprehensive review of the state-of-the-art of proton exchange membrane water electrolysis," *Mater. Sci. Energy Technol.*, vol. 8, pp. 44–65, Jan. 2025, doi: 10.1016/J.MSET.2024.07.006.

[33] S. Sebbahi *et al.*, "A comprehensive review of recent advances in alkaline water electrolysis for hydrogen production," *Int. J. Hydrogen Energy*, vol. 82, pp. 583–599, Sep. 2024, doi: 10.1016/J.IJHYDENE.2024.07.428.

[34] A. Balitskii, M. Ergin¸sahin, and E. Ergin¸sahin, "An Overview of Different Water Electrolyzer Types for Hydrogen Production," *Energies 2024, Vol. 17, Page 4944*, vol. 17, no. 19, p. 4944, Oct. 2024, doi: 10.3390/EN17194944.

[35] E. Eikeng, A. Makhsoos, and B. G. Pollet, "Critical and strategic raw materials for electrolysers, fuel cells, metal hydrides and hydrogen separation technologies," *Int. J. Hydrogen Energy*, vol. 71, pp. 433–464, Jun. 2024, doi: 10.1016/J.IJHYDENE.2024.05.096.

[36] L. E. Brecher, S. Spewock, and C. J. Warde, “The Westinghouse Sulfur Cycle for the thermochemical decomposition of water,” *Int. J. Hydrogen Energy*, vol. 2, no. 1, pp. 7–15, Jan. 1977, doi: 10.1016/0360-3199(77)90061-1.

[37] P. LU, “Technological aspects of sulfur dioxide depolarized electrolysis for hydrogen production,” *Int. J. Hydrogen Energy*, vol. 8, no. 10, pp. 773–781, Jan. 1983, doi: 10.1016/0360-3199(83)90207-0.

[38] “Sulfuric Acid Market - Report, Size & Industry Outlook 2026 - 2031.” Accessed: May 10, 2026. [Online]. Available: https://www.mordorintelligence.com/industry-reports/sulfuric-acid-market

[39] K. Qu, “Electrocatalytic oxidation of sulfur dioxide for hydrogen evolution: simultaneous pollutant removal coupled to energy production,” *Journal of Electroanalytical Chemistry*, vol. 996, p. 119345, Nov. 2025, doi: 10.1016/J.JELECHEM.2025.119345.

[40] M. B. Gorensek and W. A. Summers, “Hybrid sulfur flowsheets using PEM electrolysis and a bayonet decomposition reactor,” *Int. J. Hydrogen Energy*, vol. 34, no. 9, pp. 4097–4114, May 2009, doi: 10.1016/J.IJHYDENE.2008.06.049.

[41] T. R. Garrick *et al.*, “ Characterizing Voltage Losses in an SO 2 Depolarized Electrolyzer Using Sulfonated Polybenzimidazole Membranes ,” *J. Electrochem. Soc.*, vol. 164, no. 14, pp. F1591–F1595, Dec. 2017, doi: 10.1149/2.1061714JES/PDF.

[42] J. Staser, R. P. Ramasamy, P. Sivasubramanian, and J. W. Weidner, “Effect of water on the electrochemical oxidation of gas-phase S O2 in a PEM electrolyzer for H2 production,” *Electrochemical and Solid-State Letters*, vol. 10, no. 11, pp. 17–19, Aug. 2007, doi: 10.1149/1.2771529/XML.

[43] L. Xie, P. Zhang, R. Tian, P. Xiao, L. Wang, and S. Chen, “Research progress in SO2 depolarized electrolysis at INET,” *Renew. Energy*, vol. 242, p. 122424, Apr. 2025, doi: 10.1016/J.RENENE.2025.122424.

[44] A. El-Kharouf, T. J. Mason, D. J. L. Brett, and B. G. Pollet, “Ex-situ characterisation of gas diffusion layers for proton exchange membrane fuel cells,” *J. Power Sources*, vol. 218, pp. 393–404, Nov. 2012, doi: 10.1016/J.JPOWSOUR.2012.06.099.

[45] G. Athanasaki, A. Jayakumar, and A. M. Kannan, “Gas diffusion layers for PEM fuel cells: Materials, properties and manufacturing – A review,” *Int. J. Hydrogen Energy*, vol. 48, no. 6, pp. 2294–2313, Jan. 2023, doi: 10.1016/J.IJHYDENE.2022.10.058.

[46] M. F. Mathias, J. Roth, J. Fleming, and W. Lehnert, “Diffusion media materials and characterisation,” *Handbook of Fuel Cells*, Dec. 2010, doi: 10.1002/9780470974001.F303046.

[47] A. Ozden, S. Shahgaldi, X. Li, and F. Hamdullahpur, “A review of gas diffusion layers for proton exchange membrane fuel cells—With a focus on characteristics, characterization techniques, materials and designs,” *Prog. Energy Combust. Sci.*, vol. 74, pp. 50–102, Sep. 2019, doi: 10.1016/J.PECS.2019.05.002.

[48] D. Qiu, H. Janßen, L. Peng, P. Irmscher, X. Lai, and W. Lehnert, “Electrical resistance and microstructure of typical gas diffusion layers for proton exchange membrane fuel cell under compression,” *Appl. Energy*, vol. 231, pp. 127–137, Dec. 2018, doi: 10.1016/J.APENERGY.2018.09.117.

[49] S. Park and B. N. Popov, “Effect of a GDL based on carbon paper or carbon cloth on PEM fuel cell performance,” *Fuel*, vol. 90, no. 1, pp. 436–440, Jan. 2011, doi: 10.1016/J.FUEL.2010.09.003.

[50] A. El-kharouf and B. G. Pollet, “Gas Diffusion Media and their Degradation,” *Polymer Electrolyte Fuel Cell Degradation*, pp. 215–247, Jan. 2011, doi: 10.1016/B978-0-12-386936-4.10004-1.

[51] A. Bazylak, D. Sinton, Z. S. Liu, and N. Djilali, “Effect of compression on liquid water transport and microstructure of PEMFC gas diffusion layers,” *J. Power Sources*, vol. 163, no. 2, pp. 784–792, Jan. 2007, doi: 10.1016/J.JPOWSOUR.2006.09.045.

[52] A. El-Kharouf, N. V. Rees, and R. Steinberger-Wilckens, “Gas Diffusion Layer Materials and their Effect on Polymer Electrolyte Fuel Cell Performance – Ex Situ and In Situ Characterization,” *Fuel Cells*, vol. 14, no. 5, pp. 735–741, Oct. 2014, doi: 10.1002/FUCE.201300247.

[53] M. A. A. Hamzah, S. K. Kamarudin, M. Beygisangchin, N. Shaari, R. Hazan, and Z. Zakaria, “Microporous layer in proton exchange membrane fuel cells: Advancement in materials and properties,” *J. Environ. Chem. Eng.*, vol. 12, no. 6, p. 114220, Dec. 2024, doi: 10.1016/J.JECE.2024.114220.

[54] M. Ringström, H. Ekström, L. Kylhammar, G. Lindbergh, and R. W. Lindström, “Comprehensive ex-situ characterization of the compression-dependent properties of gas diffusion layers in PEM fuel cells,” *Energy Convers. Manag.*, vol. 356, p. 121319, May 2026, doi: 10.1016/J.ENCONMAN.2026.121319.

[55] A. Bazylak, D. Sinton, Z. S. Liu, and N. Djilali, “Effect of compression on liquid water transport and microstructure of PEMFC gas diffusion layers,” *J. Power Sources*, vol. 163, no. 2, pp. 784–792, Jan. 2007, doi: 10.1016/J.JPOWSOUR.2006.09.045.

[56] S. Ahmad, T. Nawaz, A. Ali, M. F. Orhan, A. Samreen, and A. M. Kannan, “An overview of proton exchange membranes for fuel cells: Materials and manufacturing,” *Int. J. Hydrogen Energy*, vol. 47, no. 44, pp. 19086–19131, May 2022, doi: 10.1016/J.IJHYDENE.2022.04.099.

[57] M. Adamski, N. Peressin, and S. Holdcroft, “On the evolution of sulfonated polyphenylenes as proton exchange membranes for fuel cells,” *Mater. Adv.*, vol. 2, no. 15, pp. 4966–5005, Aug. 2021, doi: 10.1039/D1MA00511A.

[58] K. A. Mauritz and R. B. Moore, “State of Understanding of Nafion,” *Chem. Rev.*, vol. 104, no. 10, pp. 4535–4585, Oct. 2004, doi: 10.1021/CR0207123.

[59] J. A. Staser, K. Norman, C. H. Fujimoto, M. A. Hickner, and J. W. Weidner, “Transport Properties and Performance of Polymer Electrolyte Membranes for the Hybrid Sulfur Electrolyzer,” *J. Electrochem. Soc.*, vol. 156, no. 7, p. B842, May 2009, doi: 10.1149/1.3129676.

[60] John A. Staser, J. V. Jayakumar, A. Gulledge, C. H. Kim, B. C. Benicewicz, and J. W. Weidner, “Polybenzimidazole membranes for hydrogen and sulfuric acid production in the hybrid sulfur electrolyzer,” *ECS Electrochemistry Letters*, vol. 1, no. 6, p. F44, Sep. 2012, doi: 10.1149/2.010206EEL/PDF.

[61] M. C. Elvington, H. Colón-Mercado, S. McCatty, S. G. Stone, and D. T. Hobbs, “Evaluation of proton-conducting membranes for use in a sulfur dioxide depolarized electrolyzer,” *J. Power Sources*, vol. 195, no. 9, pp. 2823–2829, May 2010, doi: 10.1016/J.JPOWSOUR.2009.11.031.

[62] H. R. Colón-Mercado *et al.*, “Electrode optimization for efficient hydrogen production using an SO2-depolarized electrolysis cell,” *Int. J. Hydrogen Energy*, vol. 47, no. 31, pp. 14180–14185, Apr. 2022, doi: 10.1016/J.IJHYDENE.2022.02.166.

[63] S. Subianto, “Recent advances in polybenzimidazole/phosphoric acid membranes for high-temperature fuel cells,” *Polym. Int.*, vol. 63, no. 7, pp. 1134–1144, Jul. 2014, doi: 10.1002/PI.4708;REQUESTEDJOURNAL:JOURNAL:10970126.

[64] H. R. Colón-Mercado and D. T. Hobbs, “Catalyst evaluation for a sulfur dioxide-depolarized electrolyzer,” *Electrochem. commun.*, vol. 9, no. 11, pp. 2649–2653, Nov. 2007, doi: 10.1016/J.ELECOM.2007.08.015.

[65] J. A. Allen, G. Rowe, J. T. Hinkley, and S. W. Donne, “Electrochemical aspects of the Hybrid Sulfur Cycle for large scale hydrogen production,” *Int. J. Hydrogen Energy*, vol. 39, no. 22, pp. 11376–11389, Jul. 2014, doi: 10.1016/J.IJHYDENE.2014.05.112.

[66] S. Díaz-Abad, M. Millán, M. A. Rodrigo, and J. Lobato, “Review of Anodic Catalysts for SO2 Depolarized Electrolysis for ‘Green Hydrogen’ Production,” *Catalysts 2019, Vol. 9, Page 63*, vol. 9, no. 1, p. 63, Jan. 2019, doi: 10.3390/CATAL9010063.

[67] J. A. O’Brien, J. T. Hinkley, and S. W. Donne, “The Electrochemical Oxidation of Aqueous Sulfur Dioxide: I. Experimental Parameter Influences on Electrode Behavior,” *J. Electrochem. Soc.*, vol. 157, no. 9, p. F111, Jul. 2010, doi: 10.1149/1.3458860.

[68] J. T. Hinkley, S. W. Donne -, S. W. Donne, J. Hinkley -, and J. Hinkley, “Electrochemical Oxidation of Aqueous Sulfur Dioxide II. Comparative Studies on Platinum and Gold Electrodes,” *J. Electrochem. Soc.*, vol. 159, no. 9, p. F585, Aug. 2012, doi: 10.1149/2.060209JES.

[69] J. A. O’Brien, J. T. Hinkley, S. W. Donne, and S. E. Lindquist, “The electrochemical oxidation of aqueous sulfur dioxide: A critical review of work with respect to the hybrid sulfur cycle,” *Electrochim. Acta*, vol. 55, no. 3, pp. 573–591, Jan. 2010, doi: 10.1016/J.ELECTACTA.2009.09.067.

[70] M. J. Ungerer, D. Santos-Carballal, C. G. C. E. van Sittert, and N. H. de Leeuw, “Competitive Adsorption of H2O and SO2 on Catalytic Platinum Surfaces: a Density Functional Theory Study,” *South African Journal of Chemistry*, vol. 74, pp. 57–68, 2021, doi: 10.17159/0379-4350/2021/V74A10.

[71] M. J. Ungerer, D. Santos-carballal, A. Cadi-essadek, C. G. C. E. van Sittert, and N. H. de Leeuw, “Interaction of SO2 with the Platinum (001), (011), and (111) Surfaces: A DFT Study,” *Catalysts 2020, Vol. 10, Page 558*, vol. 10, no. 5, p. 558, May 2020, doi: 10.3390/CATAL10050558.

[72] S. Diaz-Abad, I. Requena, M. A. Rodrigo, and J. Lobato, “When less is more: Enhancement of green hydrogen production and efficiency by using electrodes with ultra-low platinum loadings,” *J. Power Sources*, vol. 606, p. 234513, Jun. 2024, doi: 10.1016/J.JPOWSOUR.2024.234513.

[73] R. Tian *et al.*, “Study on the Pt loading strategy for SO2-depolarized electrolyzers,” *Int. J. Hydrogen Energy*, vol. 111, pp. 500–512, Mar. 2025, doi: 10.1016/J.IJHYDENE.2025.02.332.

[74] B. H. Meekins *et al.*, “In-situ and ex-situ comparison of the electrochemical oxidation of SO2 on carbon supported Pt and Au catalysts,” *Int. J. Hydrogen Energy*, vol. 45, no. 3, pp. 1940–1947, Jan. 2020, doi: 10.1016/J.IJHYDENE.2019.11.112.

[75] L. F. Roessler Escudero, G. J. Smales, V. Hacker, and M. Bodner, “Performance evaluation of gold as anodic catalyst for the operation of sulphur depolarised electrolysis,” *Clean. Eng. Technol.*, vol. 31, p. 101201, Apr. 2026, doi: 10.1016/J.CLET.2026.101201.

[76] T. Madden *et al.*, “Proton exchange membrane fuel cell degradation: mechanisms and recent progress,” *Handbook of Fuel Cells*, Dec. 2010, doi: 10.1002/9780470974001.F500057.

[77] J. Kim, J. Lee, and Y. Tak, “Relationship between carbon corrosion and positive electrode potential in a proton-exchange membrane fuel cell during start/stop operation,” *J. Power Sources*, vol. 192, no. 2, pp. 674–678, Jul. 2009, doi: 10.1016/J.JPOWSOUR.2009.03.039.

[78] L. Messing *et al.*, “Carbon Bipolar Plates in PEM Water Electrolysis: Bust or Must?,” *Adv. Energy Mater.*, vol. 14, no. 40, p. 2402308, Oct. 2024, doi: 10.1002/AENM.202402308.

[79] J. L. Young, Z. Kang, F. Ganci, S. Madachy, and G. Bender, “PEM electrolyzer characterization with carbon-based hardware and material sets,” *Electrochem. commun.*, vol. 124, p. 106941, Mar. 2021, doi: 10.1016/J.ELECOM.2021.106941.

[80] L. Roessler Escudero, V. Hacker, and M. Bodner, “Adjusting the operating boundaries for the mitigation of SO2 crossover in sulphur depolarized electrolysers,” *J. Power Sources*, vol. 622, p. 235329, Dec. 2024, doi: 10.1016/J.JPOWSOUR.2024.235329.

[81] X. Ding, S. Chen, L. Wang, and P. Zhang, “INET - Study on electrochemical impedance spectroscopy and cell voltage composition of a PEM SO2-depolarized electrolyzer using graphite felt as diffusion layer,” *Electrochim. Acta*, vol. 426, p. 140837, Sep. 2022, doi: 10.1016/J.ELECTACTA.2022.140837.

[82] J. L. Steimke, T. J. Steeper, H. R. Cólon-Mercado, and M. B. Gorensek, “Development and testing of a PEM SO2-depolarized electrolyzer and an operating method that prevents sulfur accumulation,” *Int. J. Hydrogen Energy*, vol. 40, no. 39, pp. 13281–13294, Oct. 2015, doi: 10.1016/J.IJHYDENE.2015.08.041.

[83] X. Ma *et al.*, “Comparison of various structure designs of SO2-depolarized electrolysis cell,” *Int. J. Hydrogen Energy*, vol. 48, no. 14, pp. 5428–5437, Feb. 2023, doi: 10.1016/J.IJHYDENE.2022.11.148.

[84] A. J. Krüger, H. M. Krieg, S. A. Grigoriev, and D. Bessarabov, “Various operating methods and parameters for SO2 electrolysis,” *Energy Sci. Eng.*, vol. 3, no. 5, pp. 468–480, Sep. 2015, doi: 10.1002/ESE3.80;REQUESTEDJOURNAL:JOURNAL:20500505;PAGE:STRING:ARTICLE/CHAPTER.

[85] P. K. Sivasubramanian, R. P. Ramasamy, F. J. Freire, C. E. Holland, and J. W. Weidner, “Electrochemical hydrogen production from thermochemical cycles using a proton exchange membrane electrolyzer,” *Int. J. Hydrogen Energy*, vol. 32, no. 4, pp. 463–468, Mar. 2007, doi: 10.1016/J.IJHYDENE.2006.06.056.

[86] M. B. Gorensek, C. Corgnale, and W. A. Summers, “Development of the hybrid sulfur cycle for use with concentrated solar heat. I. Conceptual design,” *Int. J. Hydrogen Energy*, vol. 42, no. 33, pp. 20939–20954, Aug. 2017, doi: 10.1016/J.IJHYDENE.2017.06.241.

[87] J. A. Staser and J. W. Weidner, “Effect of Water Transport on the Production of Hydrogen and Sulfuric Acid in a PEM Electrolyzer,” *J. Electrochem. Soc.*, vol. 156, no. 1, p. B16, Oct. 2009, doi: 10.1149/1.3001923/PDF.

[88] J. A. Staser and J. W. Weidner, “Sulfur Dioxide Crossover during the Production of Hydrogen and Sulfuric Acid in a PEM Electrolyzer,” *J. Electrochem. Soc.*, vol. 156, no. 7, p. B836, May 2009, doi: 10.1149/1.3129444.

[89] D. D. Wagman *et al.*, “Erratum: The NBS tables of chemical thermodynamic properties. Selected values for inorganic and C1 and C2 organic substances in SI units [J. Phys. Chem. Ref. Data **11** , Suppl. 2 (1982)],” *J. Phys. Chem. Ref. Data*, vol. 18, no. 4, pp. 1807–1812, Oct. 1989, doi: 10.1063/1.555845.

[90] X. Lulu, Z. Ping, C. Songzhe, and W. Laijun, “INET - Quantitative analysis of the cell voltage of SO2-depolarized electrolysis in hybrid sulfur process,” *Nuclear Engineering and Design*, vol. 306, pp. 203–207, Sep. 2016, doi: 10.1016/J.NUCENGDES.2016.01.012.

[91] J. A. Staser, M. B. Gorensek, and J. W. Weidner, “Quantifying Individual Potential Contributions of the Hybrid Sulfur Electrolyzer,” *J. Electrochem. Soc.*, vol. 157, no. 6, p. B952, May 2010, doi: 10.1149/1.3397901/XML.

[92] M. B. Gorensek, B. Meekins, H. Colón-Mercado, and J. Weidner, “Parametric study of operating conditions of an SO2-depolarized electrolyzer,” *Int. J. Hydrogen Energy*, vol. 45, no. 43, pp. 22408–22418, Sep. 2020, doi: 10.1016/J.IJHYDENE.2020.06.067.

[93] M. B. Gorensek, J. A. Staser, T. G. Stanford, and J. W. Weidner, “A thermodynamic analysis of the SO2/H2SO4 system in SO2-depolarized electrolysis,” *Int. J. Hydrogen Energy*, vol. 34, no. 15, pp. 6089–6095, Aug. 2009, doi: 10.1016/J.IJHYDENE.2009.06.020.

[94] L. Xue, P. Zhang, S. Chen, and L. Wang, “INET - In-situ electrochemical impedance spectroscopy measurement of anodic reaction in SO2 depolarized electrolysis process,” *Chemical Engineering and Processing: Process Intensification*, vol. 89, pp. 70–74, Mar. 2015, doi: 10.1016/J.CEP.2015.01.005.

[95] H. R. Colón-Mercado, M. B. Gorensek, C. H. Fujimoto, A. A. Lando, and B. H. Meekins, “High-performance SO2-depolarized electrolysis cell using advanced polymer electrolyte membranes,” *Int. J. Hydrogen Energy*, vol. 47, no. 1, pp. 57–68, Jan. 2022, doi: 10.1016/J.IJHYDENE.2021.10.019.

[96] R. Tian *et al.*, “INET- Evaluation of commercial Pt/C catalysts for anode of sulfur dioxide depolarized electrolysis,” *Materials Science and Engineering: B*, vol. 313, p. 117943, Mar. 2025, doi: 10.1016/J.MSEB.2024.117943.

[97] A. Santasalo-Aarnio, J. Virtanen, and M. Gasik, “SO2 carry-over and sulphur formation in a SO2-depolarized electrolyser,” *Journal of Solid State Electrochemistry*, vol. 20, no. 6, pp. 1655–1663, Jun. 2016, doi: 10.1007/S10008-016-3169-8/METRICS.

[98] Freudenberg Performance Materials GmbH & Co. KG, “Freudenberg Gas Diffusion Layers: Technical Data,” Oct. 2019. Accessed: Jun. 30, 2026. [Online]. Available: chrome-extension://efaidnbmnnnibpcajpcglclefindmkaj/https://www.fuelcellstore.com/spec-sheets/freudenberg-gdl-technical-data.pdf

[99] Freudenberg Performance Materials GmbH & Co. KG, “Freudenberg Gas Diffusion Layers—Fuel Cell: Technical Data,” 2024. Accessed: Jun. 30, 2026. [Online]. Available: chrome-extension://efaidnbmnnnibpcajpcglclefindmkaj/https://www.fuelcellstore.com/spec-sheets/freudenberg_2024_technical_data_sheet_pemfuelcells_electrolyzers.pdf

[100] R. ’Schweiss, C. Meiser, I. Galbati, and N. Haak, “SIGRACET® Gas Diffusion Layers for PEM Fuel Cells, Electrolyzers and Batteries,” 2016. Accessed: Jun. 30, 2026. [Online]. Available: https://www.fuelcellstore.com/spec-sheets/sigracet-gdl-white-paper-new-generation.pdf

[101] L. Roessler Escudero, Á. Székeli, V. Hacker, and M. Bodner, “Evaluation of Porous Media Properties for the Performance of Sulfur-Depolarized Electrolysis,” *ChemSusChem*, vol. 19, no. 8, p. e70660, Apr. 2026, doi: 10.1002/CSSC.70660;ISSUE:ISSUE:DOI.

[102] P. Kumar Sow *et al.*, “Wettability Determination of Gas Diffusion Layers for Polymer Electrolyte Fuel Cells,” *J. Electrochem. Soc.*, vol. 173, no. 6, p. 064509, Mar. 2026, doi: 10.1149/1945-7111/AE514E.

Appendix A

SIGRACET® GDL 39BB

		PRISTINE	USED
MPL	100X	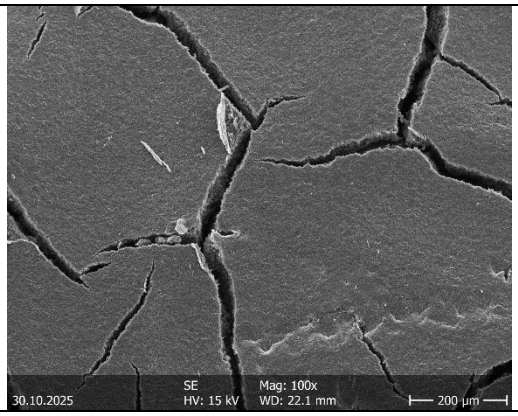	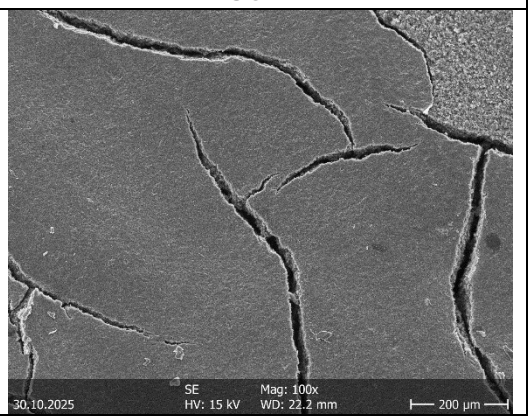

Substrate	5000x	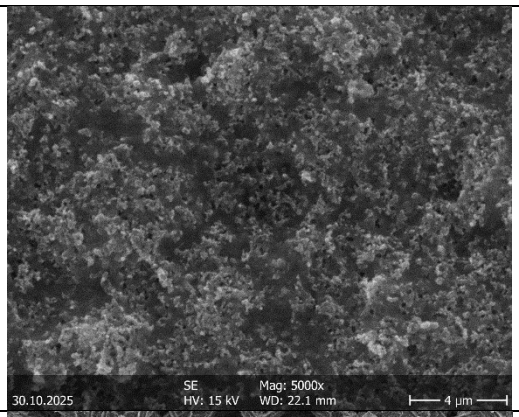	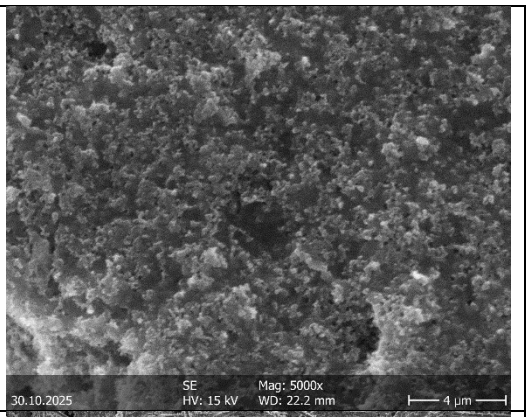
	100X	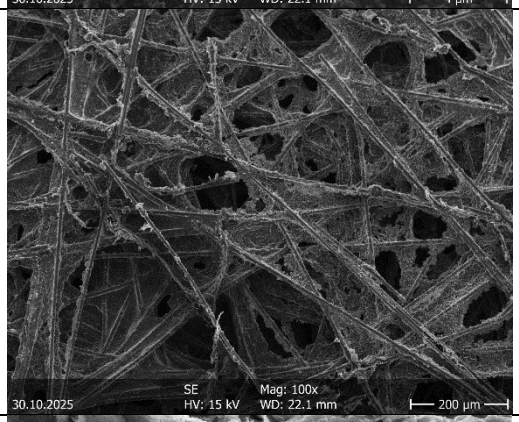	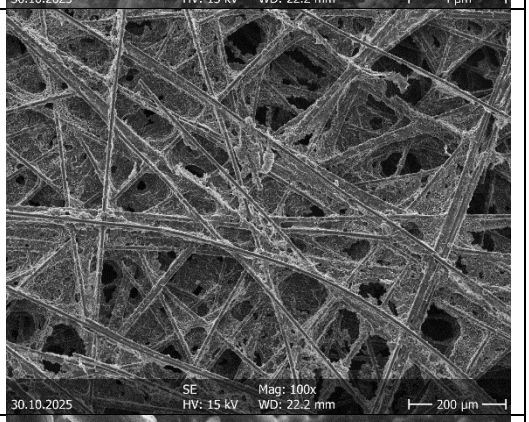
	1500x	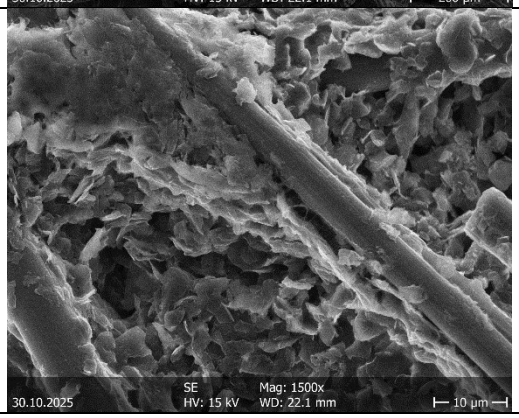	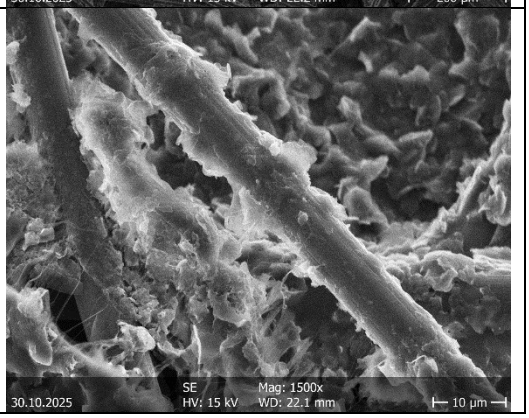

SIGRACET® GDL10BA

		PRISTINE	USED
Substrate	100X	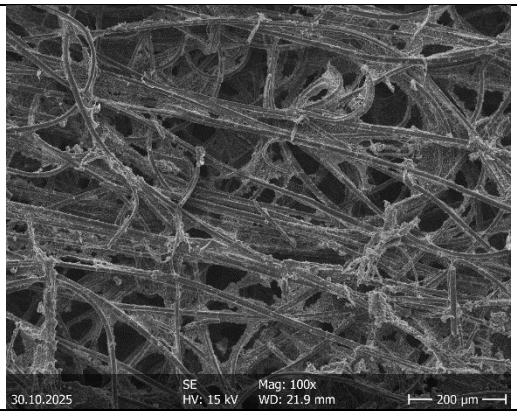	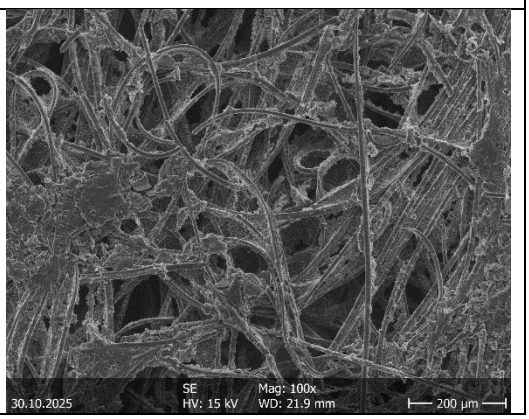

	1500x	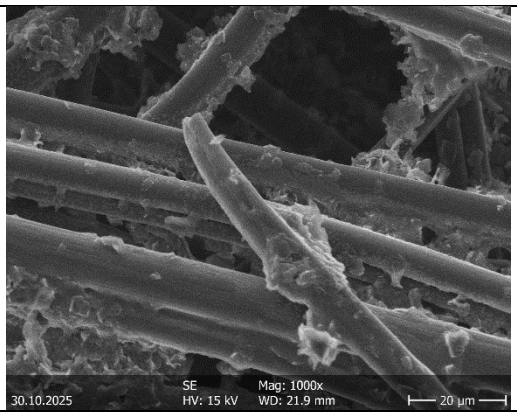	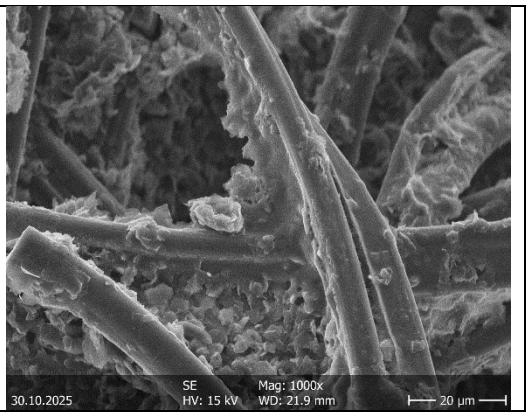

Freudenberg GDL E35

		PRISTINE	USED
Substrate	100X	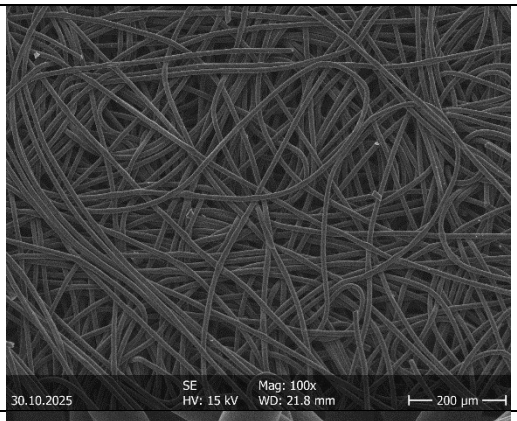	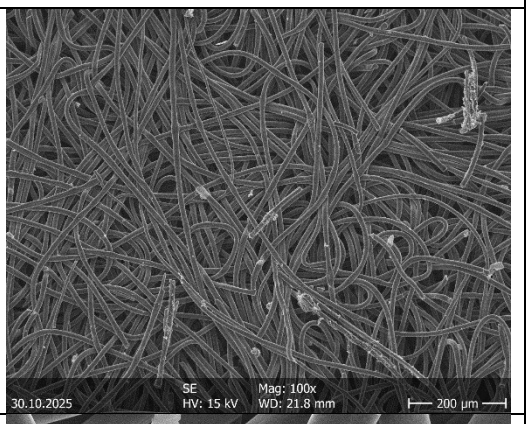
	1500x	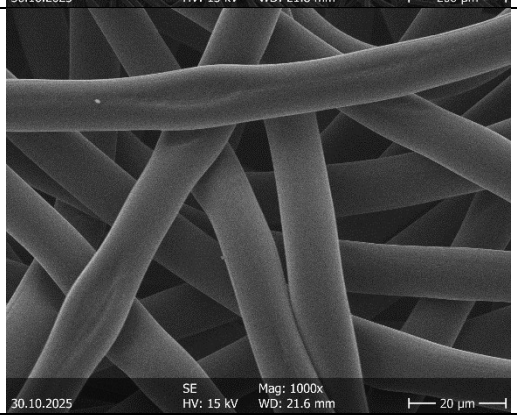	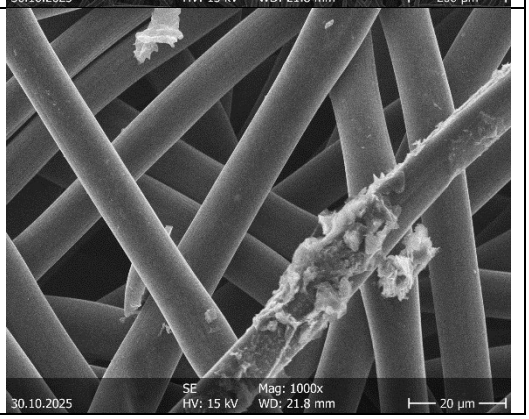

Freudenberg GDL E35H

		PRISTINE	USED
Substrate	100X	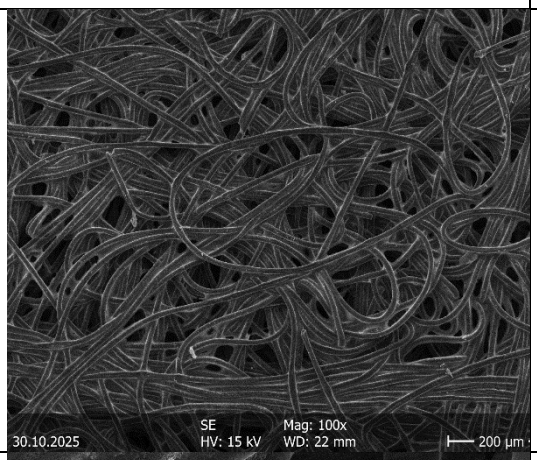	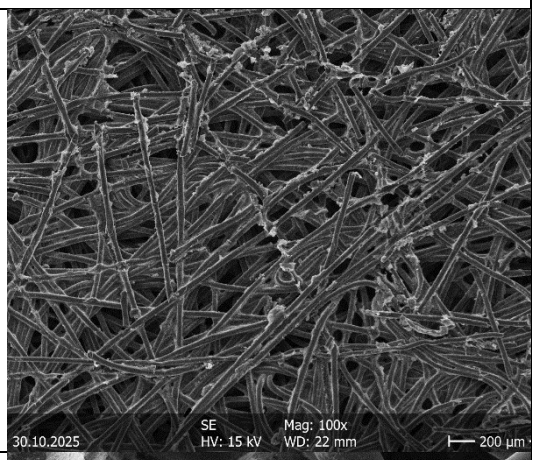
	1500x	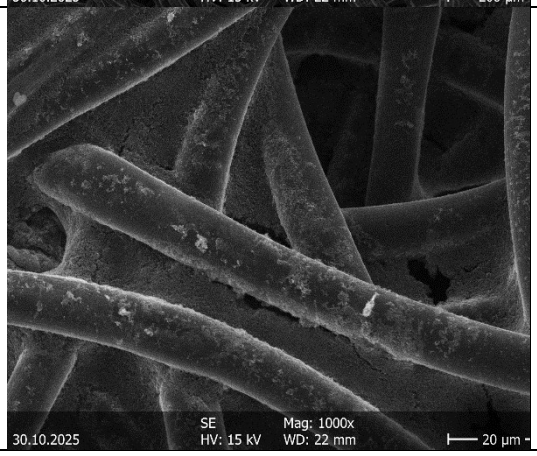	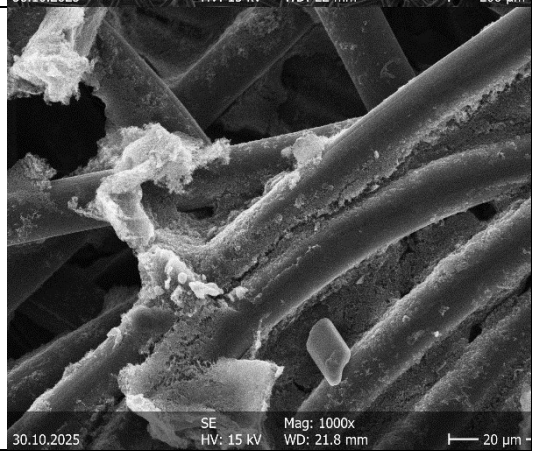

Freudenberg GDL E24C5

		PRISTINE	USED
MPL	100X	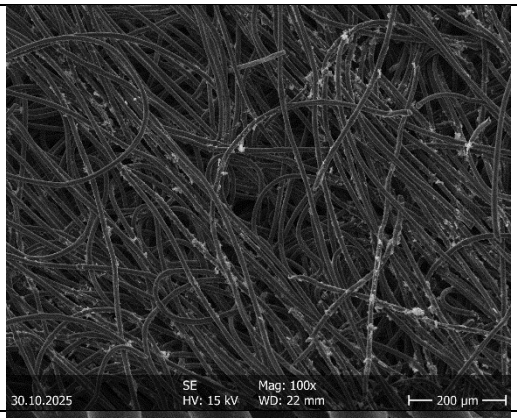	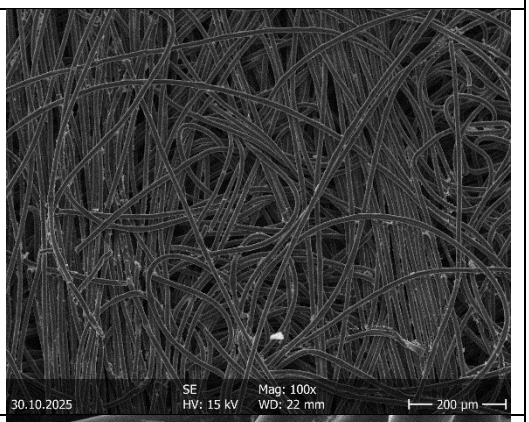
Substrate	5000x	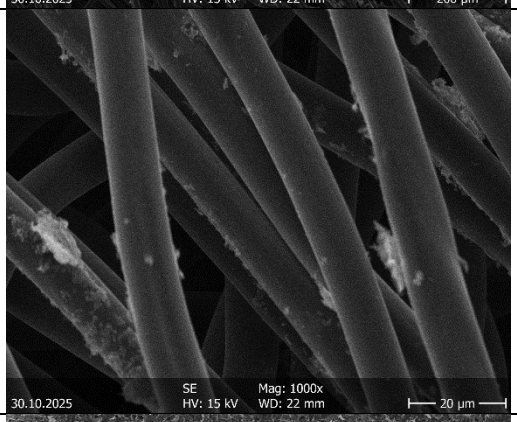	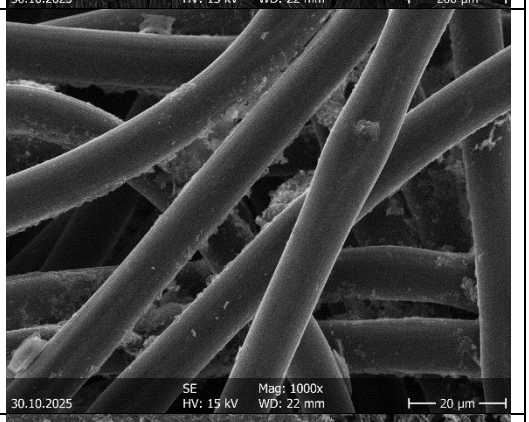
	100X	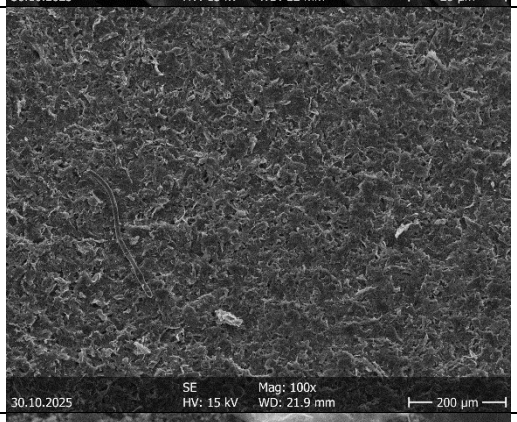	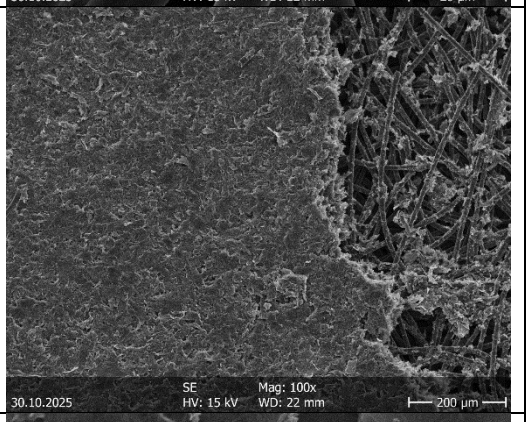
	1500x	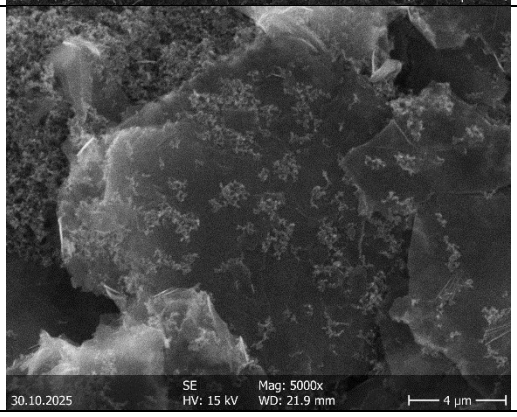	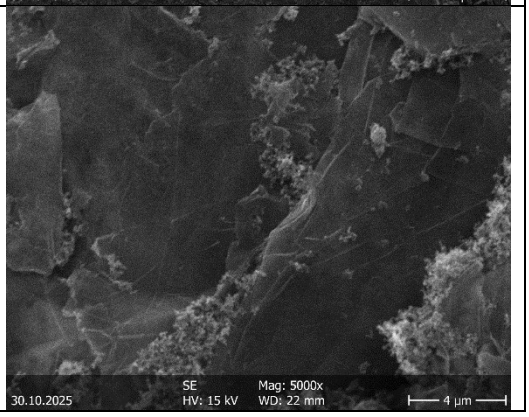

GDL Cross-section

39BB	10BA
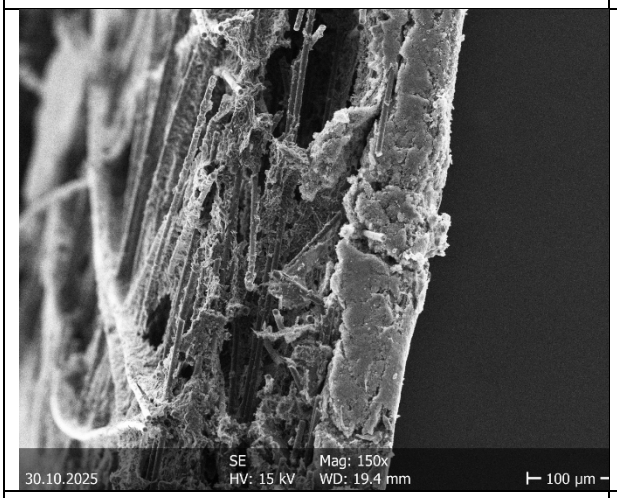	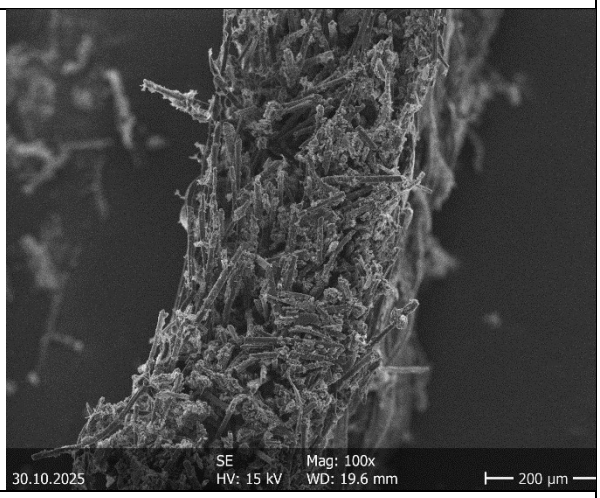
E35	**E35H**
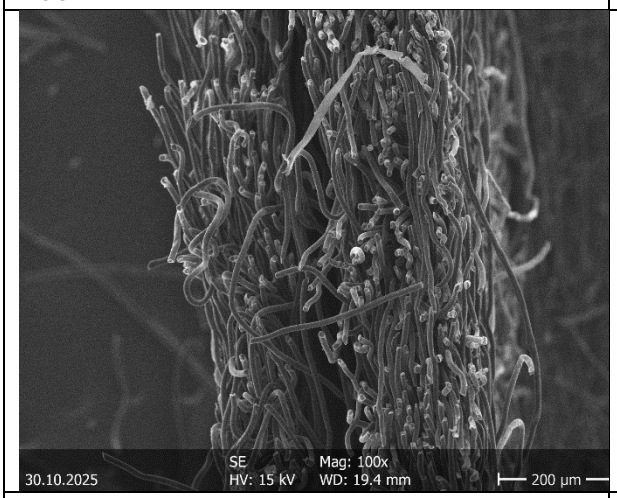	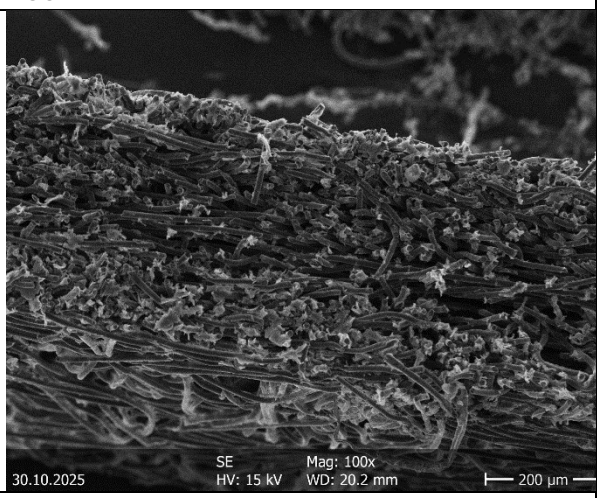
H24C5	
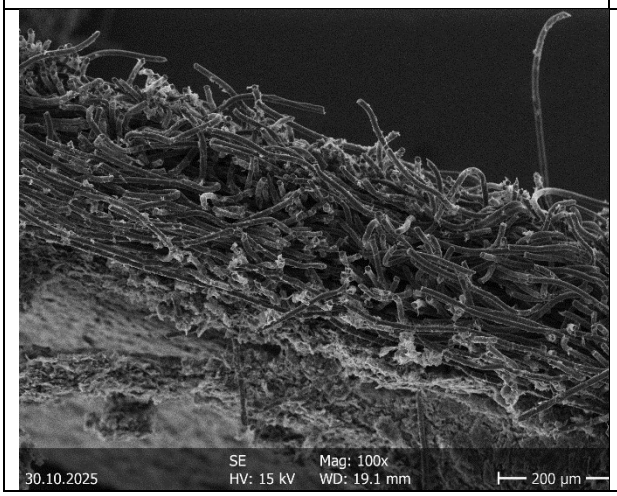	

Appendix B

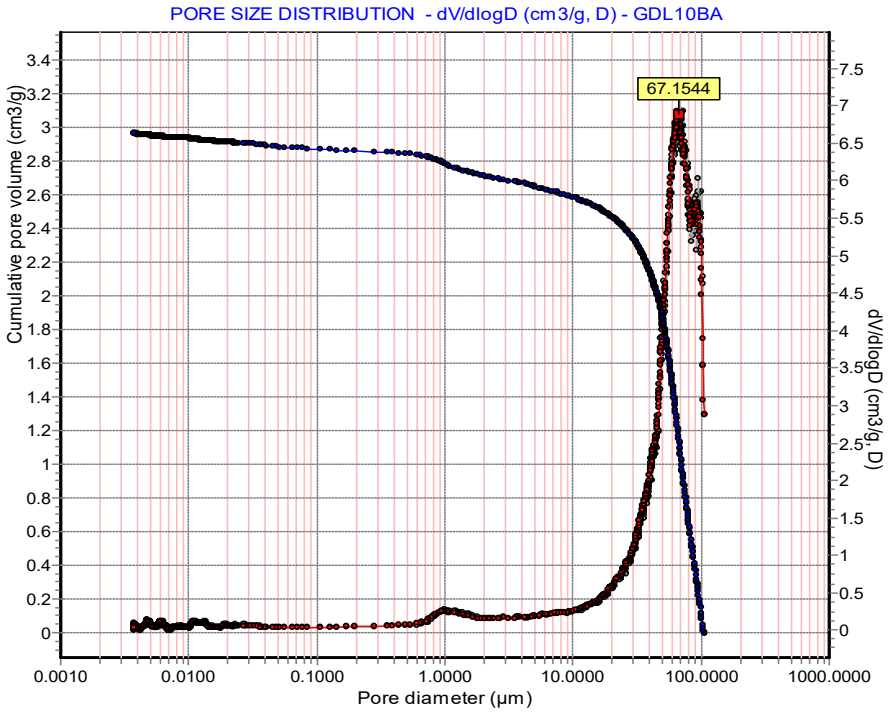
PORE SIZE DISTRIBUTION - dV/dlogD (cm3/g, D) - GDL10BA
67.1544
Cumulative pore volume (cm3/g)
dV/dlogD (cm3/g, D)
Pore diameter (µm)
0.0010
0.0100
0.1000
1.0000
10.0000
100.0000
1000.0000

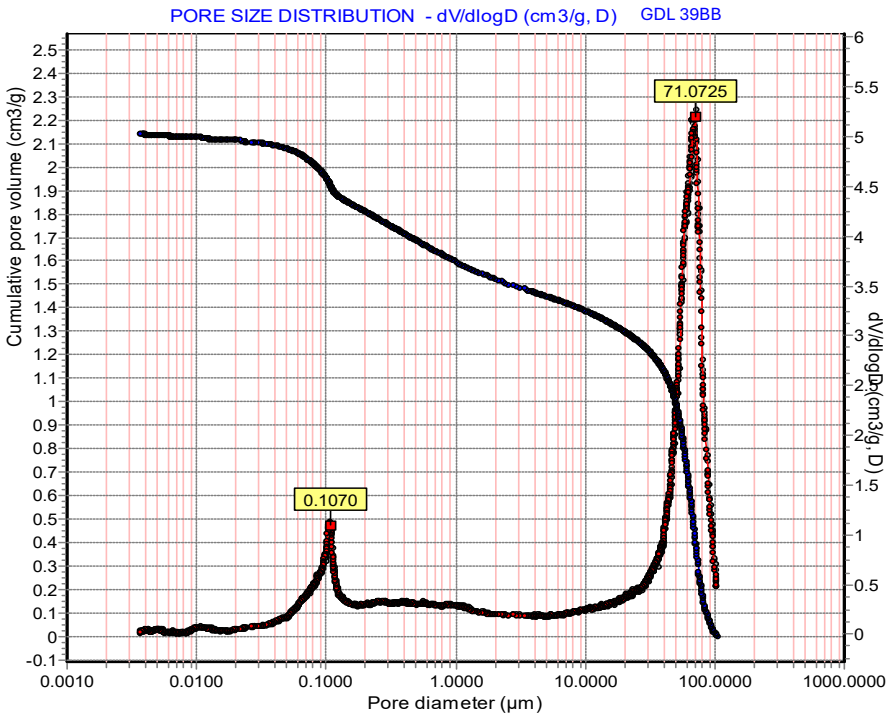
PORE SIZE DISTRIBUTION - dV/dlogD (cm3/g, D) GDL 39BB
71.0725
0.1070
Cumulative pore volume (cm3/g)
dV/dlogD (cm3/g, D)
Pore diameter (µm)
0.0010
0.0100
0.1000
1.0000
10.0000
100.0000
1000.0000

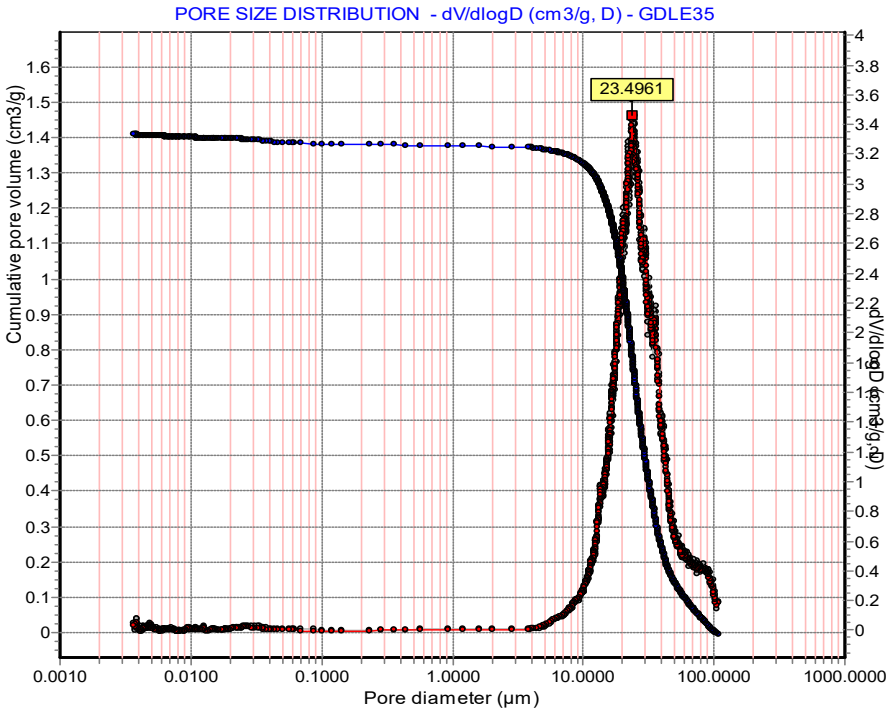
PORE SIZE DISTRIBUTION - dV/dlogD (cm3/g, D) - GDLE35
23.4961
Cumulative pore volume (cm3/g)
dV/dlogD (cm3/g, D)
Pore diameter (µm)
0.0010
0.0100
0.1000
1.0000
10.0000
100.0000
1000.0000

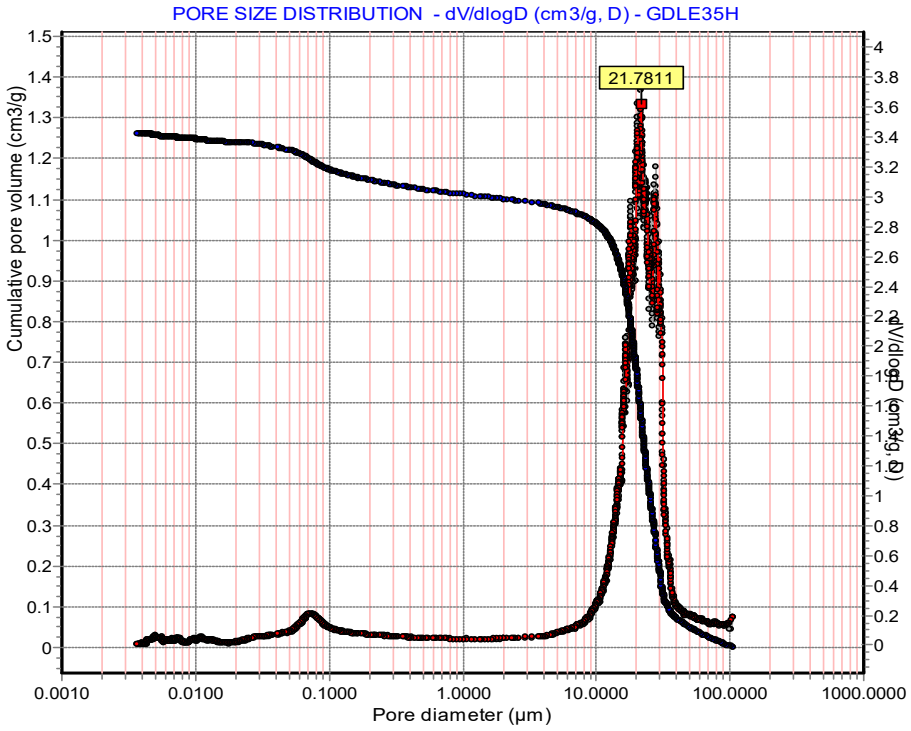
PORE SIZE DISTRIBUTION - dV/dlogD (cm3/g, D) - GDLE35H
21.7811
Cumulative pore volume (cm3/g)
dV/dlogD (cm3/g, D)
Pore diameter (µm)
0.0010
0.0100
0.1000
1.0000
10.0000
100.0000
1000.0000

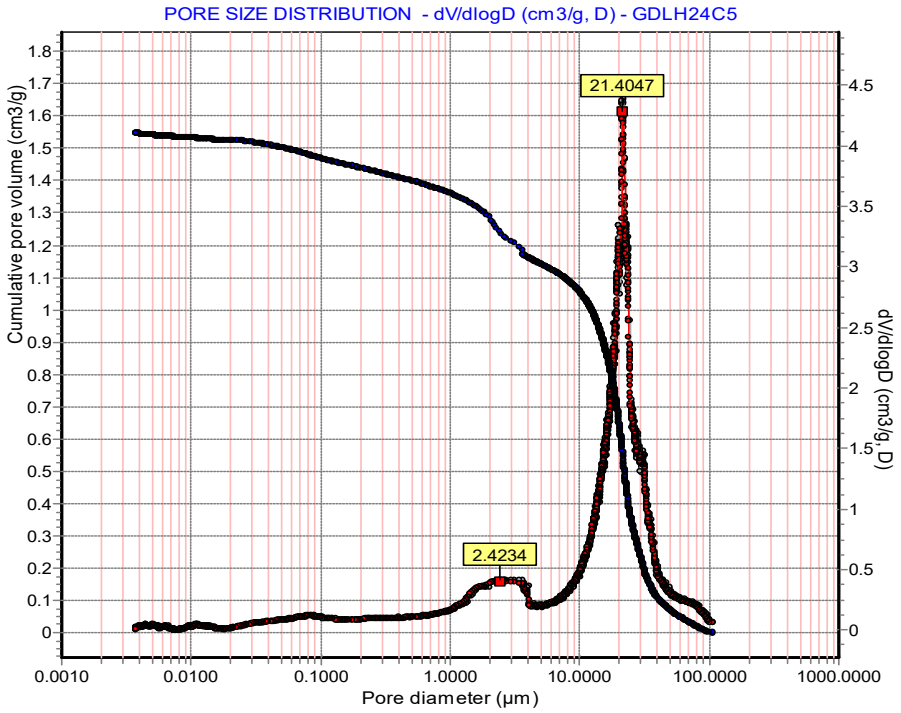

Appendix C

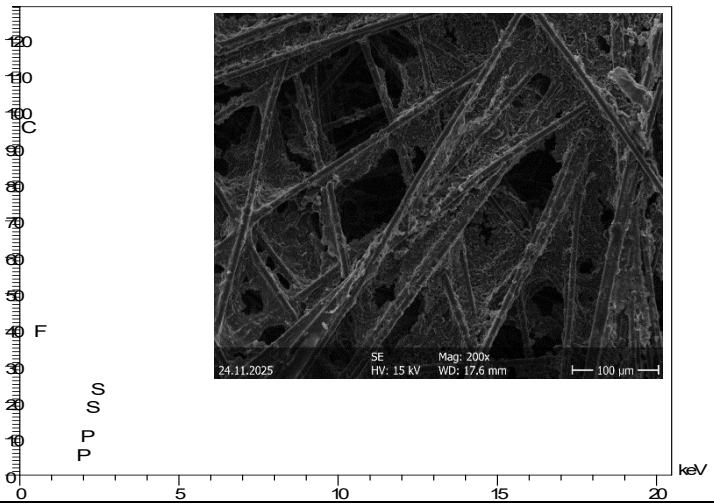

GDL39BB Substrate					
Elt	Line	Error	K	W%	A%
C	Ka	19.5975	0.7954	72.3	80.95
F	Ka	1.4237	0.1723	25.75	18.22
P	Ka	0.7782	0.0069	0.43	0.19
S	Ka	0.7782	0.0254	1.52	0.64
Total			1	100	100

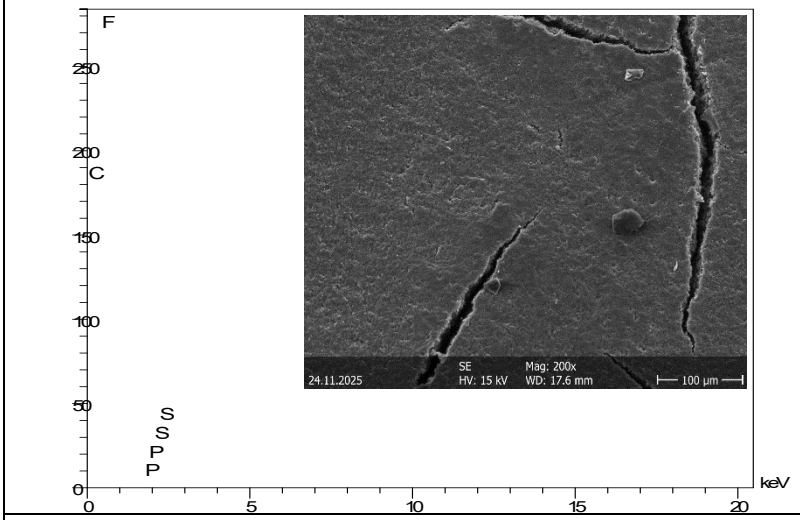

GDL39BB MPL					
Elt	Line	Error	K	W%	A%
C	Ka	25.0951	0.4718	47.37	58.81
F	Ka	1.5441	0.5219	52.27	41.03
P	Ka	0.505	0.0022	0.13	0.06
S	Ka	0.505	0.0041	0.22	0.1
Total		1		100	100

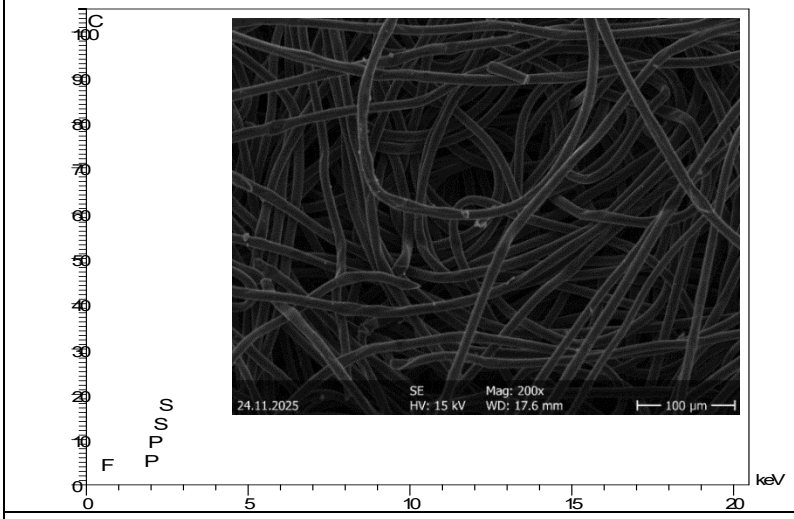

E35					
Elt	Line	Error	K	W%	A%
C	Ka	18.5374	0.9795	96.82	98.33
F	Ka	0.4329	0.0055	1.7	1.09
P	Ka	0.5733	0.0068	0.68	0.27
S	Ka	0.5733	0.0083	0.8	0.31
			1	100	100

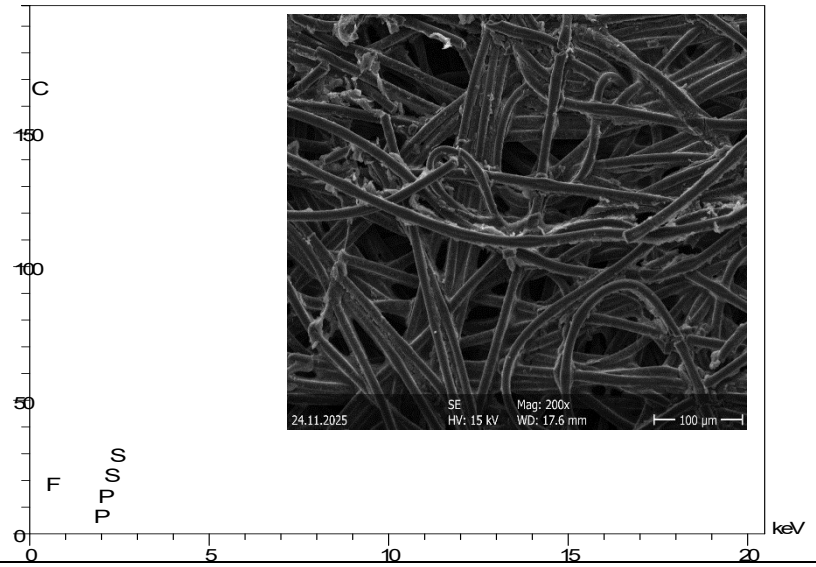

E35H					
Elt	Line	Error	K	W%	A%
C	Ka	19.9438	0.949	89.24	93.17
F	Ka	0.7886	0.0388	9.72	6.41
P	Ka	0.609	0.0048	0.42	0.17
S	Ka	0.609	0.0074	0.62	0.24
Total		1	1	100	100

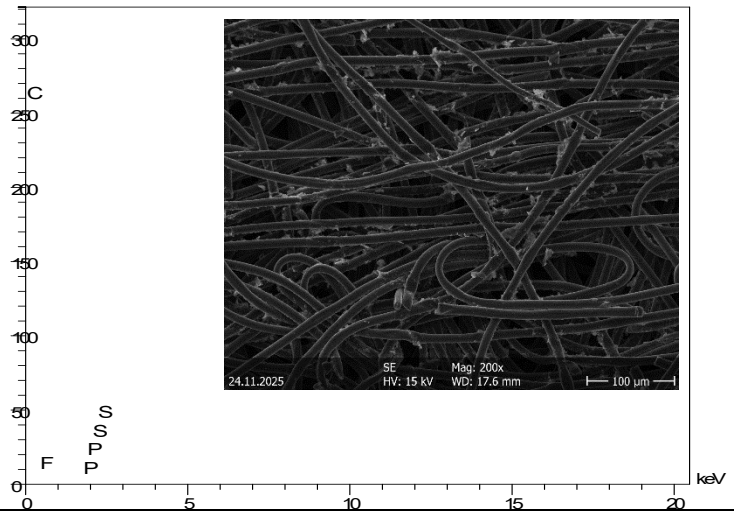

H24C5 Substrate					
Elt	Line	Error	K	W%	A%
C	Ka	57.4876	0.9824	96.58	98.06
F	Ka	1.0821	0.0076	2.41	1.55
P	Ka	0.5923	0.0034	0.35	0.14
S	Ka	0.5923	0.0066	0.66	0.25
Total		1	1	100	100

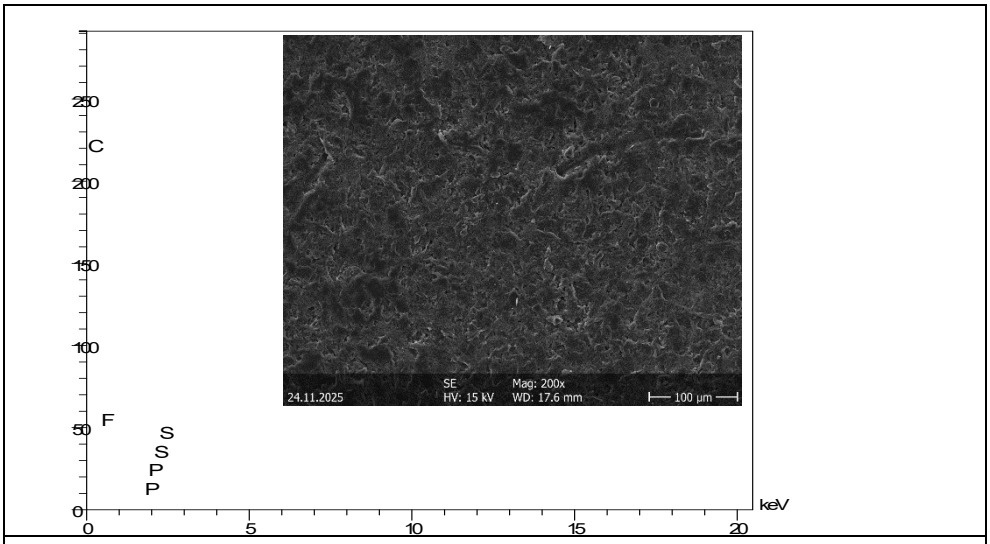

H24C5 MPL					
Elt	Line	Error	K	W%	A%
C	Ka	28.363	0.8617	78.49	85.64
F	Ka	0.9365	0.1123	19.78	13.65
P	Ka	0.5185	0.0045	0.31	0.13
S	Ka	0.5185	0.0215	1.42	0.58
Total		1		100	100

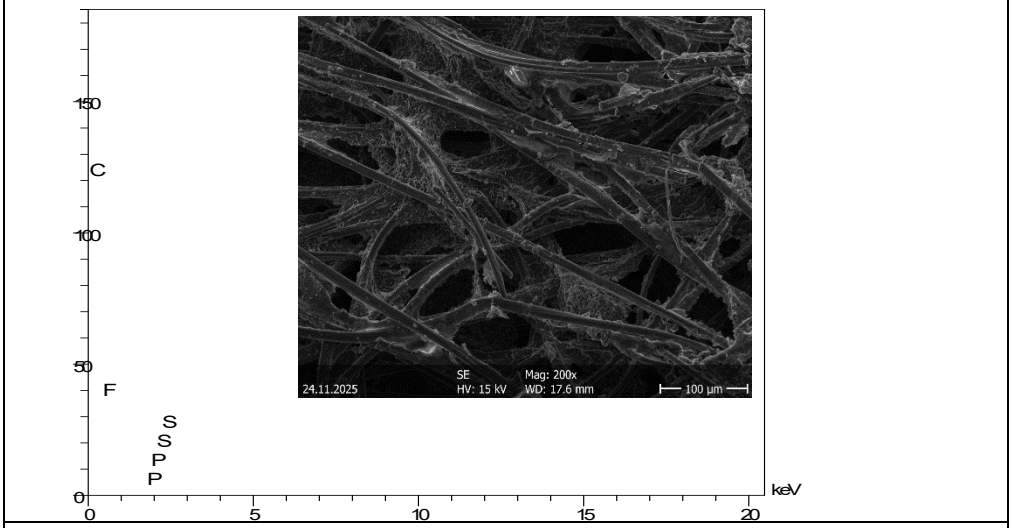

GDL10BA					
Elt	Line	Error	K	W%	A%
C	Ka	18.91	0.8165	73.02	81.35
F	Ka	0.7885	0.1638	25.72	18.11
P	Ka	0.6073	0.0069	0.46	0.2
S	Ka	0.6073	0.0128	0.8	0.33
Total		1		100	100

Appendix D